Structural, magnetic and electrical investigation of Iron-based III/V-semiconductor hybrid structures

Dissertation with the aim of achieving a doctoral degree

at the Faculty of Mathematics, Informatics and Natural sciences

Department of Applied Physics

of Universität Hamburg

submitted by

Dipl.-Phys. Boris Landgraf

from Itzehoe, Germany

2014 in Hamburg

Gutachter der Dissertation: Prof. Dr. W. Hansen

                                     Prof. Dr. R. H. Blick

Gutachter der Disputation: Prof. Dr. U. Merkt

                                     Prof. Dr. W. Hansen

Datum der Disputation: 20. Februar 2014

Vorsitzender des Prüfungsausschusses: Prof. Dr. H. P. Oepen

Vorsitzender des Promotionsausschusses: Prof. Dr. D. Pfannkuche

Dekan der Min-Fakultät: Prof. Dr. H. Graener

Abstract

The major goal of this dissertation was to investigate the structural, magnetic and electrical properties of the following hybrid structures: iron on modulation-doped GaAs (001), iron/MgO/modulation-doped GaAs (001) and iron on inverted, modulation-doped InAs heterostructures. The semiconductor structures were fabricated using regular III/V-semiconductor molecular-beam epitaxy (*MBE*) chambers. A metal *MBE* chamber and MgO *UHV* chamber were built and assembled to deposit iron films and insulating MgO films.

Reflection high-energy electron diffraction experiments demonstrated epitaxial relationships between the materials of the hybrid structures. The experiments revealed that the misfit strain of iron films had different relaxation behaviors on GaAs, MgO and $In_{0.75}Al_{0.25}As$. At the iron/GaAs interface, intermixing led to the formation of Fe_3GaAs and Fe_2As.

In experiments investigating the iron film's in-plane magnetic properties, the crystal directions of the magnetic axes were determined and the thickness-dependence of magnetic anisotropies were studied using magneto-optic Kerr effect microscopy. The results showed different thickness dependencies of uniaxial and cubic anisotropies on GaAs and $In_{0.75}Al_{0.25}As$ substrates. Iron films on MgO exhibited a thickness independent uniaxial anisotropy. Thereby, the magnetic axes were rotated by $90°$ relative to the ones on GaAs and $In_{0.75}Al_{0.25}As$. Mono- and multidomain states during external magnetic field sweeps were identified for each hybrid system.

The electrical properties were investigated by conducting two-terminal current-voltage experiments. The results revealed Schottky barriers at the iron/GaAs and iron/$In_xAl_{1-x}As$ interfaces with varying resistances. The iron/MgO/GaAs interfaces with $2\,nm$, $4\,nm$ and $6\,nm$-thick MgO films exhibited a combination of a trapezoidal shaped barrier and a Schottky barrier. Post-deposition annealing of the iron/MgO/GaAs structures drastically changed the resistivity of the interfaces. Temperature-dependent experiments identified the transport mechanisms across the different barriers.

In addition, the strain relaxation mechanisms of step-graded metamorphic $In_xAl_{1-x}As$ buffers on GaAs (001) substrates with an additional AlAs/GaAs superlattice (*SL*) were examined using high-resolution X-ray diffraction and atomic force microscopy (*AFM*). The experiments revealed that strain between the substrate and the structure's top layer relaxes through the AlAs/GaAs *SL* and also by displaced periodic sections within the metamorphic buffer.

Finally, the electron mobility of inverted, modulation-doped InAs heterostructures with different indium contents was determined by performing magneto-transport experiments.

The carrier concentration dependence of the electron mobility demonstrated that remote impurity scattering is the main limiting factor for the electron mobility. Furthermore, the data revealed a correlation between electron mobility and surface morphology, which was imaged using *AFM*. Lattice relaxation within the 4 nm-thick InAs channel, and thus the generation of misfit dislocations, suggested scattering at charged dislocations as the main reason for the reduced mobility anisotropy at low indium contents.

In conclusion, this study determined the major material characteristics of iron-based III/V-semiconductor hybrid structures. These findings have particular relevance to future spintronic applications.

Kurzfassung

Das Ziel dieser Dissertation war die Untersuchung der strukturellen, magnetischen und elektrischen Eigenschaften der folgenden hybriden Strukturen: Eisen auf modulations-dotierten GaAs (001), Fe/MgO/modulationsdotiertes GaAs (001) und Eisen auf modulationsdotierten InAs Heterostrukturen. Die Halbleiterstrukturen wurden mit III/V-Halbleiter Molekularstrahlepitaxieanlagen (MBE) hergestellt. Eine Metall MBE Kammer und eine MgO UHV Kammer wurden konstruiert und aufgebaut, um Eisen und nicht leitende MgO Filme zu deponieren.

Experimente der Beugung hochenergetischer Elektronen bei Reflexion wiesen epitaktische Beziehungen zwischen den Materialien der hybriden Strukturen auf. Die Ergebnisse zeigten, dass die auf den GaAs, MgO und $In_{0.75}Al_{0.25}As$ Substraten verspannten Eisenfilme unterschiedlich relaxierten. An der Fe/GaAs Grenzfläche führte Durchmischung zu der Formation von Fe_3GaAs und Fe_2As.

Die magnetischen Eigenschaften der Eisenfilme in der Ebene wurden mit magneto-optischer Kerr Effekt Mikroskopie untersucht, um die Kristallrichtungen der magnetischen Achsen der Filme zu bestimmen und die Schichtdickenabhängigkeit der magnetischen Anisotropie zu untersuchen. Die Ergebnisse zeigten unterschiedliche Schichtdickenabhängigkeiten der uniaxialen und kubischen Anisotropie auf GaAs und $In_{0.75}Al_{0.25}As$ Substraten. Die Eisenfilme auf MgO/GaAs wiesen eine schichtdickenunabhängige uniaxiale Anisotropie auf. Die magnetischen Achsen der Anisotropie waren dabei um $90°$ gedreht relativ zu denen von Eisenfilmen auf GaAs und $In_{0.75}Al_{0.25}As$ Substraten. Mono- und multidomäne Zustände wurden für jedes hybride System identifiziert.

Die elektrischen Eigenschaften wurden mit Zweipunkt Strom-Spannungsexperimenten untersucht. Die Ergebnisse zeigten Schottky Barrieren an den Fe/GaAs und $Fe/In_xAl_{1-x}As$ Grenzflächen mit variierenden Widerständen. Die Fe/MgO/GaAs Grenzflächen mit $2\,nm$, $4\,nm$ and $6\,nm$-dicken MgO Filmen wiesen eine Kombination aus trapezförmigen Barrieren und Schottkybarrieren auf. Erhitzen der hergestellten Fe/MgO/GaAs Strukturen veränderte die Widerstände der Grenzflächen drastisch. Temperaturabhängige Experimente identifizierten die Transportmechanismen durch die Grenzflächen der verschiedenen hybriden Strukturen.

Mit hochauflösender Röntgendiffraktion und Rasterkraftmikroskopie (AFM) wurde der Mechanismus untersucht, welcher zum Verspannungsabbau in schrittweise gradierten metamorphen $In_xAl_{1-x}As$ Puffern auf GaAs (001) Substraten mit einem zusätzlichen AlAs/-GaAs Supergitter (SL) führt. Die Experimente zeigten, dass sich die Verspannung zwischen dem Substrat und den obersten Schichten der Struktur durch das AlAs/GaAs SL und durch verschobene periodische Strukturen in dem metamorphen Puffer abbaut.

Die Elektronenmobilität von invertierten, modulationsdotierten InAs Heterostrukturen mit variierendem Indiumgehalt wurde mit Magnetotransportexperimenten untersucht. Die Abhängigkeit von der Ladungsträgerkonzentration demonstrierte, dass Streuung an Störstellen der limitierende Faktor für die Elektronenmobilität ist. Des weiteren zeigten die Daten, dass die Elektronenmobilität und Oberflächenmorphologie, welche mit AFM abgebildet wurde, miteinander korrelieren. Streuung an geladenen Versetzungen durch die Relaxation des 4 nm-dicken InAs Kanals und die Formation von Fehlversetzungen ist der Hauptgrund für die reduzierte Mobilitätsanisotropie bei geringen Indiumkonzentrationen.

Zusammenfassend untersucht diese Studie die Hauptmaterialcharakteristiken von Eisen-basierten III/V-Halbleiter Hybridstrukturen. Diese Ergebnisse haben teilweise Relevanz für zukünftige spintronische Anwendungen.

Contents

1. Introduction to semiconductor/ ferromagnet hybrid systems

Over the last decades, various investigations and experiments have been carried out in the field of spintronics[1–5]. Thereby, many prospective hybrid structures were fabricated to realize and investigate spin injection from binary and ternary ferromagnetic metal alloys into III/V-semiconductors[6–11].

Iron is an attractive material in combination with arsenide semiconductors[12] to be the injection and detection electrode in lateral spin-valve experiments. This is based on the following facts: (i) Iron has a Curie temperature well above room temperature. (ii) Iron can be epitaxially deposited on GaAs[13] and InAs[14]. The epitaxial relationship is related to the body-centered cubic lattice of α-iron ($a = 0.28664\,\mathrm{nm}$[15]) with roughly half the lattice constant of GaAs ($0.56533\,\mathrm{nm}$). In this regard the most likely alignment between iron (001) and GaAs (001) and iron (001) and InAs (001) ($a = 0.60583\,\mathrm{nm}$) would be two iron unit cells for every GaAs unit cell to reduce the compressive and tensile strain to $\sim 1.4\,\%$ and $\sim 5.4\,\%$, respectively. It has been shown that iron is less reactive on InAs surfaces than on GaAs ones[16]. Thus, the formation of unintentional compounds with reduced magnetic moment[17] would be not as strong on InAs.

For instance, the hybrid system iron on GaAs was used to study the efficiency of spin-polarization injection[18,19]. The spins were injected through a reverse-biased iron/GaAs Schottky barrier and detected by another iron/GaAs Schottky barrier contact under zero or forward bias. Thereby, highly-doped GaAs formed a narrow Schottky tunnel barrier to the ferromagnetic iron electrode to achieve efficient tunneling rates. The $500\,\mathrm{nm}$-thick low-doped GaAs conduction channel ensured a long spin-life time[20]. Lou et al. achieved spin diffusion length of $\sim 6\,\mu\mathrm{m}$ in the non-local spin-valve configuration with spin polarizations at the injector and detector electrode of $17\,\%$ and $2\,\%$.

In view of spintronic applications, material systems with spin-orbit coupling are needed to manipulate the injected spin[12,21]. Modulation-doped InAs heterostructures have been

proposed for spintronic device concepts, owing to the strong spin-orbit coupling and the tunable rashba parameter in this material[21–24]. The heterostructures are prepared on molecular-beam epitaxy (*MBE*) fabricated virtual substrates strain-engineered to match the lattice constant of the electronically active layers. The virtual substrates contain metamorphic buffer layers to compensate for the lattice mismatch. Due to a demand for high quality, deposition on GaAs substrates is often preferred. Then a 7 % lattice mismatch exists between relaxed InAs layers and the substrate. This misfit strain must be released in order to avoid a large amount of threading dislocations in the electronically active regions of the device. Recent developments in the design of metamorphic buffers have made possible high-quality epitaxial InAs heterostructures[25–30].

Previous investigations have provided hints about the relaxation processes taking place during the growth of metamorphic buffer layers[31–35]. Linear single and dual slope as well as step-graded $In_xAl_{1-x}As$ ($0.05 < x < 1$) metamorphic buffers have been fabricated and investigated using reciprocal space mapping[36]. It has been shown that an additional AlAs/GaAs superlattice underneath the step-graded $In_xAl_{1-x}As$ metamorphic buffer reduces the density of threading dislocations[37]. Inverted, modulation-doped InAs heterostructures have been grown on top of these metamorphic buffers with and without a superlattice[38]. The introduction of an AlAs/GaAs superlattice leads to improvement in the structure quality and much higher electron mobilities of up to $\mu = 300.000\,\mathrm{cm^2/Vs}$[23]. However, details of the strain relaxation mechanisms in such buffers are still not clear.

Modulation-doped InAs heterostructures on InP substrates were used to accomplish and investigate spin injection from permalloy electrodes in the non-local spin-valve configuration[39]. The InAs heterostructures were fabricated without metamorphic buffers and had low electron mobilities of about $\mu = 55.000\,\mathrm{cm^2/Vs}$. The spin-valve geometries were prepared with ex-vacuo transferring steps. Thereby, argon-milling was applied to reduce the distance thus the resistivity between the heterostructures surface and the InAs layer with the embedded two-dimensional electron gas. Exposure to dry air led to a thin oxide barrier whereon subsequently permalloy was deposited by a sputtered technique. The most likely degeneration of the permalloy/InAs interface due to defect generation during argon-milling and sputtering might led to the relative low remained spin polarization in the semiconductor of 1.4 % at 20 K. The authors accomplished to control the spin precession within these heterostructures through an electric field generated by a gate[40]. The experiments revealed that the detection voltage of the spin-valve structure and thus the spin precession in the semiconductor can be controlled by varying the gate voltage.

The degeneration of the ferromagnet/semiconductor interface can be avoided by using the non-destructive *MBE* deposition method and fabricate epitaxial ferromagnetic films on inverted, modulation-doped InAs heterostructures. In the framework of this thesis a *MBE* chamber for the deposition of metals was assembled and connected to the ultra-high vacuum cluster including III/V-semiconductor *MBE* chambers. Thus, all necessary deposition processes can be operated in-vacuo without exposing the InAs heterostructures to atmosphere. In this regard, very few studies have been conducted about *MBE* fabrication of ferromagnetic materials on inverted, modulation-doped InAs heterostructures[41, 42].

A key issue with this kind of hybrid structures is the ferromagnet/semiconductor interface. Tunnel barriers were suggested to tackle the conductivity mismatch problem in order to achieve spin injection from ferromagnets into semiconductors[43, 44]. It has been shown that Schottky barriers at iron/GaAs interface can be used as tunnel barriers in spin-valve experiments[18, 45, 46]. In order to achieve sufficient spin injection rates the ferromagnet/semiconductor interface is desired to have low interface resistances. In highly-doped semiconductors the strong band bending thus leads to narrow Schottky tunnel barriers enhancing the spin injection rates[47]. The electrical properties like the Schottky barrier height between metals like gold and aluminum and the ternary semiconductor $In_xGa_{1-x}As$ can be tuned by varying the indium content[48, 49]. Thereby, InAs forms an ohmic contact to the metals. So far, no results have been reported on the electrical properties of the interface between iron films and $In_xAl_{1-x}As$ semiconductors which is the top layer of the inverted, modulation-doped InAs heterostructure.

Another way to achieve tunable tunnel barriers between ferromagnetic metals and semiconductors is to deposit thin insulating MgO or Al_2O_3 films with controlled thickness. Advantageously, the oxides can simultaneously act as diffusion barriers during the deposition process of metals[50]. This prohibits intermixing with the underlying semiconductor structure. The oxide barriers can also prevent the ferromagnetic metals from degenerating[41] and from reducing spin injection efficiency into the semiconductor[51, 52]. Notice that pinholes can sometimes arise due to poor surface coverage of the thin insulating films on the semiconductors influencing the spin injection[53–55]. And also oxygen vacancies within the insulating films have an impact on the tunneling process through the potential barrier[56].

In order to comprehend the spin injection process across the ferromagnet/semiconductor interface for specific materials it is important to investigate interdiffusion and thus

intermixing between the materials of the hybrid system, the formation of unintentional compounds at the interface and the magnetic as well as electrical properties of the interface.

This thesis focuses on the fabrication and investigation of structural, magnetic as well as electrical properties of the following hybrid structures: iron on modulation-doped GaAs (001), iron/MgO/modulation-doped GaAs (001) and iron on modulation-doped InAs heterostructures. Chapter 2 introduces the reader to some basic transport concepts across the ferromagnet/semiconductor interface. The experimental methods and procedures which were used to fabricate the semiconductor and hybrid structures and investigate their structural, magnetic and electrical properties are described in chapter 3. Chapter 4 comprises the results of the structural, magnetic and electrical properties of the fabricated semiconductor and hybrid structures. Finally, conclusions are drawn in chapter 5 by summarizing the main results and giving an outlook of selected aspects for future developments and experiments.

2. Basic transport concepts across the ferromagnet/semiconductor interface

A major fundamental issue with using ferromagnetic metals as spin-injectors on semiconductors is the large difference in conductivity between the two materials. This is known as the problem of conductivity mismatch[43]. The following two criteria must be fulfilled to achieve significant spin-injection from a metal contact into a semiconductor[57]: The interface resistance must (i) be spin-selective and (ii) dominate the series resistance in the near-interface region. Tunnel barriers between ferromagnetic metals and semiconductors were suggested as a solution to the conductivity mismatch problem and satisfy both these criteria[44].

In general, the ferromagnetic contact and metal/semiconductor interface should exhibit the following specific characteristics to achieve high spin-injection efficiency at low bias powers for temperatures well above room temperature[57]: (i) The contact/interface should be thermodynamically stable and also thermally stable during material deposition, sample processing and device operation. (ii) The contact/interface should have a reasonable low resistance. High resistances can degrade the signal-to-noise ratios. (iii) The interface should exhibit a low density of defects. Interface defects in heteroepitaxial systems and thus spin scattering can limit the spin-injection efficiency achieved by electrical injection[58]. Therefore, the electrical property of ferromagnet/semiconductor and ferromagnet/insulator/semiconductor interfaces is a major subject in terms of spin injection from ferromagnetic metals into semiconductors. In order to investigate electrical properties of the fabricated hybrid structures it is important to identify the carrier transport mechanisms across the interfaces. The following comprises an overview of selected carrier transport concepts across ferromagnet/semiconductor interfaces.

2.1. Transport across Schottky barriers

The interface of the metal/semiconductor junction forms either an ohmic or a Schottky contact[59,60]. In the ideal case of a Schottky contact without any surface states or other

anomalies the chemical potentials of both materials line up and lead to band bending on the semiconductor side. This is depicted exemplarily for a n-doped semiconductor by the sketch in Figure 2.1. Thereby, the Fermi level of the n-doped semiconductor is lowered by the amount equal to the difference between the work function of the metal $e\varphi_M$ and the one of the semiconductor $e(\chi + \varphi_N)$.
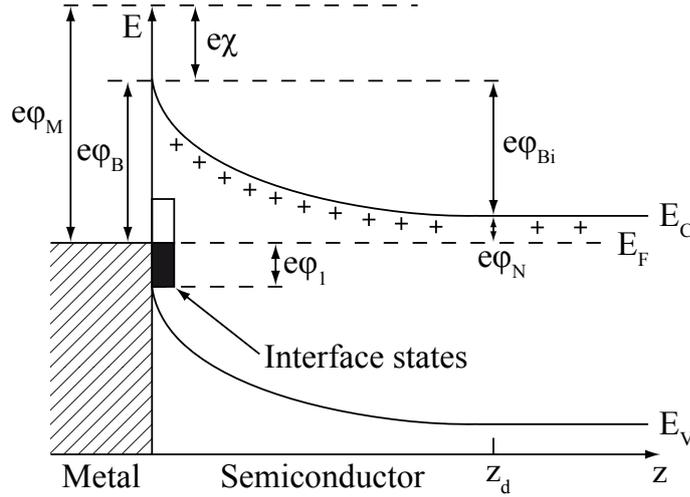
Figure 2.1.: Sketch of the energy-band diagram at the metal/semiconductor interface for a n-doped semiconductor.

The barrier height φ_B of an ideal Schottky barrier where surface effects are neglected is given by the difference between the work function of the metal $e\varphi_M$ and the electron affinity of the semiconductor $e\chi$:

$$e\varphi_B = e(\varphi_M - \chi)$$

Thus, when metals makes contact with the semiconductors the conduction band E_C and valence band E_V are brought into a definite energy offset with respect to the Fermi level of the metal. The subsequent band bending leads to a space charge region due to the positively charged donor atoms which remain in the n-doped semiconductor. The width of this depletion region is defined as

$$z_d = \sqrt{\frac{2\,\epsilon\epsilon_0\varphi_{Bi}}{e\,N_D}}$$

where ϵ is the relative permittivity of the semiconductor, ϵ_0 the vacuum permittivity, e the elementary charge and N_D the donor concentration of the semiconductor. Clearly, the higher the doping concentration the thinner the depletion region at the interface.

In general, the Schottky barrier height is also determined by the states at the metal/semiconductor interface. The existence of the interface states is related to the extensive Bloch states of the metal. These states decay in the semiconductor and superimpose with the wave functions of either the valence or conduction band. The energy of the interface states is located relative to the conduction and valence band edge. The usual high density of states at the metal/semiconductor interface leads to pinning of the Fermi level at the charge neutrality level and thus the formation of a Schottky barrier. The band bending on the semiconductor side as it is shown in Figure 2.1 for a n-doped semiconductor is defined by the condition of charge neutrality between the interface states and the donor states.

For most III/V compound semiconductors, the barrier height is essentially independent of the metal work function[59]. In this limit the barrier height is entirely determined by the surface properties of the semiconductor:

$$e\varphi_B = E_g - e\varphi_1$$

where E_g is the bang gap of the semiconductor and φ_1 the sum of the neutral level of interface states φ_0 and the interface-trap charge Q_{SS}.

Since Schottky barriers can form at the metal/semiconductor interface, charge carriers have to overcome or tunnel through this potential barrier when applying a voltage between metal and semiconductor. The following two section describe the carrier transport across Schottky barriers.

Thermionic-emission theory

Bethe developed a comprehensive thermionic-emission theory to describe the transport of charge carriers across a metal/semiconductor junction with energies larger than the barrier height $e\,\varphi_B$[61]. In this model, the transport across the barrier consists essentially of two currents. The diffusion current arises from the semiconductor into the metal due to different carrier concentrations. Simultaneously, the electric field caused by the band bending leads to the drift current of carriers from the metal into the semiconductor. At zero bias these two currents are equal so that the net current vanishes when thermal

equilibrium prevails. The band diagrams in Figure 2.2 show the metal/semiconductor junction with a n-doped semiconductor under (a) forward and (b) reverse bias.
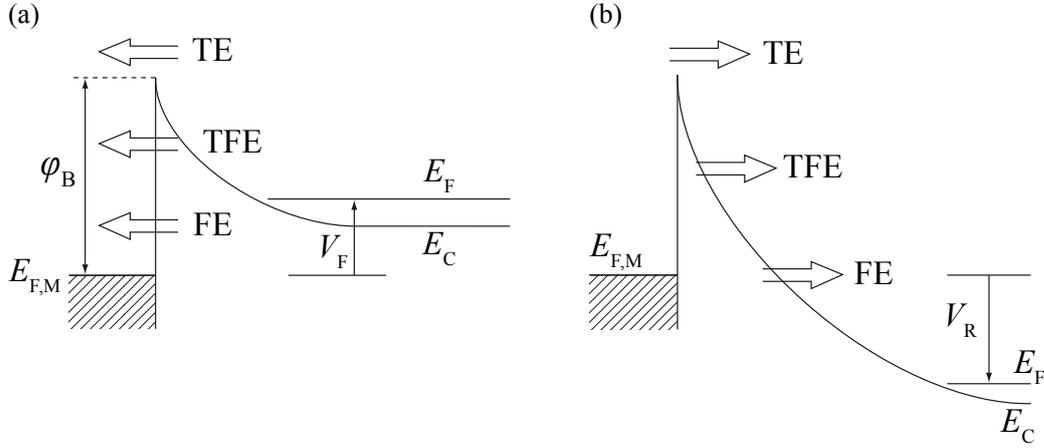
Figure 2.2.: Schematic of the energy-band diagram for the Schottky diode with a n-doped semiconductor under (a) forward and (b) reverse bias. The arrows display possible transport contributions.

Under forward bias the Fermi level increases on the semiconductor side. The applied electric field reduces the depletion region by charge carriers diffusing into the space charge region. Accordingly, more carries can overcome the barrier and flow from the semiconductor into the metal. Under reverse bias the Fermi level decreases on the semiconductor side. The applied electric field leads to a larger depletion region by charge carriers diffusing out of the space charge region. As a result, carriers can overcome or tunnel through the barrier and flow from the metal into the semiconductor. The current transport across metal/semiconductor junctions is mainly due to majority carriers, i.e., in the case of n-type semiconductors by electrons. The sum of the two opposite currents yields the total current across the barrier which results in the current-voltage characteristic described as:

$$I \;=\; I_S \cdot \left[\exp\left(\frac{eV}{n\,k_B\,T} \right) - 1 \right] \tag{2.1}$$

$$I_S \;=\; A\,A^*\,T^2 \cdot \exp\left(\frac{-e\,\varphi_B}{k_B\,T} \right)$$

$$A^* \;=\; \frac{4\pi\,e\,m^*\,k_B^2}{h^3} \tag{2.2}$$

where I_S is the saturation current, V the applied voltage, n the ideality factor, A^* the Richardson constant, A the cross-sectional area of the contact, m^* the effective mass and k_B the Boltzmann constant.

Certain mechanisms like recombination of carries in the depletion region, thermionic-field emission and tunneling of carriers through the Schottky barrier can lead to deviations from the Bethe model. The ideality factor accounts for these deviations. It is equal to one for an ideal Schottky diode with pure thermionic-emission transport over the potential barrier.

Experimentally, the characteristic parameters of a metal/semiconductor junction as barrier height φ_B and ideality factor n can be obtained from a fit of the measured voltage as a function of the current. A logarithmic fit yields the coefficients α and β:

$$V = \alpha \cdot \ln\left(\beta \cdot I + 1\right) \tag{2.3}$$

These coefficients result in ideality factor n and the barrier height φ_B:

$$n = \frac{e\,\alpha}{k_B T} \tag{2.4}$$

$$\varphi_B = -\frac{k_B T}{e} \ln\left(\frac{1}{AA^*T^2\beta}\right) \tag{2.5}$$

The Schottky barrier height φ_B by means of an activation-energy measurement and also the Richardson constant A^* can be determined from the experimental data by constructing a Richardson plot. This analyzes the temperature dependence of the saturation current I_S in reverse bias so that equation 2.1 results as:

$$\ln\left(\frac{I_S}{T^2}\right) = \underbrace{\ln\left(A\,A^*\right)}_{a} - \underbrace{\frac{e\,\varphi_B}{k_B}}_{b} \cdot \frac{1}{T} \tag{2.6}$$

The slope b of a plot of $\ln\left(I_S/T^2\right)$ versus the inverse of the temperature yields the barrier height and the ordinate intercept a at $1/T = 0$ the product of cross-sectional area A and Richardson constant A^*. Advantageously, no assumption of the electrically active area is required to determine the barrier height. In the Richardson plot the experimental data will reveal a range with a linear dependence on the inverse of the temperature. The Bethe model of thermionic emission is valid in this range and the data can be reasonably fit with equation 2.6.

Tunneling through the potential barrier

While the thermionic-emission theory implies only charge transport over the barrier tunneling of carriers through the potential barrier may become more significant for more heavily doped semiconductors and/or at lower temperatures[59]. Notice that both the ideality factor n and the saturation current I_S in equation 2.1 increase if tunneling starts to occur. The carrier transport over and through the barrier can roughly be categorized into three types: 1. thermionic-emission (TE) over the barrier, 2. field-emission (FE) near the Fermi level and thermionic-field emission (TFE) at an energy between TE and FE. The three types of carrier transport under (a) forward and (b) reverse bias are depicted in Figure 2.2.
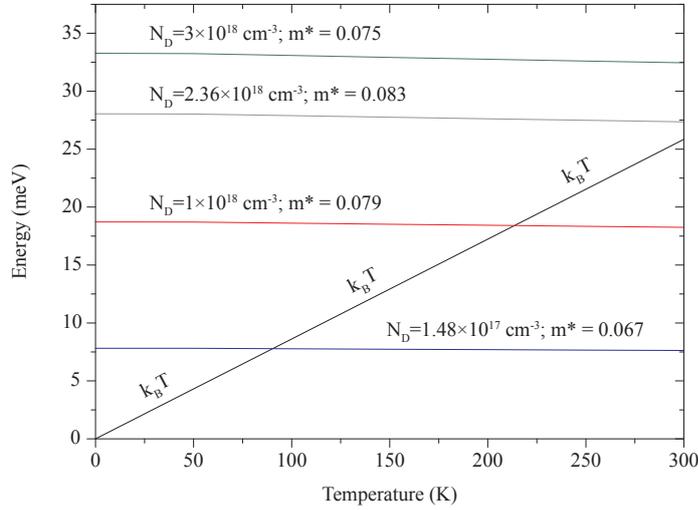
Figure 2.3.: The graph shows a plot of the thermal energy $k_B T$ and characteristic energy E_{00} of GaAs as a function of the temperature.

The dominant transport mechanism can be estimated by comparing the thermal energy $k_B T$ to the characteristic energy E_{00}:

$$E_{00} = \frac{e\,\hbar}{2} \cdot \sqrt{\frac{N_D}{m^*\,\epsilon_{SC}(T)}} \tag{2.7}$$

where $\hbar$ is the Planck's constant, m^* the effective mass and $\epsilon_{SC}(T)$ the temperature dependent permittivity of the semiconductor. If the thermal energy is much larger than E_{00} thermionic-emission is the main transport mechanism. When the energy E_{00} is much larger than the thermal energy tunneling predominates and when the energies are equal thermionic-field emission dominates the transport across the barrier.

The graph in figure 2.3 presents a plot of the thermal energy $k_B T$ and characteristic energy E_{00} of GaAs as a function of temperature. The latter energy was determined for several observed combinations of doping concentration and effective masses[62–64] and with the temperature dependent permittivity of GaAs: $\epsilon_{SC}(T) = \epsilon_0 (1 + \lambda T) = 12.35 (1 + 2.01 \cdot 10^{-4} T/K)$[65]. The data reveal that tunneling of electrons through the potential barrier can occur at room-temperature for doping concentration larger than $\sim 2 \times 10^{18}$cm^{-3}. But impurities at the interface and also interfacial layers caused by intermixing might lower the probability of tunneling.

2.2. Rowell criteria for tunneling transport

Originally, a set of „AND" criteria was formulated by Rowell to identify tunneling as the dominant transport mechanism in superconductor/insulator/superconductor structures[66]. If neither of the electrodes superconduct as it is for ferromagnet/insulator/ferromagnet structures only three of these criteria remain to apply[67]:

First criterion: The conductance $(dG = dI/dU)$ should have an exponential dependence on the thickness of the barrier: $G(s) \sim \exp(s/s_0)$ with $s_0 = \hbar/2 \sqrt{2m\varphi_B}$.

Second criterion: The conductance should have a parabolic dependence on the voltage and can be fit with the Simmons (symmetric barrier)[68] or Brinkman, Dynes and Rowell model (asymmetric barrier)[69].

Third criterion: The slope of the current-voltage characteristic (dU/dI) at zero bias (ZBR) should exhibit a weak insulating-like temperature dependence.

Notice, the first criterion cannot be applied for Schottky barriers because of variations of the barrier's width with the bias voltage. Ånkerman et al. have shown that the second criterion can be applied even when tunneling was not the dominant transport mechanism[70]. They have presented convincing evidence that the third Rowell criterion definitely confirms tunneling as the dominant conduction mechanism through the barrier. The third criterion can also be used to rule out the existence of pinholes in thin tunnel barrier layers[54, 70]. In this thesis, the third Rowell criteria was applied to identify tunneling as the dominant transport mechanism across the ferromagnet/semiconductor interface of the fabricated hybrid structures.

2.3. Brinkman, Dynes and Rowell model of a trapezoidal potential barrier

Simmons[68] derived a formula to describe the electron tunneling transport between similar electrodes separated by an insulating film with an arbitrary shaped potential barrier. Brinkman, Dynes and Rowell extended the Simmons's model with an asymmetry component when the electrodes are made out of different materials. Their model describes the parabolic dependence of the conductance $G(V)$ on the applied voltage for trapezoidal shaped potential barriers[69]. Figure 2.4(a) presents a sketch of such an asymmetric barrier. They observed that the following expression is accurate to roughly 10 % for barriers thicker than 1 nm and when $\Delta\varphi/\bar{\varphi} \ll 1$.

$$\frac{G(V)}{G(0)} = 1 - \left(\frac{A_0\,\Delta\varphi}{16\,\bar{\varphi}^{3/2}}\right) eV + \left(\frac{9}{128}\frac{A_0^2}{\bar{\varphi}}\right)(eV)^2 \tag{2.8}$$

$$G(0) = \frac{e^2 A\sqrt{2m\bar{\varphi}}}{h^2 s}\exp\left(-\frac{2s}{\hbar}\sqrt{2m\bar{\varphi}}\right)$$

where $G(0)$ is the differential conductance at zero bias, $A_0 = 4s\sqrt{2m}/(3\hbar)$, A the cross-sectional area of the tunnel contact, m the electron mass, s the barrier thickness in Å, $\bar{\varphi}$ the average height and $\Delta\varphi$ the asymmetry of the barrier in volt.

Since the expression above was developed in powers of voltage of second order a parabolic fit of the differential conductance versus the applied voltage yields the coefficients $K_0\,(\bar{\varphi}, s)$, $K_1\,(\bar{\varphi}, \Delta\varphi, s)$ and $K_2\,(\bar{\varphi}, s)$:

$$G(V) = \frac{dI}{dV} = K_0\,(\bar{\varphi}, s) + K_1\,(\bar{\varphi}, \Delta\varphi, s)\,V + K_2\,(\bar{\varphi}, s)\,V^2 \tag{2.9}$$

The characteristic parameters of the tunnel barrier can be obtained from these coefficients which results in the average height $\bar{\varphi}$, thickness s and asymmetry $\delta\varphi$ of the tunnel barrier as follows:

$$\bar{\varphi} = \frac{e}{4}\sqrt{\frac{K_0}{2K_2}}\ln\left(\sqrt{K_0 K_2}\frac{h^3}{\sqrt{2}e^3 m\pi A}\right), \tag{2.10}$$

$$s = \frac{2\hbar}{e}\sqrt{\frac{K_2}{K_0}\frac{\bar{\varphi}}{m}}, \tag{2.11}$$

$$\Delta\varphi \;\; = \;\; -\frac{K_1}{K_0}\,\frac{12\,\hbar\,\bar{\varphi}^{3/2}}{\sqrt{2mes}} \tag{2.12}$$

Notice that the Brinkman, Dynes and Rowell model is valid not only for single trapezoidal shaped tunnel barriers. It can also be applied if two potential barriers formed between the two different electrodes. A second barrier might be formed by oxidizing the substrate during deposition or post-annealing the hybrid structures leading to interfacial reactions[71]. Figure 2.4(b) shows a sketch of two trapezoidal shaped barriers with different heights and asymmetries.
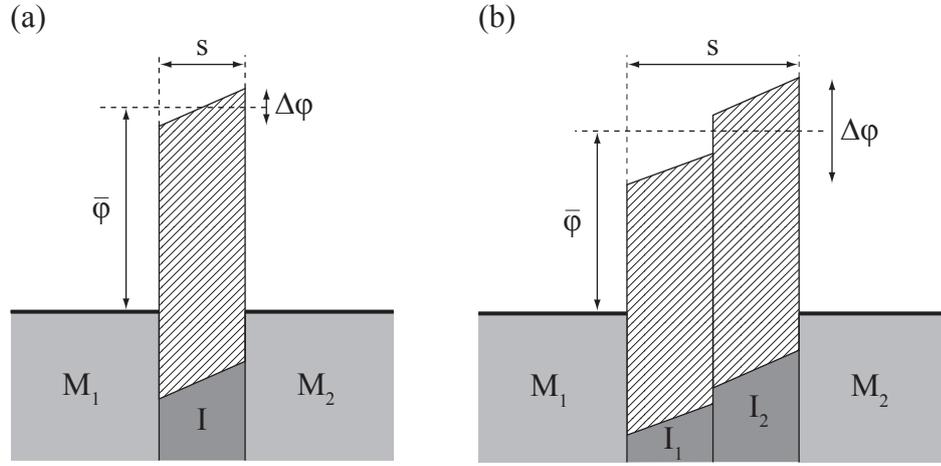
Figure 2.4.: (a) Single trapezoidal shaped potential barrier separated by electrodes M_1 and M_2. The electrodes are made out of different materials. (b) two trapezoidal shaped potential barriers I_1 and I_2 separated by electrodes M_1 and M_2. The insulators as well as the electrodes are made out of different materials. The sketches reflect the situation at zero bias.

In the case of two potential barriers, a parabolic fit of the measured conductance as a function of the applied voltage with equation 2.9 would also result in an average height $\bar{\varphi}$, thickness s and asymmetry $\Delta\varphi$ of the barriers. Based on the Brinkman, Dynes and Rowell model it cannot be excluded that only one barrier is formed between the electrodes. But, the characteristic parameters of the potential barrier and also their temperature dependence can delineate its form roughly.

3. Experimental methods and procedures

This chapter contains descriptions of the experimental methods and procedures which were used to fabricate the semiconductor and hybrid structures and investigate their structural, magnetic and electrical properties.

3.1. Molecular beam epitaxy

Molecular beam epitaxy (MBE) is a deposition method suitable to fabricate homo- or heteroepitaxial thin crystalline layers, complex heterostructures as well as quantum dots and nanowires. MBE allows atomically precise control of composition, thickness and possible doping materials of each structure, independently. An advantage of this method compared to other fabrication techniques is the possibility to control the deposition parameters in wide range with very high precision whereby sharp doping and composition profiles are formed.

The outer part of the MBE chambers is made out of stainless steel. Each chamber incorporates a manipulator on which three-inch molybdenum blocks can be mounted with two-inch wafers. The manipulators can rotate and heat the samples during deposition. Deposition materials are either evaporated by effusion cells or electron-beam evaporators. The materials inside the evaporators are kept in boron nitride, Al_2O_3 or copper crucibles depending on the evaporation temperature of the material. The geometric form of the effusion cells leads to molecular beams which are directed to the substrate. Mechanically controlled shutters can switch the beams of each cell on and off, independently. During deposition process supersaturation leads to condensation of atoms on the surface of the substrate through the constant particle flux thus to nucleation and growth of the structures on the substrate[72]. Reflection high-energy electron diffraction ($RHEED$), low-energy electron diffraction ($LEED$) and Auger electron spectroscopy are used to in-situ monitor the deposition process and in-vacuo analyze fabricated structures.

Figure 3.1 displays the ultra-high vacuum (UHV) cluster. In addition to the introduction, transfer and degas chambers the cluster has three MBE chambers. The Riber 32P and

Riber C21 *MBE* chambers used to fabricate III/V compound semiconductors and the metal *MBE* chamber to deposit metal alloys. The MgO *UHV* chamber is specifically designed for thin tunnel barriers. The mask *UHV* chamber is designed to fabricate patterned metal droplets but still under construction.
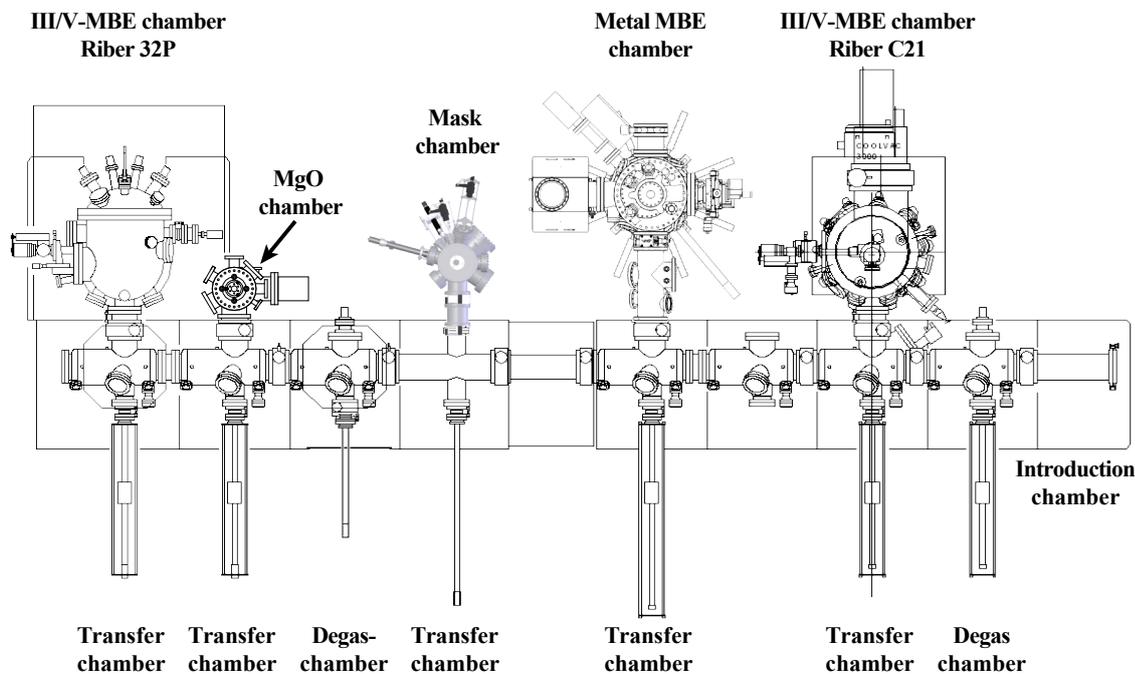
Figure 3.1.: Schematic of the *UHV* cluster.

3.1.1. III/V-MBE chambers

In this thesis the III/V-semiconductor structures were fabricated with the Riber 32p and the Riber C21 *MBE* chambers. Cryogenic pumps and in the case of the Riber 32p also a combination of ion getter and titanium sublimation pump kept the *UHV* base pressure inside these chambers in the range between the upper 10^{-12} mbar and middle 10^{11} mbar. In addition to the pumps, liquid nitrogen cryogenic shrouds froze impurity atoms out and lower the residual gas pressure. The low background pressure enabled a sufficient mean free path L[73] for atoms in the molecular beam of several kilometers. Thus, the interaction between atoms in the beam within the distance of the effusion cells and the substrate was negligible.

Single $450\,\mu$m-thick GaAs (001) crystal wafers were used as substrates. Before deposition, the temperatures of the GaAs (001) substrates were calibrated by monitoring with *RHEED*

the desorption of the thermal oxide at an absolute temperature of $582\,°C$ [74]. The elements gallium, aluminum and indium as well as the donor doping material silicon were evaporated by effusion cells. The arsenic was supplied by an valved arsenic cracker source. The temperature of the arsenic reservoir was kept at about $330\,°C$ and the cracker temperature at $550\,°C$. The flux of the arsenic was regulated by a needle valve which was controlled by a stepper motor. The deposition rates of the compounds GaAs and AlAs of $0.8\,\mathrm{ML/s}$ and $0.4\,\mathrm{ML/s}$ were calibrated by monitoring the intensity oscillations of the specular beam with *RHEED*. In the case of InAs the deposition rate was $0.01\,\mathrm{ML/s}$. It was determined by measuring the time when reflexes from InAs quantum dots appear on the *RHEED* screen at a critical coverage of $\theta_c = 1.68\,\mathrm{ML/s}$ [75]. Different compositions of $In_xAl_{1-x}As$ and $In_xGa_{1-x}As$ were enabled by varying the indium effusion cell temperatures T_{In}. Thereby, the effusion cell temperatures of gallium and aluminum were the same as for the compounds GaAs and AlAs with the deposition rates of $0.8\,\mathrm{ML/s}$ and $0.4\,\mathrm{ML/s}$.

3.1.2. MgO UHV chamber

The MgO *UHV* chamber was custom-built to fabricate thin tunnel barriers between semiconductor structures and ferromagnetic metals. Figure 3.2 shows pictures of the MgO chamber.
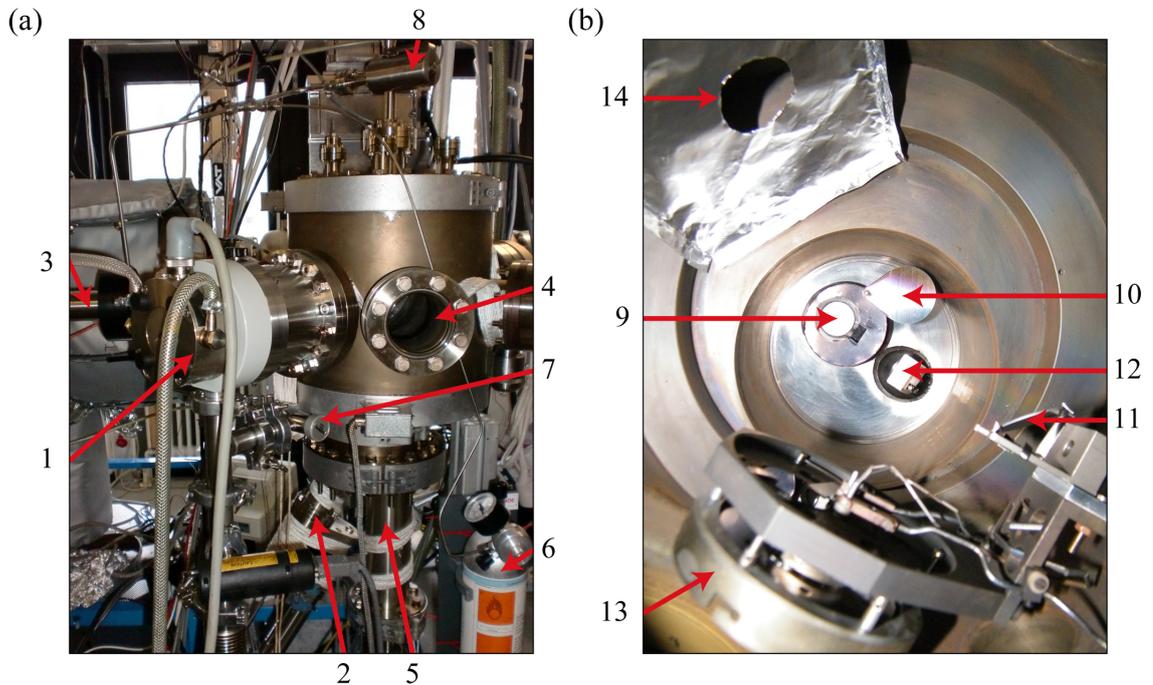
Figure 3.2.: (a) Outer and (b) inner parts of the MgO chamber.

A combination of scroll and water-cooled turbo pump (1) kept the base pressure of the chamber at 9×10^{-9} mbar. The electron-beam evaporator (5) vaporized MgO powder which was compressed in the copper crucible (9). The crucible was visible through the view port (4) via the mirror (11) to adjust and focus the electron beam on the MgO material. The molybdenum blocks with the substrates on it were mounted on the non-heatable manipulator (3, 13). Thereby, the aluminum mask (14) prevented the molybdenum blocks from contamination with MgO. The chamber has an oxygen injection system to grow stoichiometric MgO[71]. The aluminum bottle (6) supplied the O_2 gas. The valve (7) was used to flush and pump the stainless steel pipes between gas bottle and chamber with the scroll pump. The needle valve (8) regulated the oxygen gas flow into the chamber. During the deposition of MgO the background pressure with the additional oxygen gas was about 5×10^{-6} mbar. The deposition of MgO started and stopped by turning the manipulator with the substrate on it from the transfer position downwards into the molecular beam. Thereby, the shutter (10) above the crucible was opened. The deposition was monitored in-situ with the water-cooled oscillating crystal (2) and the SQM 160 Multi-Channel Quartz Crystal Monitor. The scale of the monitor was calibrated with specular X-ray reflectivity as described in section 3.4.2. Figure 3.3 presents the reflectivity curve and fit of the experimental data. The fit resulted in the deposition rate of 0.57 nm/min. The data reveal that a Ga_2O_3 layer formed between the GaAs substrate and the MgO layer. Unfortunately, no systematical investigation of the deposition rate of MgO and effect of oxidation of the GaAs substrate could be conducted because of a defect X-ray tube.
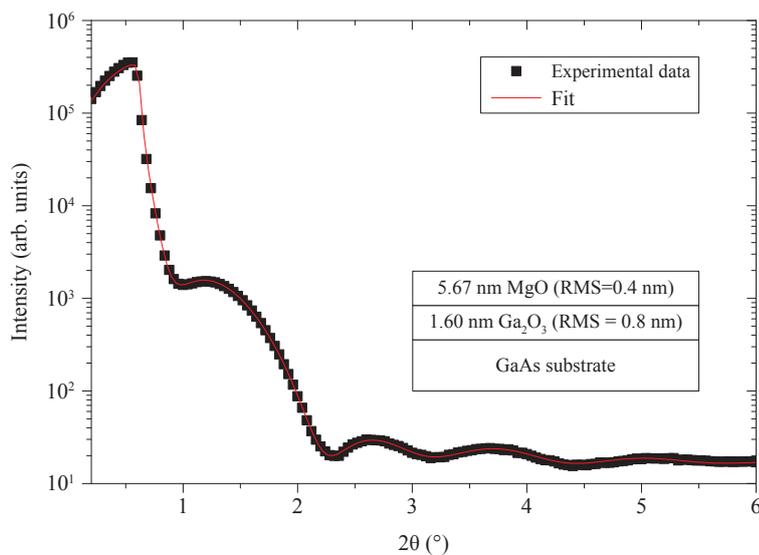
Figure 3.3.: Specular X-ray reflectivity curve and fit of the data.

3.1.3. Metal MBE chamber

The metal *MBE* chamber was custom-built to fabricate ferromagnetic thin films[76]. The chamber enables the deposition of different single or binary component material systems or Heusler alloys without changing the fillings of the effusion cells. In addition, it is possible to investigate the deposition process and fabricated structures in-situ using different analysis methods as Auger spectroscopy, low-energy electron diffraction (*LEED*) and *RHEED*. This section comprises the functionality of the chamber and the deposition rate calibrations of the materials iron and gold.
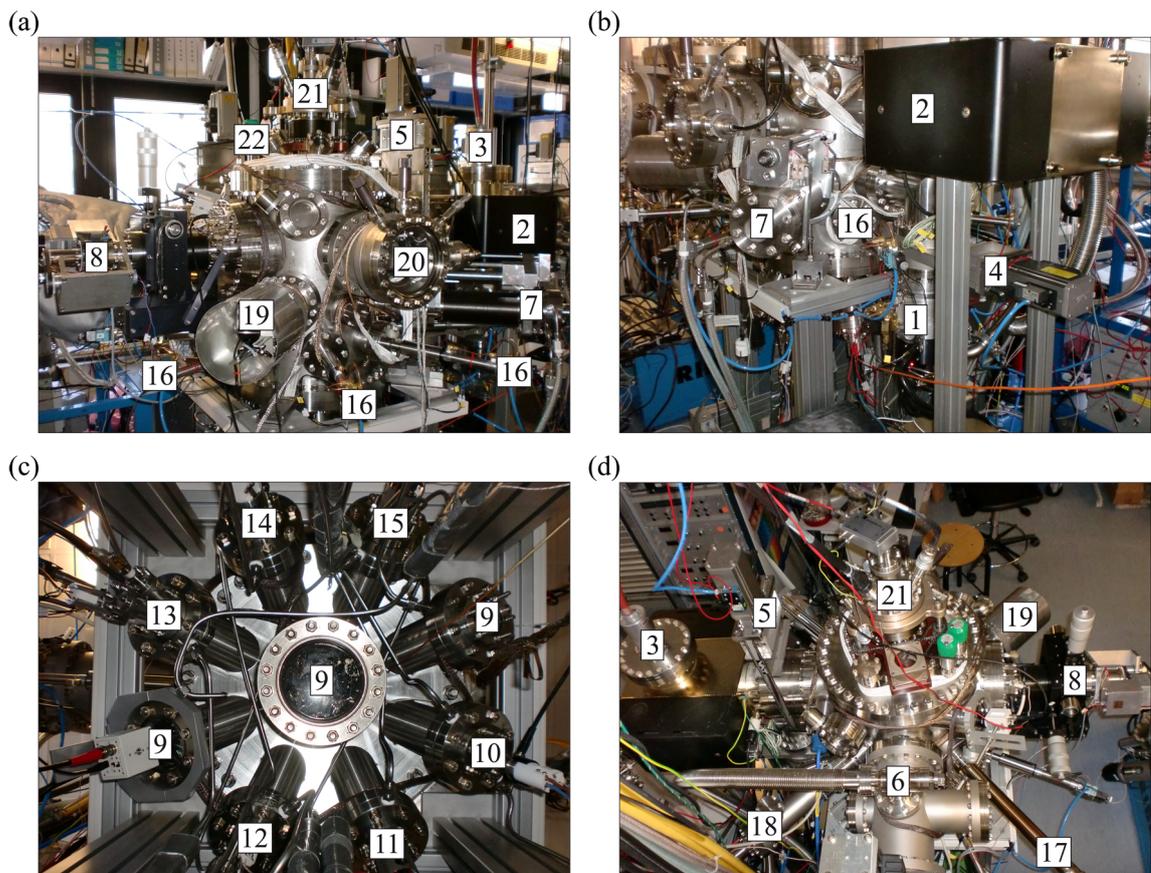
Figure 3.4.: The metal *MBE* chamber with its components.

Experimental setup

Figure 3.4 shows different views from (a) and (b) the sides, (c) underneath and (d) the top of the chamber with its individual components. On standby the combination of ion getter (2) and titanium sublimation pump (3) kept the base pressure of the chamber at 5×10^{-10} mbar. Thereby, the gate valve (4) between chamber and turbo pump was closed

and the gate valve (5) between chamber and ion getter pump opened. During deposition process the titanium sublimation pump was switched off to avoid contamination of the substrate or grown material with titanium. At pressures above 1×10^{-9} mbar the gate valve (5) was closed and the gate valve (4) opened. The chamber was pumped then with a combination of scroll and turbo pump (1). For maintenance, the chamber was vent via the fore-vacuum system of the transfer line by opening the valve (6) while both gate valves (4, 5) are closed. A quadrupole mass spectrometer (7) was installed to either analyze the residual gas in the chamber or the elements of the molecular beam. Therefore, the mass spectrometer was translated to deposition position of the substrate while the manipulator was turned into transfer position.

Figure 3.4(c) shows a view from underneath the chamber. Nine ports are visible. The view ports (9) were used to adjust the substrate in deposition position. Water-cooled effusion cells were installed at the other six ports. They are radially arranged around the vertical axis of the chamber so that the generated molecular beams are directed to the center of the substrate. The effusion cells contained the following materials: iron (10), cobalt (12), manganese (14), indium (15), gold (11) and silicon (13). With these materials it was possible to fabricate thin crystalline films of single elements or alloys. The gold was used to cover the grown ferromagnetic films in order to prevent them from oxidization. Linear cell shutter and a main shutter (16) switched the molecular beams on and off to start and stop the deposition. The molybdenum blocks with the GaAs substrates were mounted on a heatable manipulator (8). The substrates could be heated up to about $700\,^\circ$C. During deposition the substrate was rotated with 10 rpm to achieve homogeneous film thicknesses and homogeneous compositions.

Different in-situ analysis methods were installed to characterize the fabricated structures. Therefore, the manipulator could be rotated to either the position of the Auger spectrometer (21), the low-energy electron diffractometer (20) or downwards to deposition position. The *RHEED* system with the electron gun (18) and the fluorescence screen (19) was installed to in-situ monitor the deposition process. During deposition the tantalum mask was translated (17) and positioned 1 cm below the substrate to prevent the molybdenum blocks from contamination with deposition material. Thereby, the electron beam of the *RHEED* system was still able to strike the surface of the sample with a small incident angle by going through the gap between mask and sample. Furthermore, the mask was to fabricate thickness gradients as it will be discussed in section 3.3.

Deposition rate calibration of iron and gold

The deposition rate of iron was determined on a 100 nm-thick buffer layer of undoped GaAs via *RHEED*. This in-situ characterization technique will be further described in section 3.2.
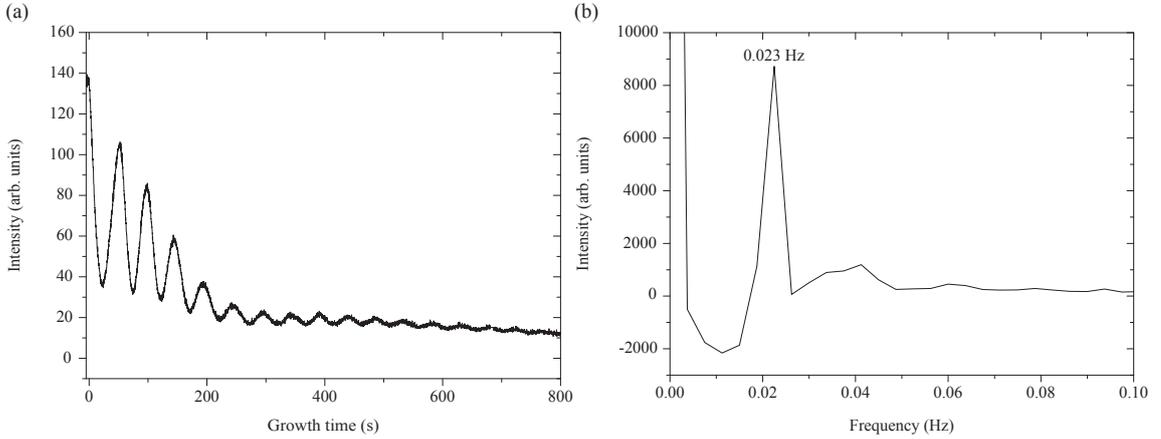
Figure 3.5.: Monitoring the deposition of iron on GaAs (001) with *RHEED*. (a) Intensity oscillations of the specular beam. (b) Fast Fourier transform of the intensity oscillations.

The buffer was fabricated on a GaAs (001) substrate in one of the III/V-*MBE* chambers, had an arsenic terminated surface and showed a 2×4 surface reconstruction. In the metal *MBE* chamber the electron beam was adjusted to a small incident angle of about $1°$ in the $[\bar{1}10]$ crystal direction. During deposition the surface was investigated by monitoring the intensity of the specular electron beam. First of all, the shutter of the iron effusion cell was opened for two minutes before starting the deposition to reduce the effect of the shutter transient. The deposition of iron started by opening the main shutter. It occurred at a substrate temperature of 230 °C. Figure 3.5(a) shows intensity oscillations of the specular beam due to the growth of monolayers.

The fast Fourier transform of the *RHEED* oscillations in Figure 3.5(b) shows a distinct peak at the frequency of 0.0238 Hz. It corresponds to the deposition rate of 0.4093 nm/min. Further measurements at several iron effusion cell temperatures T_{Fe} (° C) determined the typical exponential behavior of the cell. Figure 3.6 shows the experimental data and the red curve the best exponential fit:

$$\text{Iron growth rate} = \left(-0.0084 + 5.5423 \cdot 10^{-10} \exp\left(0.0133 \cdot T_{\mathrm{Fe}}\right)\right) \text{ML/s}.$$

The exponential fit has an offset of -0.0084. This offset is caused by the thermocouple of the effusion cell positioned a few millimeter underneath the crucible with the iron material inside.
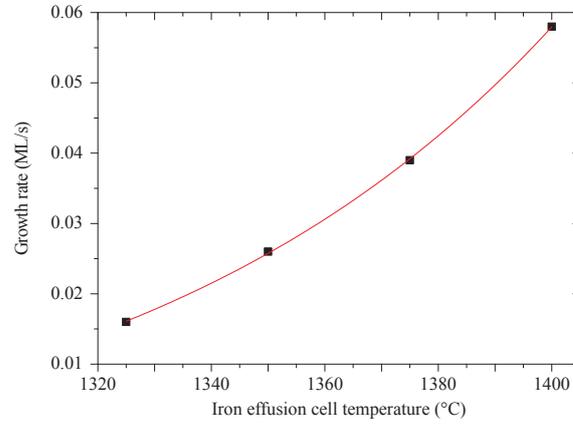
Figure 3.6.: Iron deposition rate in monolayers per second versus the temperature of the iron effusion cell. The red curve is the exponential fit to the experimental data.

The deposition rate gold of was determined by measuring the thickness of a deposited gold film with atomic force microscopy. Thereby, gold was deposited at the effusion cell temperature of $T_{Au} = 1200\,°C$ on a SiO_2 substrate for $60\,min$. Subsequently, the film was patterned with the optical resist S1813 and etched with diluted HCl:HNO$_3$ (3:1) down to the surface of the SiO_2 substrate. An atomic force microscope scan in tapping-mode[77] across the fabricated edge resulted in a deposition rate of $0.5\,nm/min$. The surface of the gold film had an average roughness of about $0.5\,nm$.

3.1.4. Sample design and deposition sequences

This section depicts the sample design and fabrication process of the different hybrid structures. Figure 3.7 shows schemes of the individual structures. Two-inch undoped GaAs (001) and SiO_2 (001) substrates mounted on three-inch molybdenum blocks were introduced into the *UHV* cluster via the introduction chamber. Before transferring them into the deposition chambers they were degassed at $400\,°C$ for 2 hours in the degas chambers. This was necessary to evaporate H_2O and other residuals from the surfaces of the molybdenum block and the wafer.

(a)

Gold (2 nm)
Iron
MgO (2 - 6 nm)
n^{++} Si-doped GaAs (15 nm)
n → n^{++} Si-doped GaAs (15 nm)
n Si-doped GaAs (500 nm)
(001) GaAs - substrate

(b)

Gold (2 nm)		
Iron		
Quantum well region	In$_{0.75}$Al$_{0.25}$As (15 nm)	
	In$_{0.75}$Ga$_{0.25}$As (11 nm)	
	InAs (4 nm)	
	In$_{0.75}$Ga$_{0.25}$As (2 nm)	
	In$_{0.75}$Al$_{0.25}$As spacer (5 nm)	
	Si-doped In$_{0.75}$Al$_{0.25}$As (7 nm)	
In$_{0.75}$Al$_{0.25}$As (530 nm)		
In$_x$Al$_{1-x}$As	x=0.65 (100 nm)	Metamorphic buffer
	x=0.55 (100 nm)	
	x=0.45 (100 nm)	
	x=0.35 (100 nm)	
	x=0.25 (100 nm)	
	x=0.14 (100 nm)	
	x=0.06 (50 nm)	
Superlattice (20 x 2.8 nm)		
(001) GaAs - substrate		

(c)

Gold (2 nm)		
Iron		
n Si-doped In$_x$Al$_{1-x}$As (1000 nm)		
n^{++} Si-doped In$_x$Al$_{1-x}$As (300 nm)		
In$_x$Al$_{1-x}$As	x=0.65 (100 nm)	Metamorphic buffer
	x=0.55 (100 nm)	
	x=0.45 (100 nm)	
	x=0.35 (100 nm)	
	x=0.25 (100 nm)	
	x=0.14 (100 nm)	
	x=0.06 (50 nm)	
Superlattice (20 x 2.8 nm)		
(001) GaAs - substrate		

Figure 3.7.: Sample designs of the hybrid structures (a) iron/MgO/modulation-doped GaAs (001), (b) iron on inverted, modulation-doped InAs heterostructure and (c) iron on modulation-doped In$_x$Al$_{1-x}$As. All structures are capped with a thin layer of gold to prevent the iron from oxidization[78].

Iron on modulation-doped GaAs (001)

Figure 3.7(a) shows the layer sequence of the iron on modulation-doped GaAs (001) structure containing an additional layer of MgO. The hybrid structures were deposited with the solid-source Riber 32p as well as the Riber C21 *MBE* chambers. The modulation-doped GaAs (001) consists of an undoped GaAs (001) substrate, a 500 nm-thick low-doped ($5 \times 10^{16}\,\text{cm}^{-3}$) and a 15 nm-thick highly-doped ($3 \times 10^{18}\,\text{cm}^{-3}$) GaAs layer. The semiconductor structures were transferred in-vacuo into the *MBE* chamber for the deposition of metals. The iron was deposited at the deposition rate of 0.4 nm/min while rotating the sample with 10 rpm. The pressure in the chamber 5×10^{-9} mbar. The deposition processes were monitored by *RHEED*.

Iron/MgO/modulation-doped GaAs (001)

The modulation-doped GaAs (001) structures were deposited using either the Riber 32p or the Riber C21 *MBE* chamber and transferred in-vacuo into the MgO *UHV* chamber afterwards. The deposition process of the modulation-doped GaAs (001) structure is described in the previous section. After fabricating the modulation-doped GaAs (001), the semicon-

ductor substrates were transferred in-vacuo into the MgO *UHV* chamber. The power of the electron beam was increased after switching on the water cooling of the electron-beam evaporator, the turbo pump and the oscillating crystal. Before injecting the oxygen via the needle valve the pipes were flushed two times with the scroll pump of the fore-vacuum system. In the MgO chamber the background pressure with the additional oxygen gas was about 5×10^{-6} mbar. After the deposition rate monitored with the oscillating crystal stabilized the manipulator with the semiconductor structure on it was turned into the molecular beam. The deposition of MgO occurred at room temperature. Subsequently, the MgO/modulation-doped GaAs (001) structures were transferred in-vacuo into the metal *MBE* chamber. The samples were post-annealed at $250\,°C$ for two hours by setting the heater of the manipulator to the constant output power of $24\,\%$. The annealing was done to improve the crystallinity of the MgO. It is a critical step toward a smooth interface between the MgO and the GaAs[79]. During post-annealing the temperature should not exceed $250\,°C$ to minimize the interdiffusion of oxygen atoms into the GaAs[71]. Afterwards, the deposition of iron occurred at room temperature and at the deposition rate of $0.4\,nm/min$. During deposition the tantalum mask protected the molybdenum block from iron contamination. The was also used to fabricate an iron thickness gradient.

Iron on inverted, modulation-doped InAs heterostructure

Figure 3.7(b) shows the layer design of the iron on inverted, modulation-doped InAs heterostructure. The semiconductor structure consists of an AlAs/GaAs superlattice and a metamorphic $In_xAl_{1-x}As$ buffer to adjust the lattice constant to the one of InAs. On top of it, the silicon-doped $In_{0.75}Al_{0.25}As$ layer provides carriers for the high-mobility electron channel. The thin $In_{0.75}Al_{0.25}As$ spacer separates the charged ions from the electronic active layer. The two-dimensional electron gas is located at the InAs layer between two $In_{0.75}Ga_{0.25}As$ layers and is capped with the $In_{0.75}Al_{0.25}As$ layer. After fabricating the heterostructure, the sample was transferred in-vacuo into the metal *MBE* chamber for the deposition of iron. Thereby, samples were fabricated with iron films of different thickness and iron layer gradients.

Iron on modulation-doped $In_xAl_{1-x}As$

The iron on $In_xAl_{1-x}As$ hybrid structures in Figure 3.7(c) were fabricated using the Riber 32p *MBE* chamber to investigate the interface between iron and the top $In_xAl_{1-x}As$ layer of the modulation-doped InAs heterostructure. The structures consist of an $In_xAl_{1-x}As$ metamorphic buffer with stepwise increasing indium content to adjust the lattice constant, a highly-doped 300 nm-thick $In_xAl_{1-x}As$ back gate with the carrier concentration above

$10^{18}\,\mathrm{cm}^{-3}$ and a low-doped 1μm-thick $\mathrm{In}_x\mathrm{Al}_{1-x}\mathrm{As}$ layer with the carrier concentration of about $5 \times 10^{16}\,\mathrm{cm}^{-3}$. Structures were fabricated with indium contents of $x = 0.65$ and $x = 0.75$. The semiconductor structures were transferred in-vacuo into the metal *MBE* chamber for the deposition of iron. $50\,\mathrm{nm}$-thick iron films were deposited with the deposition rate of $0.4\,\mathrm{nm/min}$ on top of the semiconductor structures.

3.2. Reflection high-energy electron diffraction (*RHEED*)

Reflection high-energy electron diffraction (*RHEED*) is a surface-sensitive technique to analyze in-situ the fabrication of two- and three-dimensional structures. Incorporated in *MBE* chambers it monitors the growth of crystals and conveys crystallographic information. It accesses in-plane as well as out-of-plane lattice constants and the degree of relaxation. The STAIB *RHEED* system of the metal *MBE* chamber consists of an electron gun with an acceleration voltage of up to $15\,\mathrm{kV}$, a phosphor detector screen, image-processing hardware and software to process the data. Thereby, the video setup captures about three frames per second thus collecting sufficient information on the deposition process.
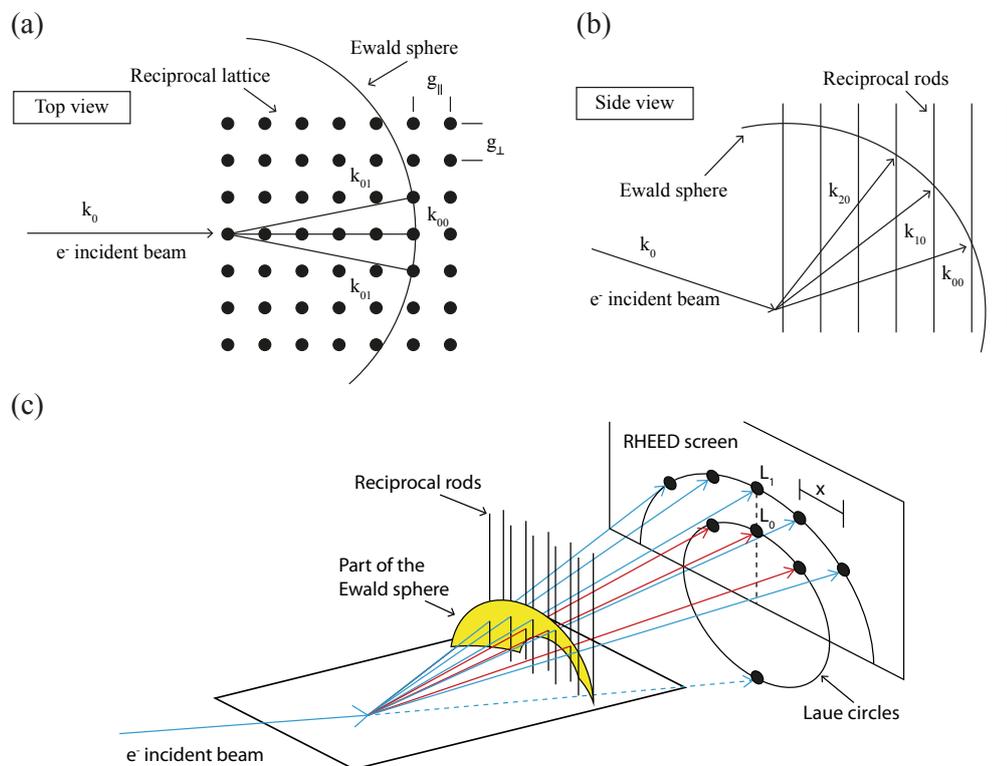
Figure 3.8.: *RHEED* diffraction geometry and construction of the Ewald sphere[80,81].

In glancing-incident-angle geometry, the angle of the incident beam is typically below $5°$. Atoms at the sample surface diffract the electrons so that the beam samples only a few atomic layers beneath the surface. Figure 3.8(a) shows the surface of the sample in reciprocal space. The two-dimensional array of the surface atoms turns into vertical one-dimensional infinite rods as shown in Figure 3.8(b). In kinematical scattering theory, the electrons undergo a single, elastic scattering event. Thereby, the condition for constructive interference is fulfilled when the incident $\vec{k}_0$ and diffracted $\vec{k}'$ beam wavevectors differ by the reciprocal-lattice vector $\vec{G} = \vec{k}' - \vec{k}_0$. According to elastic scattering approximation, the energy of the electrons is conserved so that $|\vec{k}'| = |\vec{k}_0|$. It is expressed by the geometrical construction of the Ewald sphere with radius $|\vec{k}_0| = \frac{1}{\hbar} \cdot \left(2\, m_0\, E + \frac{E^2}{c^2} \right)^{1/2}$. Intensity maxima also called reflexes are projected onto the screen when the Ewald sphere intersects with the rods of the reciprocal space. Figure 3.8(c) shows those reflexes which are located on Laue circles of radius L_n[82]. Further information about the theory of *RHEED* is supplied for example in the work of Wolfgang Braun[83].

The following sections discuss analytical *RHEED* tools which were used to calibrate deposition rates and investigate the *MBE* deposition processes of the fabricated semiconductor/metal hybrid structures.

3.2.1. RHEED oscillations

This method gathers in-situ and real-time information on the dynamics of *MBE* grown crystals[84]. The *RHEED* oscillations were used to calibrate the deposition rate of iron as described in section 3.1.3. The oscillations are generally observed during the layer-by-layer so-called Frank-van der Merwe growth mode. During growth, the surface periodically changes its morphology due to nucleation and coalescence of islands. This change in morphology is observed as intensity oscillations of the specular beam intensity. Figure 3.5 shows an example of time evolution of the specular beam intensity during the deposition of iron on undoped GaAs (001) with a (2×4) reconstructed surface. The intensity of the specular reflex oscillates. Thereby, one oscillation period corresponds to the growth of one monolayer. The intensity is maximal when the growth of one monolayer is completed and drops due to surface roughening. The roughening is caused by mainly diffusive scattering. It reaches a minimum when half a monolayer is completed. During the growth of crystal structures, damping of the oscillating intensity occurs with a much bigger time scale than the oscillation period. Damping is caused by increasing surface roughening but also by geometrical factors. The latter ones are due to the non-uniformity of the impinging rate of atoms across the sample surface. The electron beam averages over a certain area of the

sample surface and thus over a range of frequencies. Another reason might be that the electron beam gets out of focus from the original surface with increasing layer thickness leading to an increasing absorption of electrons[83].

3.2.2. Analysis of in-plane lattice constants

The strain relaxation during the deposition of iron was investigated by accessing its in-plane lattice constant. Figure 3.9(a) shows exemplarily the *RHEED* screen of the $In_{0.75}Al_{0.25}As$ surface reconstruction. The area of the *RHEED* image surrounded by a white rectangle was integrated in the direction of the arrow. This integrated intensity is plotted versus the horizontal pixel position x in Figure 3.9(b). In this graph, the $\vec{k}$ vectors are labeled such that the vector with the smallest angle to the sample surface is of 0th order. The integrated data were fitted using Gaussian functions. The black solid line displays the experimental data, the red lines the sum of the fits and the blue lines the individual fits.
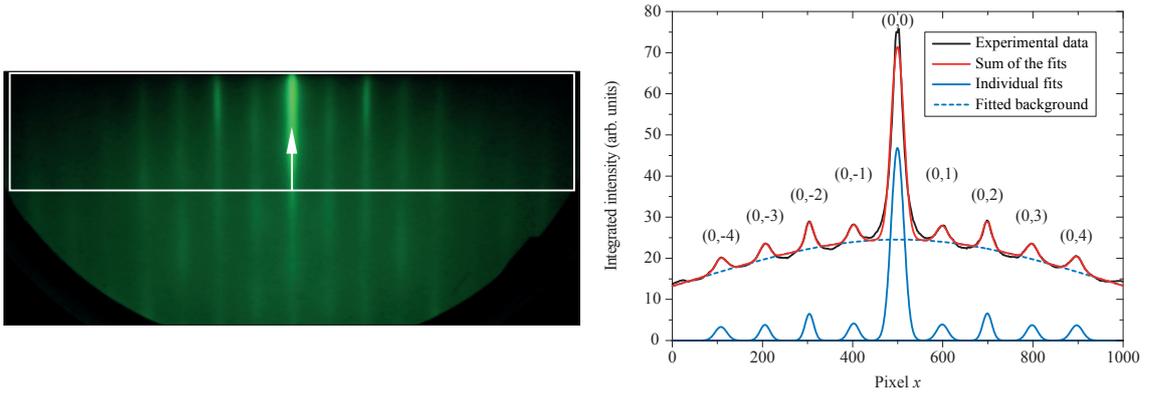
Figure 3.9.: The picture in (a) shows the surface reconstruction of $In_{0.75}Al_{0.25}As$ and the graph in (b) its integrated intensity profile.

The in-plane lattice constant of the deposited films was extracted from the lateral distances between the *RHEED* reflexes and related to the lattice constant of the substrate. Based on this, the in-plane lattice constant was calculated considering the geometry of the *RHEED* setup and applying Bragg's law:

$$a_{film} = a_{substrate} \times \frac{\sin\left(\arctan\left(\frac{x_{substrate}}{L}\right)\right)}{\sin\left(\arctan\left(\frac{x_{film}}{L}\right)\right)} \tag{3.1}$$

$$\text{with} \quad L = \frac{x_{substrate}}{\tan\left(\arcsin\left(\frac{n\lambda}{2\,a_{substrate}}\right)\right)}$$

where $x_{\text{substrate}}$ and x_{film} are peak-to-peak distances between the $(0,0)$ reflex and its direct neighbor, $a_{\text{substrate}}$ the lattice constant of the substrate, λ the wavelength of the electrons at given energy, $n = 1$ the order of diffraction and L the distance sample and *RHEED* screen. The wavelength of $\lambda = \frac{2\pi}{k_0} = 2\pi\hbar \cdot \left(2\, m_0\, E + \frac{E^2}{c^2}\right)^{-1/2} = 1.1131 \cdot 10^{-11}\,\text{m}$ was determined from the acceleration voltage of $12\,\text{kV}$, with relativistic corrections. At this electron energy, the penetration depth in the surface is on the order of a few monolayers, so that it was possible to determine the lattice constant of iron at the surface.

3.3. Electrical four-probe measurements

Four-probe measurements were performed to determine the sheet resistivity of conducting samples. This four-terminal sensing method measures the resistivity independent of the contact resistance between tip and surface of the sample. Figure 3.10 shows a scheme of the setup geometry.
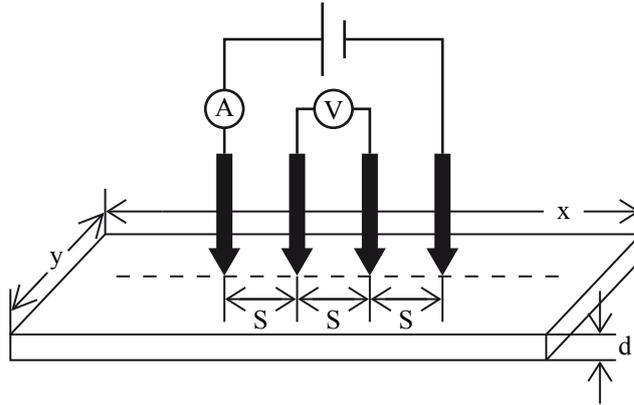
Figure 3.10.: Scheme of the four-probe setup.

The four-probe setup operates as follows: Four gold coated metal tips are aligned equidistant along the dashed line. A voltage is applied at the outer tips, driving a current through the sample. At the same time the voltage drop at the inner tips is measured. Thereby, the distance S between the tips has to be much smaller than the lateral sample size. The tips should be placed at the center of the sample to avoid influences from the edges of the sample.

The specific sheet resistivity ρ_A results from the data of four-probe current-voltage-measurements. The thickness d of the sample can be calculated from the specific sheet resistivity ρ_A if the specific resistivity ρ is known and independent of d:

$$\rho_A = \frac{\pi}{ln(2)} \cdot \frac{V}{I} \qquad \text{with} \quad \rho = \rho_A \cdot d \qquad \Rightarrow \qquad d = \frac{\rho \cdot ln(2)}{\pi} \cdot \frac{I}{V} \qquad (3.2)$$

This four-terminal sensing technique was used to determine the layer thickness of deposited iron and gold films across the area of the sample. In this regard, the specific resistivity ρ was set to the value which complied with the calibrated layer thickness at the center of the wafer. The calibration procedure is described in section 3.1.3. Thus, the four-terminal current-voltage behavior of homogeneous metal films reflects the layer thickness d according to equation 3.2. In these investigations the layer thickness dependency of the specific resistivity was neglected.
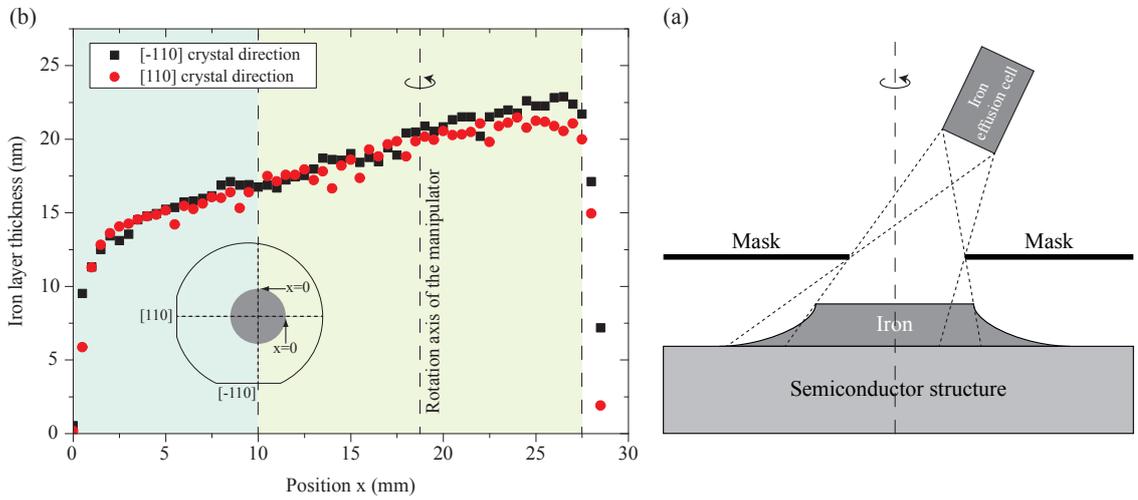
Figure 3.11.: (a) Iron layer thickness on SiO_2 without rotating the sample during deposition. (b) Scheme of a hybrid structure rotated during deposition, the tantalum mask and the iron effusion cell.

Gradients in layer thickness with a homogeneous area at the center of the wafer were fabricated by using the tantalum mask of the metal *MBE* chamber. In this chamber, the effusion cell was installed at the angle of about $20\,^{\circ}$ with respect to the vertical axis of the chamber. In general, the flux density of Knudsen cells decrease with $1/r^2$ so that the rate of arrival atoms is non-uniform across the wafer. In this setup, the position of the maximum particle flux of the iron molecular beam is not at the center of the wafer thus off the rotation axis of the sample holder. This and the non-uniformity of the rate of arrival atoms led to a gradient in layer thickness across the center of the wafer. Figure 3.11(a) shows the layer thickness of an iron film along the deposited area. The sample has not been rotated during the deposition process. The four-probe measurements depict a gradient in layer thickness along two perpendicular crystal directions. In the graph, the dashed line

at $x = 18.5 \, \text{mm}$ displays the rotation axis of the sample holder. If the sample would have been rotated a homogeneous layer thickness would emerge from $x = 10.0 \, \text{mm}$ to $x = 27 \, \text{mm}$ with a gradient from $x = 0 \, \text{mm}$ to $x = 10 \, \text{mm}$. Figure 3.11(b) displays a sketch of the arrangement in the metal *MBE* chamber with the iron effusion cell, the tantalum mask, a semiconductor structure and deposited iron film. During deposition the sample was rotated leading to the homogeneous thickness range and thickness gradient of the iron film.

Figure 3.12 shows four-probe data of iron and gold layers deposited on SiO_2 substrates which were rotated during deposition. SiO_2 substrates were used as they are insulating. Thus, the four-probe experiments determined the resistivity of just the metal films.
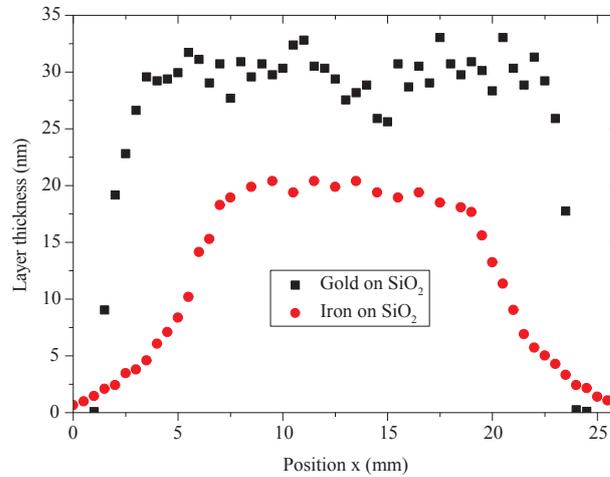
Figure 3.12.: Layer thickness of iron and gold at the center of the SiO_2 wafer.

The iron film on SiO_2 exhibits a homogeneous layer thickness range at the center of the wafer of about $15 \, \text{mm}$ in diameter. The specific resistivity is $0.36 \, \Omega \cdot \text{mm}^2/\text{m}$. This value is in agreement with previous multiple-beam interferometry measurements[85]. The deposited gold on SiO_2 has a larger homogeneous range of about $20 \, \text{mm}$ in diameter and a specific resistivity of $0.22 \, \Omega \cdot \text{mm}^2/\text{m}$. The specific resistivity is larger than calculated value from other groups[86]. The larger homogeneous range of the gold film relative to the iron film is due to the alignment of the crucible in the effusion cell. It is advantageous since the gold covers the iron film to prevent it from oxidation.

3.4. High-resolution X-ray diffraction (*HRXRD*)

Ex-situ, high-resolution X-ray diffraction (*HRXRD*) was applied to investigate the chemical composition and structural properties of the epitaxial fabricated semiconductor and

hybrid structures. The X-ray diffraction technique is non-destructive and does not need any kind of sample preparation. This section is about the experimental *HRXRD* setup, the sample alignment and the X-ray methods which were used to access the properties of the structures. Several books provide further information about X-ray diffraction and analysis of crystal structures[87, 88].
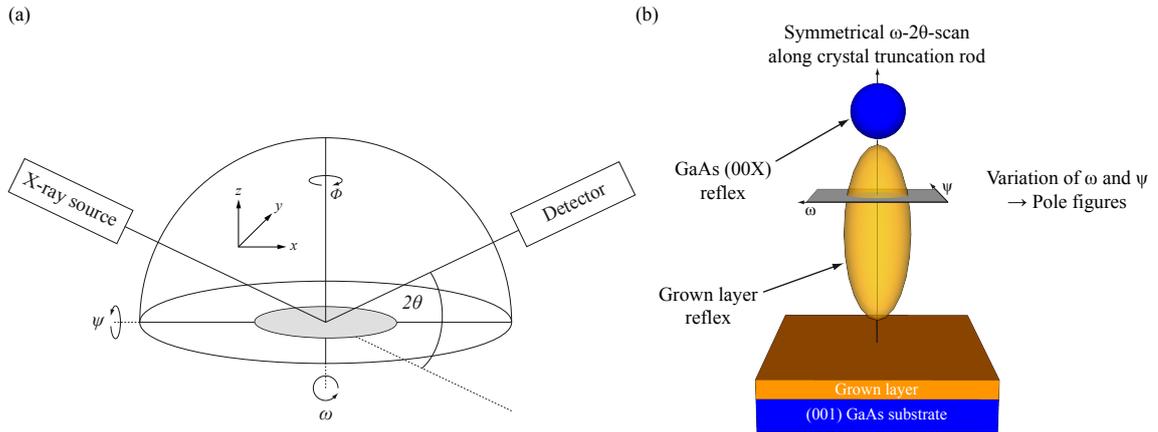
Figure 3.13.: Scheme of (a) the experimental *HRXRD* setup and (b) example of an epitaxial grown layer on (001) GaAs substrate with their reciprocal space reflexes.

3.4.1. Experimental setup

In general, the sample to be analyzed is mounted on a stage and illuminated by an X-ray beam. The stage aligns or moves the sample during the measurements. A detector detects the direct or diffracted beams in a known orientation. Figure 3.13(a) shows a scheme of the experimental setup with its essential components and various alignment and measurement axes. The axis x, y and z position the sample in the beam. The reciprocal space is scanned by tilting the sample by the angles ω and Ψ or the detector by 2θ. The rotation angle Φ can be used to analyze the texture of the sample or perform powder diffraction measurements. Figure 3.13(b) displays as an example X-ray intensities in reciprocal space of a crystalline material on a GaAs (001) substrate. It depicts that the different stage axes can be used to perform certain scans in reciprocal space in order to collect information about the structural properties of the fabricated layer.

In this thesis, the Panalytical X'Pert PRO high-resolution X-ray diffractometer was used to characterize the structures fabricated with the *MBE* chambers. Figure 3.14 shows a picture of the four-circle diffractometer with its components. The X-ray tube (1)

emitted characteristic CuK_α-radiation. The X-ray beam was collimated with a parabolic mirror (2) and optional monochromatized with a $4\times Ge(220)$ monochromator (3). The monochromator filtered the $CuK_{\alpha2}$-radiation so that the $CuK_{\alpha1}$-radiation of higher intensity passed and could be used for the measurements. The samples were glued on a holder mounted on the high-precision goniometer (4). The goniometer tilted and moved the samples in the beam. The direct X-ray beam and diffracted signals were detected by either the proportional point detector PW 3011/20 or the one-dimensional PIXcel detector.
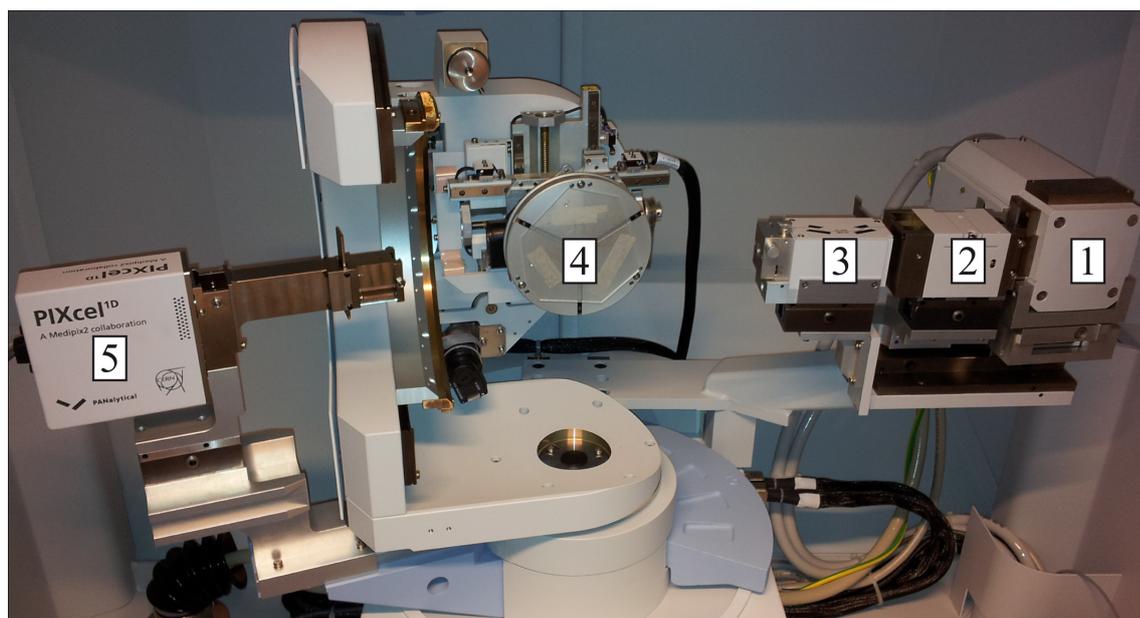
Figure 3.14.: Inside view of the Panalytical X'Pert PRO four circle high-resolution X-ray diffractometer.

3.4.2. Principle of measurements

This section explains procedures of aligning the sample, calibrating the goniometer zero positions and performing a scan or series of scans. Different methods of X-ray diffraction analysis are described which were used to characterize the crystal structures and accessed lattice constants, layer thickness, texture and degree of relaxation.

All measurements were performed with an acceleration voltage and electrode current of the X-ray tube of $40\,kV$ and $40\,mA$, respectively. The wavelength of the X-ray is in the order of atomic distances thus an excellent probe to investigate crystal structures. In the case of X-ray diffraction, the shell electrons of the lattice atoms diffract the high-energy photons. The X-rays are interacting weakly with the atomic nuclei. In the classical picture, the

incident electromagnetic wave excites the shell electrons of the sample atoms which begin to oscillate. The oscillating electrons re-radiate waves with the same frequency. These secondary waves are interfering with each other resulting in typical diffraction patterns with intensity maxima and minima. In this regard, Bragg's law describes the condition for constructive interference from a set of discrete parallel planes separated by the lattice spacing d. A Bragg reflex occurs when the path difference $2\,d \cdot \sin(\theta)$ is an integer value n of the wavelength λ[87]:

$$n \cdot \lambda \;\; = \;\; 2\,d \cdot \sin(\theta) \tag{3.3}$$

$$d_{h,k,l}^2 \;\; = \;\; \frac{a^2}{h^2 + k^k + l^2} \quad \text{(Cubic unit cell)}$$

where n is the order of diffraction, θ the angle between incident beam and the lattice planes, a the lattice constant and h, k and l the Miller indices.

Sample alignment

In the first step, the sample was aligned in the X-ray beam to provide a homogeneous illumination during measurements. The sample was glued with either candle wax or double-sided tape to the sample holder. The alignment began by placing the 2θ-axis on an absolute scale. An attenuator was required due to the high intensity of the direct beam. Thereby, the detector scanned through the $2\theta = 0$ position while the sample is out of the incident beam $z = 0$. Subsequently, the 2θ peak position was set to zero. In the next step, the ω angle was placed to an absolute scale. Thereby, the sample was first adjusted in z-direction so that the intensity at $2\theta = 0$ was half the one of the direct beam intensity. Now, the sample could still be tilted by an angle ω. Therefore, an ω-scan was performed and the peak position set to zero. Finally, another z-scan readjusted the intensity to half the one of the direct beam intensity.

$\omega - 2\theta$ scan

The ω-2θ or radial scan in reciprocal space was used to determine the out of surface plane lattice constant and strain of epitaxial structures. Figure 3.15 shows the general case when changing the reciprocal space vector Q by varying the angles ω and 2θ. Thereby, the step size of 2θ is twice the size of the one of the angle ω. If $\omega = \theta$ the scan is
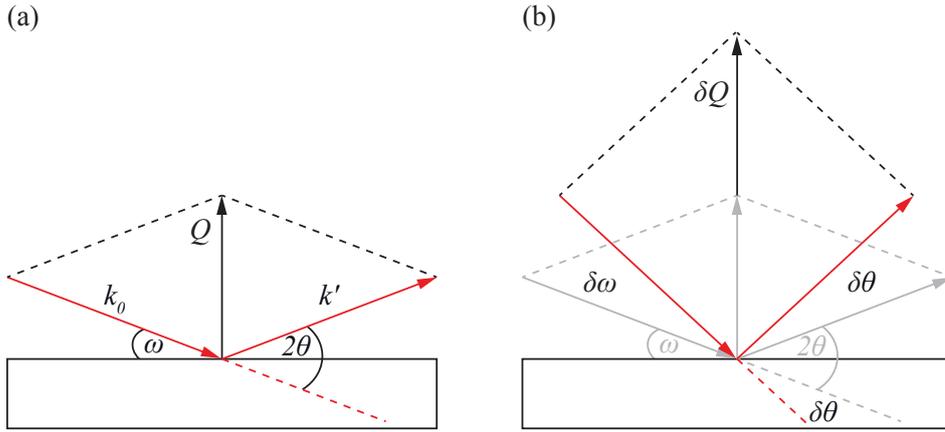
Figure 3.15.: Illustration of the general ω-2θ scan in reciprocal space.

symmetrical along the crystal truncation rod. It is called offset or asymmetrical scan if $\omega \neq \theta$. The ω-2θ measurements were performed by collimating the incident X-ray beam by a parabolic mirror, restricting it by the $1/2°$ divergence slit and $1.4\,\text{mm}$ antiscatter slit and monochromizing it with the $4\times\text{Ge}$ (220) monochromator. The point detector with the triple axis $3\times\text{Ge}$ (220) analyzer collected the diffracted beams. The symmetrical ω-2θ scans were performed relative to the absolute peak position of the GaAs (004) with $\omega = 33.02552°$ and $2\theta = 66.05105°$.

The dependence of the lattice constant on the composition of compound semiconductor alloys like $\text{In}_x\text{Al}_{1-x}\text{As}$ is described in good approximation by Vegard's law[89,90]. It establishes a linear relation between the lattice constant of an alloy and the composition of the constituent elements at a constant temperature. In the simplest case of a binary compound A-B the expression is:

$$a_{AB} = a_B + x \cdot (a_A - a_B) \tag{3.4}$$

The lattice constant of $\text{In}_x\text{Al}_{1-x}\text{As}$ was calculated by Vagard's law from the nominal indium content of the composition according to the fabrication protocol and the Riber 32p *MBE* system calibration. In this regard, the degree of relaxation of the material system was considered via a symmetrical and an asymmetrical scan and determined with the Poisson ratio of 0.325[91].

Specular X-ray reflectivity

Specular x-ray reflectivity (XRR) is a method to determine the density of materials, the layer thickness, the surface as well as interface roughness of thin films or multilayers[92–95]. In specular XRR configuration the reciprocal space vector Q is perpendicular to the surface of the structure and is far away from material diffraction peaks. Therefore, it contains no information about in-plane properties and crystalline structures of the layers. Figure 3.16 shows a simulated XRR curve of a 20 nm-thick iron film on a GaAs substrate. The shape and course of the curve contains information about the properties of the layer stack along the crystal truncation rod.
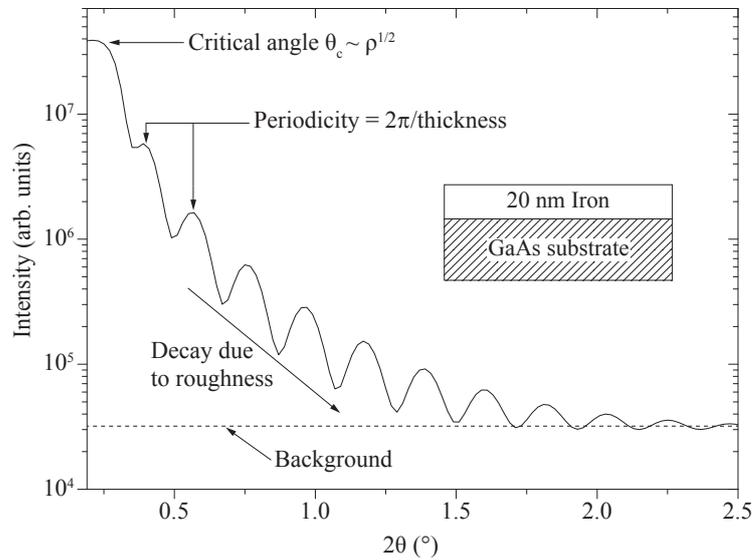
Figure 3.16.: Simulated *XRR* curve of an iron film on GaAs substrate.

XRR scans were performed in symmetrical θ-2θ configuration whereby the angles θ are much smaller than in θ-2θ diffraction geometry. In the region of small Q vectors the reflectivity curves are analyzed by using the classical Fresnel equations. Incident X-rays are totally reflected from the surface for angles smaller than the critical angle θ_c. This reflection at the interface depends on the difference in electron densities of the neighboring materials. The mass density ρ of the material arises from the critical angle:

$$\theta_c = \sqrt{\frac{r_0\,\lambda^2}{\pi}\,N_A\,\frac{(Z + f')}{A} \cdot \rho} \tag{3.5}$$

where r_0 is the classical electron radius, λ the wavelength of the X-ray, N_A the Avogadrozahl, Z the atomic number, A the atomic mass and f' the first order correction term

of the atomic scattering factor. The critical angle θ_c is in the range of 0.1° to 0.6° for most materials.

X-rays will penetrate into the material if the incident angle θ is larger than the critical angle θ_c. Angle-dependent interferences occur due to reflection of the waves at the interfaces of the layer stack. These interference Kiessig fringes[96] can be used to determine the thickness d of thin films. Thereby, the thickness is inversely proportional to the periodicity of the fringes:

$$d = \frac{\lambda \, (n_i + 1/2)}{2 \, \sqrt{\sin^2 (\theta_i) - \theta_c^2}} \tag{3.6}$$

where θ_i the angle of the i-th interference maximum and n_i an integer number[97]. The Fourier analysis of reflectivity curves is another way to determine the thickness of thin films or of multilayers also[98]. Moreover, effects like absorption or inelastic scattering decrease the intensity of the reflectivity curves for $\theta > \theta_c$. Another reason for the decay is diffusive scattering from rough interfaces.

Before specular reflectivity scans were performed and after the first alignment of the sample described in section 3.4.2, the samples were aligned more precisely in the beam. This was done by setting the angles ω and 2θ to the peak position of the specular reflex. Subsequently, the scans were performed symmetrically with $\omega = \theta$ in the range from $\theta = 0°$ to about $\theta = 3°$ as described above. The experimental reflectivity curves were simulated and analyzed using the program RCRefSimW.

Pole figure texture analysis

The texture or crystal orientation of the lattice planes of epitaxial structures relative to planes of the substrate were investigated by using Pole figures. Pole figures were constructed by collecting intensities either in ϕ scans at different ψ angles or in ω scans at different angles of ϕ[99]. The incident x-ray beam was collimated by a parabolic mirror, restricted by the 1/8° divergence slit and 1.4 mm antiscatter slit and monochromatized by the 4×Ge (220) monochromator. The diffracted beams were collected with the one-dimensional PIXcel detector.

3.5. Magneto-optic Kerr effect microscopy

This section comprises an overview about the magneto-optic Kerr effect, the experimental *MOKE* setup and the measurement procedures. Magneto-optic Kerr effect (*MOKE*) measurements were performed in cooperation with Stephan Martens from the group of professor K. Nielsch. The investigations accessed the in-plane magnetization and magnetic anisotropies[100] of the fabricated hybrid structures.
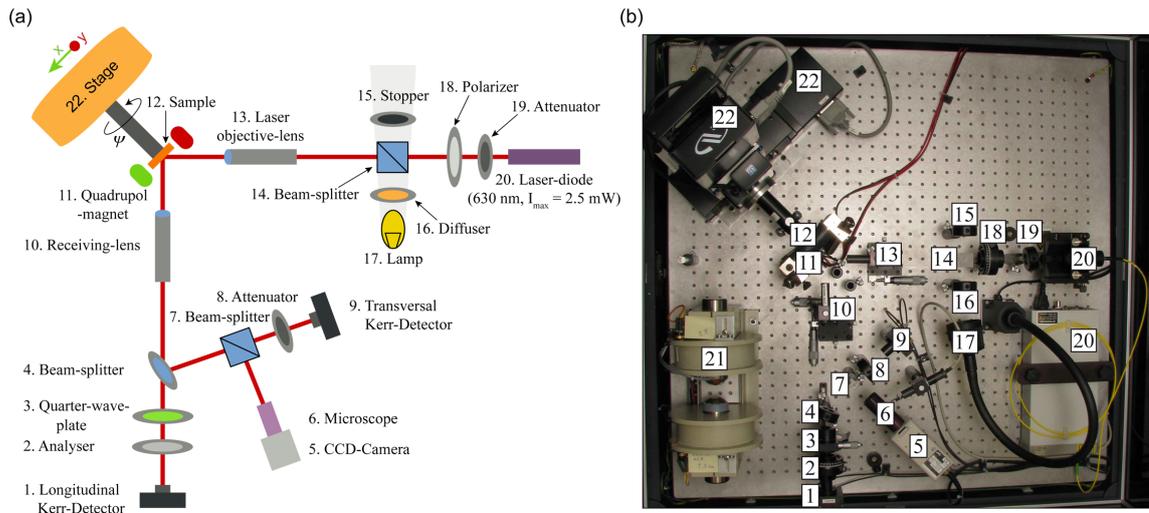
Figure 3.17.: (a) Sketch of the *MOKE* setup components and (b) top view of the experimental setup.

3.5.1. Experimental setup

Figure 3.17 shows (a) a sketch and (b) top view of the *MOKE* setup. The setup was used to investigate the in-plane magnetic properties of the fabricated hybrid structures. The magnetometer has two optical systems which were used to conduct the *MOKE* measurements and image the surface of the sample. Light with a wavelength of 630 nm enters the system from a temperature stabilized laser diode with a maximal output power of 2.5 mW (20.). The laser light goes through the polarizer (18.) to generate s- or p-polarized light and is focused by the objective (13.) lens onto the sample surface. The sample is mounted on the cylindrical sample holder tilted 45° to the optical axis. The stage (22.) moves the sample in x- and y-direction and rotates it around the angle ψ. The light reflected from the sample surface is collected and focused with the receiving lens (10.). The beam splitter (4.) sends approximately 50 % in direction of the longitudinal Kerr detector (1.) and the other half in direction of the transversal Kerr detector (9.). An attenuator (8.) prevents the transversal Kerr detector from saturating. In the case of the longitudinal path the

analyzer is used to attenuate the p-polarized component of the reflected light and detect the Kerr signal. In regard to measure the Kerr-rotation the quarter-wave plate (3.) has to be removed and inserted to measure the Kerr-ellipticity. Furthermore, the lamp with white light (17.), attenuator (19.), diffuser (16.), beam-splitters (7., 14.), stopper (15.), microscope (6.), CCD-camera (5.) are used to image the surface of the sample and adjust the laser spot onto the sample surface.

A quadrupole electromagnet (11.) generated and applied an in-plane magnetic field to saturate the samples. The coils of the electromagnet were adjusted so that $4 \times 4\,\mathrm{mm}^2$ big samples could be placed in the magnetic field. The maximal magnetic field at the center of the sample was about $\pm\,90\,\mathrm{mT}$ at the field sweeping frequency of $f = 7.2\,\mathrm{Hz}$.

Relation between measured intensity and magnetization

The following describes the relation between the measured intensity of the light reflected from the surface of the sample and the Kerr rotation as well as Kerr ellipticity[101]. The working principle of the above described *MOKE* setup is derived in context of the macroscopic dielectric theory[102]. In this theory, the description is based on analyzing the dielectric properties of a medium by the antisymmetric, off-diagonal elements in the dielectric tensor. If the incident light is p-polarized and the sample is non-magnetic the light will be reflected purely p-polarized. But if the sample is ferromagnetic the reflected light also contains an s-polarized component E_s in addition to the dominant p-polarized component of the electric field E_p. The relation E_s/E_p is described as the complex Kerr amplitude $\phi_{K,p}$:

$$\phi_{K,p} = \phi_p^{'} + i\,\phi_p^{''} = \frac{r_{sp}}{r_{pp}} = \frac{E_s}{E_p} \tag{3.7}$$

where r_{sp} and r_{pp} are the Fresnel coefficients for the s- and p-component of the reflected light, $\phi^{'}$ the Kerr rotation and $\phi^{''}$ the Kerr ellipticity. In the experiments, a polarizer/analyzer was placed in front of the photodetector to eliminate the p-component and measure the s-component of the reflected light. This method has two disadvantages: First, the detector measures the intensity of the light $I \sim |E_s|^2$. Thus, the measured quantity is proportional to the square of the magnetization $I \sim M^2$. Second, it is not possible to determine the absolute value of the Kerr rotation. This can be circumvented by setting the polarizer at a small angle δ from the p-axis:

$$I \;=\; |E_p\,sin(\delta) + E_s\,cos(\delta)|^2 \approx |E_p\,\delta + E_s|^2$$

with equation 3.7

$$\Rightarrow \qquad I \;=\; \underbrace{|E_p|^2\,\delta^2}_{I_0}\left(1 + \frac{2\,\phi^{'}}{\delta}\right) \tag{3.8}$$

where the Kerr rotation $\phi^{'}$ depends linearly on the magnetization of the sample. The plot of the reflected intensity as a function of the external magnetic field would show the hysteresis loop of the film magnetization.

In the case of an optically anisotropic medium, birefringence can occur and lead to an s-component of the reflected light. The quarter-wave plate is used, not only to measure the Kerr ellipticity but also to cancel the birefringence. The plate leads to a phase shift of $\pi/2$ between the s- and p-component of the light. The Kerr rotation and Kerr ellipticity in equation 3.7 are interchanged and the measured intensity directly proportional to the Kerr ellipticity $\phi^{''}$.

$$I = \underbrace{|E_p|^2\,\delta^2}_{I_0}\left(1 - \frac{2\,\phi^{''}}{\delta}\right) \tag{3.9}$$

3.5.2. Measurement procedures and analysis

The *MOKE* setup detects the longitudinal and transversal Kerr signals simultaneously to access the in-plane magnetization of thin magnetic films. Figure 3.18 displays sketches of (a) longitudinal and (b) transversal *MOKE* geometries. In these *MOKE* configuration the magnetization vector is (a) directed parallel to the surface and the plane of incidence and (b) directed parallel to the surface but perpendicular to the plane of incidence. In the latter case, the intensity of the reflected light changes instead of the Kerr rotation depending on the absolute value of the magnetization.

The longitudinal Kerr detector detects the sum of the longitudinal and transversal Kerr signals so that the transversal Kerr signal has to be subtracted from the longitudinal one. In the calibration procedure, the normalized transversal Kerr signal is multiplied by the DC voltage ratio in detected and saturated longitudinal and transversal Kerr signals
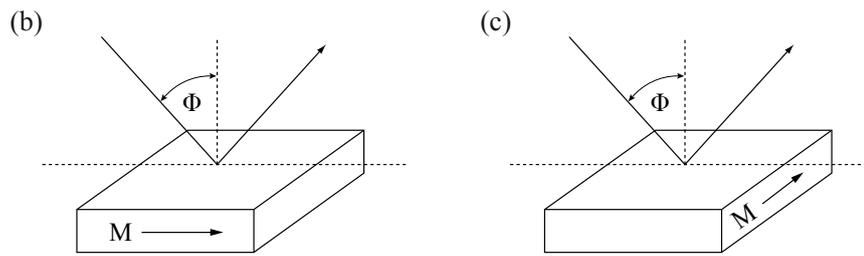
Figure 3.18.: Schematic of the different *MOKE* geometries: (a) longitudinal and (b) transversal *MOKE*.

and subtracted from the longitudinal Kerr signal. Figure 3.19 shows and the following describes this calibration procedure: The first step is to identify an in-plane magnetic easy axis of the ferromagnetic film. In longitudinal *MOKE* configuration, the magnetic field is then swept in direction of this magnetic easy axis. Figure 3.19(a) displays examples of the longitudinal and transversal Kerr detector signals in this configuration. The longitudinal one shows a sharp hysteresis with maximal voltages of $V_L = \pm 20\,\mathrm{mV}$. All further with the longitudinal detector detected data will be normalized with these saturation signals to $M_L/M_S = M_{L,N}$. The transversal Kerr detector shows no signal.
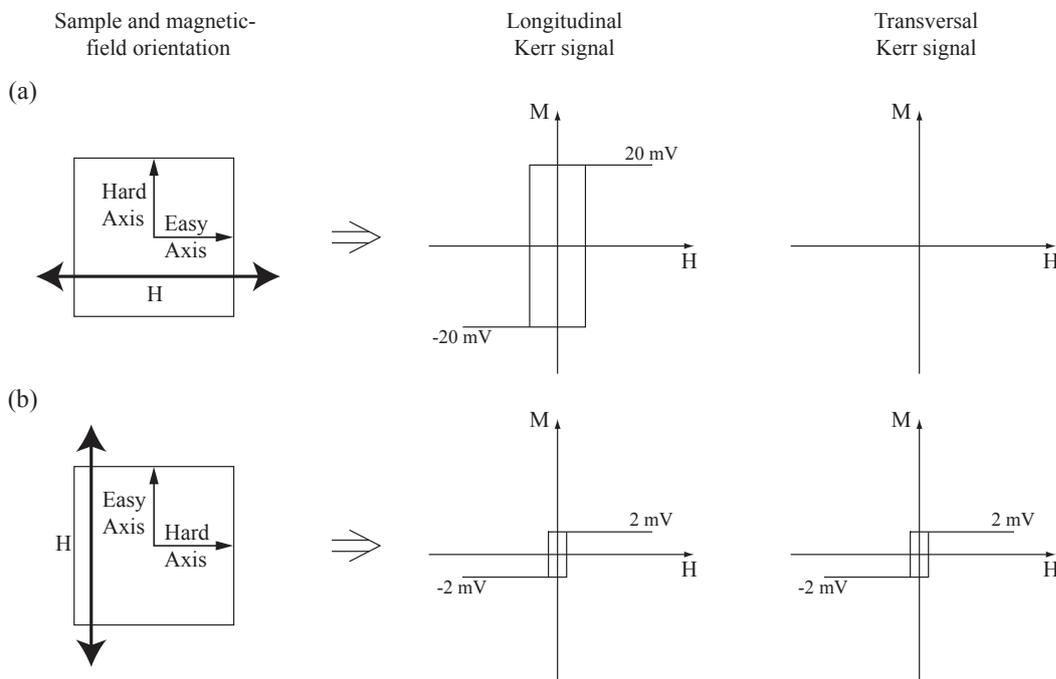
Figure 3.19.: Calibration procedure in (a) longitudinal and (b) transversal *MOKE* configuration.

In the second step, the magnetic field is swept in transversal *MOKE* configuration as shown in Figure 3.19(b). Both detectors detect signals look alike but with much lower intensity than in longitudinal configuration. The maximal voltages of $V_T = \pm 2\,\text{mV}$ normalize all further with the transversal Kerr detector detected data to $M_T/M_S = M_{T,N}$. These measurements depict that the longitudinal detector also detects the transversal signal. In this regard, the normalized transveral detector signals were multiplied by the DC voltage ratio between the longitudinal and transversal detector signals (usually in the order of $V_T/V_L = 1/10$) and subtracted from the normalized longitudinal detector signal.

In-plane magnetic axes of the ferromagnetic films

Previous studies of the systems iron on GaAs[13,103], iron on MgO[104] and iron on $\text{In}_{0.52}\text{Al}_{0.48}\text{As}$[105] reported negligible out-of-plane components of the magnetization. This is due to the magnetic shape anisotropy. Thus, the investigations in this thesis focused on the in-plane magnetic properties of the fabricated hybrid systems. Magnetic-field dependent longitudinal and transversal Kerr signals were detected to access the in-plane magnetic properties of the fabricated hybrid structures. The magnetic field sweeps were performed at different in-plane crystal direction from $\psi = 0\,°$ to $\psi = 360\,°$ in steps of $5\,°$. The samples were illuminated with p-polarized light while sweeping the magnetic field from the maximal negative to the maximal positive value. The laser was focused to a $4\,\mu\text{m}$ spot in diameter on the surface of the samples. The laser spot was positioned at the rotation axis of the stage so that always the same area was probed during the measurements at different angles ψ. Dust particles or structures on the surface of the samples were used to guide this adjustment.

Reversal process and magnetic domains

The reversal process of the normalized in-plane magnetization vector $\vec{M}_N(\psi)$ was displayed by constructing polar plots. Thereby, the normalized longitudinal signal $\left(M_{L,N}/|\vec{M}_N(\psi)| \right) = cos(\psi)$ was plotted versus the normalized transversal signal $\left(M_{T,N}/|\vec{M}_N(\psi)| \right) = sin(\psi)$ with the in-plane rotation angle ψ of the sample. The reversal process of the magnetization vector can be described by the Stoner-Wohlfarth model[106]. This single domain-model is only valid for coherent reversal rotation of the magnetization. But, a single-domain spin state can transit via a domain structure into another single-domain spin state during the reversal process. The transition between those two single-domain states is explained by unpinning of domain walls and sweeping them across the magnetic film. In this simple model, multidomain states are not defined but the energy before domain splitting and after the formation of single-domain states[107].

During the reversal process of the magnetization vector, monodomain states were assumed in saturation magnetization M_S of the material[108]. Single-domain states could be identified if the magnitude of the magnetization vector remained constant during magnetic field sweeps. Domain splitting could be identified by a reduced magnitude of the vector. In the phase of domain splitting the magnetic moments are mostly aligned parallel to in-plane magnetic easy axes to minimize the energy of the multidomain structure[104,109].

In-plane magnetic anisotropy constants

Once the symmetry of the magnetic in-plane anisotropy is known, it is possible to determine the uniaxial anisotropy K_U[110,111] and cubic anisotropy K_4[105,112] constants. In this analyzes, the hard axis hysteresis loops in the $[\bar{1}10]$ crystal direction were fitted to an expression of the inverted magnetization loop $H(m_L)$ obtained by minimizing the magnetic energy density[113]:

$$H\left(M_{L,N}\right) = \frac{2\,K_4\,M_{L,N}}{\mu_0\,M_S} \cdot \left(\frac{K_U}{K_4} + 2\,M_{L,N}^2 - 1\right) \tag{3.10}$$

where $M_{L,N} = M_L/M_S$ is the magnetization component in direction of the applied field normalized to the saturation magnetization M_S and μ_0 the vacuum permeability. The anisotropy constants were extracted by assuming that the saturation magnetization of iron per unit volume at room temperature is $M_S = 1.72 \cdot 10^6\,\mathrm{A/m}$[114].

In this thesis, the thickness dependence of the in-plane anisotropies was studied by conducting Kerr signals along an iron layer thickness gradient. The gradient was fabricated with an especially designed tantalum mask in the metal *MBE* chamber. The method to determine the thickness of the gradient is described in section 3.3. The Kerr measurements were performed with 5 mm wide stripes cleaved along the uniaxial hard axis of the materials. Hysteresis loops were conducted for thicknesses between 0 nm and 20 nm since the penetration depth of the laser is restricted to about 25 nm depending on the material. In order to disclose dependencies, the anisotropy constants were plotted versus the position on the wafer and the iron layer thickness.

Following facts may limit the precision with which the layer thickness along the thickness gradient was determined: First, the *MOKE* setup averages over the distance of 4 μm whereby the four-Probe setup averages over an estimated distance between 1 mm and 2 mm. This fact results in discrepancies between the iron layer thickness at the position x

of the *MOKE* spot on the wafer and the position x of the four-terminal probes. Second, the thickness dependence of the specific resistivity of iron is not known. The specific resistivity might increase for smaller layer thicknesses[86]. This would change the shape of the curve in Figure 3.12(b). Third, the flat surface of the GaAs and the cross-hatch morphology of the $In_{0.75}Al_{0.25}As$ might lead to different nucleation behavior of the deposited material on these substrates. At the early stage of deposition, the growth and coalescence of islands might vary. This leads to varying thicknesses determined with the four-probe setup despite the fact that the amount of deposited material is the same.

3.6. Fabrication process of transport structures

This section summarizes the fabrication processes of the structures which were used to perform magneto-transport and voltage-current measurements. In this regard, optical lithography with a shadow mask was used to fabricate structure in the micrometer range[77]. The mask consists of a glass substrate on which a structured chromium film defines the transport structures. The chromium absorbs and reflects the light so that the resist gets exposed through just the transparent areas of the mask. The resolution of this method in contact is restricted by diffraction at the mask as well as the thickness, homogeneity and contrast of the resist. It is defined by the minimum feature size (*MFS*):

$$\mathrm{MFS} = \sqrt{d \cdot \lambda},$$

where d is the thickness of the resist and λ the wavelength of the light. In this thesis, the „Karl Süss MJB4" mask aligner exposure optics provided ultraviolet light with a wavelength of $365\,\mathrm{nm}$. The samples were exposed in the vacuum contact printing mode. Advantages of this mode are the high resolution of about $800\,\mathrm{nm}$ and that tilts between sample and mask are reduced by the vacuum. It is disadvantageous that mask and sample can be damaged by the contact. It might also lead to defects in the printed structures.

L-Hallbar structures for magneto-transport measurements

Microscopic L-Hallbar structures were transferred with photolithography to inverted, modulation-doped InAs heterostructures to perform low-temperature magneto-transport measurements. Figure 3.20 shows the design of the L-Hallbar. The wafers with the fabricated structures were cleaved into pieces of $5 \times 5\,\mathrm{mm}^2$. In the first photolithography step, the positive resist S1813 was spin-coated onto the sample surface at $6000\,\mathrm{rpm}$ for $60\,\mathrm{s}$. The sample with the resist was then soft baked at $115\,°\mathrm{C}$ for $60\,\mathrm{s}$. Afterwards, the resist
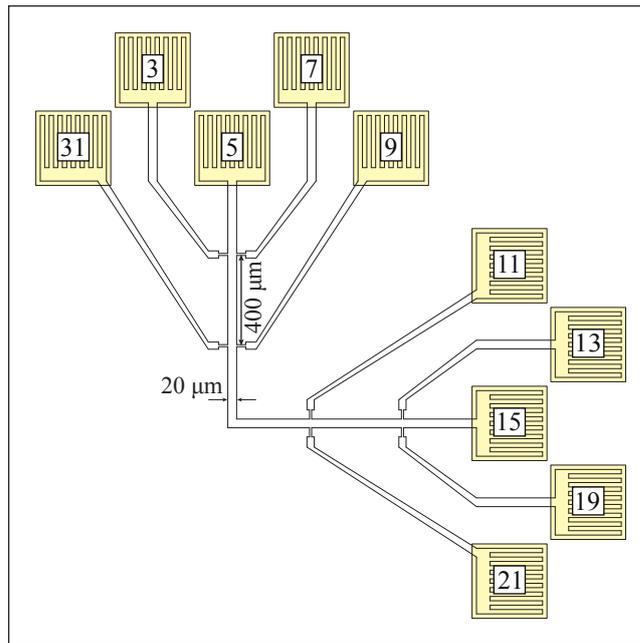
Figure 3.20.: Design of the L-Hallbar structure. During magneto-transport measurements contacts 5 and 15 are used to drive a current through the structure and 3, 7, 9, 11, 13, 19, 21 and 31 to measure off the lateral and longitudinal voltages.

was exposed through the L-Hallbar patterned mask for 7 s and developed with MF319 for 45 s. The developing process was stopped with distilled water. The samples were then transferred into diluted H_2SO_4:H_2O_2:H_2O (500:10:1) for 60 s while stirring with the magnetic mixer. This defined the L-Hallbar structure whereby the etching depth is roughly 60 nm. In the last photolithography step, the resist S1813 was used to fabricate 50 nm-thick $Au_{0.88}Ge_{0.12}$ bonding pads by also using thermal evaporation and performing the lift-off in acetone. The structured samples were then glued on a chip carrier. In the last step, the $Au_{0.88}Ge_{0.12}$ pads were wire-bonded to the gold contacts of the chip carrier.

Circle structures for current-voltage measurements

The circle structures in Figure 3.21 were used to perform current-voltage measurements. The structures were transferred with photolithography to the fabricated hybrid structures in Figure 3.7. This circle structure was transferred to all fabricated hybrid structures to investigate the electrical properties of their interfaces.

The first photolithography step defined the iron contacts. The negative resist ma-N 1405 was spin-coated onto the sample at 3000 rpm for 30 s. It was then soft baked at 100 °C for 60 s. Afterwards, the resist was exposed through the circle patterned mask for

$10\,\mathrm{s}$ and developed with ma-D 533s for $15\,\mathrm{s}$. The developing process was stopped with distilled water. The circle shaped iron contacts were etched in diluted hydrochloride acid ($HCl:H_2O$=1:20) while stirring with the magnetic mixer. Typical etch rates were $0.1\,\mathrm{nm/s}$. The process was stopped with distilled water.

In the case of iron on modulation-doped GaAs (001), the sample was then transferred into diluted sulphuric acid ($H_2SO_4:H_2O_2:H_2O$=500:10:1; etch rate: $60\,\mathrm{nm/min}$) to remove the highly-doped GaAs layer. The remaining resist ma-N 1405 was removed with acetone and isopropanol. In the next step, the positive resist S1813, thermal evaporation and lift-off in acetone was used to fabricate $50\,\mathrm{nm}$-thick $Au_{0.88}Ge_{0.12}$ circle structures.
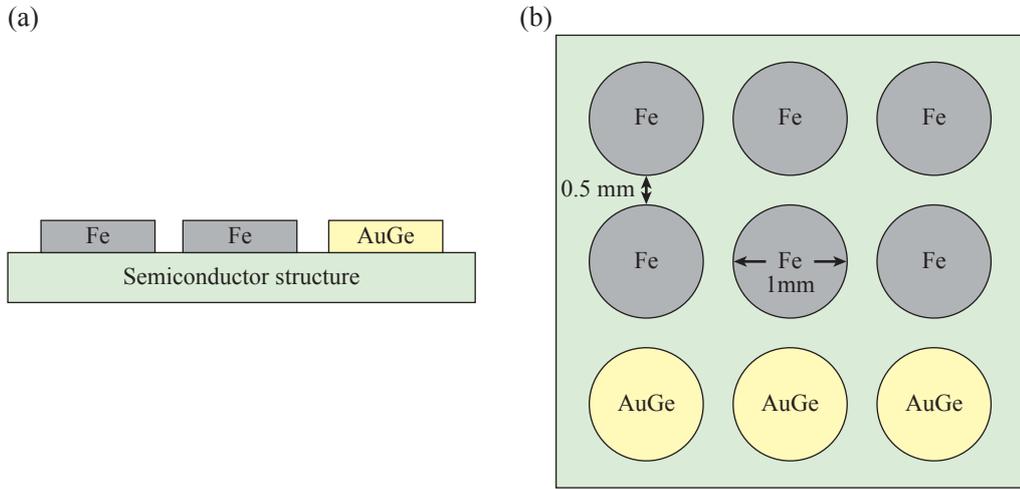
Figure 3.21.: Sample design of the circle structure: (a) side view and (b) top view.

In the case of iron on MgO on modulation-doped GaAs (001), the samples were transferred into diluted sulphuric acid ($H_2SO_4:H_2O$=100:11) for $30\,\mathrm{s}$ to remove the insulating MgO layer. The samples were then transferred into diluted sulphuric acid ($H_2SO_4:H_2O_2:H_2O$=500:10:1; etch rate: $60\,\mathrm{nm/min}$) to remove the highly-doped GaAs layer. The remaining resist ma-N 1405 was removed with acetone and isopropanol. In the next step, the positive resist S1813, thermal evaporation and lift-off in acetone was used to fabricate $50\,\mathrm{nm}$-thick $Au_{0.88}Ge_{0.12}$ circle structures.

In the case of the iron on $In_xAl_{1-x}As$ structures, the remaining resist ma-N 1405 was removed after the iron etch step with acetone and isopropanol. In the next step, the positive resist S1813 was used to define circle structures. The samples were then transferred into diluted sulphuric acid ($H_2SO_4:H_2O_2:H_2O$=500:10:1; etch rate: $60\,\mathrm{nm/min}$) to access the

highly-doped $In_xAl_{1-x}As$ layer. Subsequently, thermal evaporation and lift-off in acetone was used to fabricate 50 nm-thick $Au_{0.88}Ge_{0.12}$ circle structures on top of the highly-doped $In_xAl_{1-x}As$ layer.

In the last steps, the structured samples were glued on chip carriers and the iron and $Au_{0.88}Ge_{0.12}$ circles wire-bonded to the gold contacts of the chip carrier.

3.7. Low-temperature and temperature-dependent transport measurements

The performed low-temperature measurements can be divided into two categories. The first category comprises the magneto-transport measurements on inverted, modulation-doped InAs heterostructures. These measurements characterize the electrical properties of the inverted, modulation-doped InAs heterostructures, such as electron mobility and carrier concentration. Figure 3.22 shows the block diagram of the experimental setup. The dashed lines display general purpose interface bus (*GPIB*) connections between the instruments and the computer and the solid lines connections between the instruments and the sample.
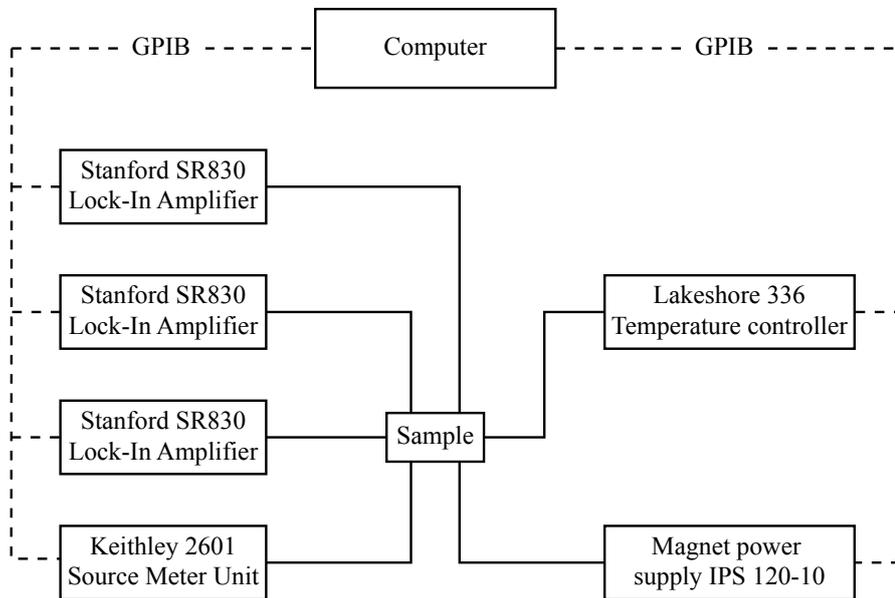
Figure 3.22.: Block diagram of the experimental setup for magneto-transport measurements.

The structured sample was mounted on a holder and loaded into an Oxford helium cryostat with a maximum magnetic field of $\pm 7.7\,T$. The temperature was controlled

by the Lakeshore 336 controller and the superconducting magnet by the IPS 120-10 power supply. Stanford SR-380 lock-in technique was used to perform the electrical measurements. The Keithley source meter unit 2601 applied a voltage to a light emitting diode with the wavelength of $\sim 940\,\text{nm}$ to increase the carrier concentration of the two-dimensional electron gas embedded in the high-mobility InAs heterostructure. During measurements, the current of $100\,\text{nA}$ was flowing from contact five to contact fifteen of the L-Hallbar structure by using a $100\,\text{M}\Omega$ series resistor. The lateral and longitudinal AC voltages were measured off at contacts 3, 7, 9, 11, 13, 19, 21 or 31. The contact numbers are shown in Figure 3.20. During measurement, the surface of the sample was aligned perpendicular to the magnetic field which is swept from $-7.7\,\text{T}$ to $7.7\,\text{T}$. A computer with LabView software and *GPIB* control automated the experiments.

The second category comprises the current-voltage measurements which were conducted with the closed cycle cryostat on the hybrid diode depicted in Figure 3.21. Sample temperature and bias current were varied to study the electrical properties of the interfaces of the hybrid structures in Figure 3.7. Figure 3.23 shows a block diagram of the experimental setup.
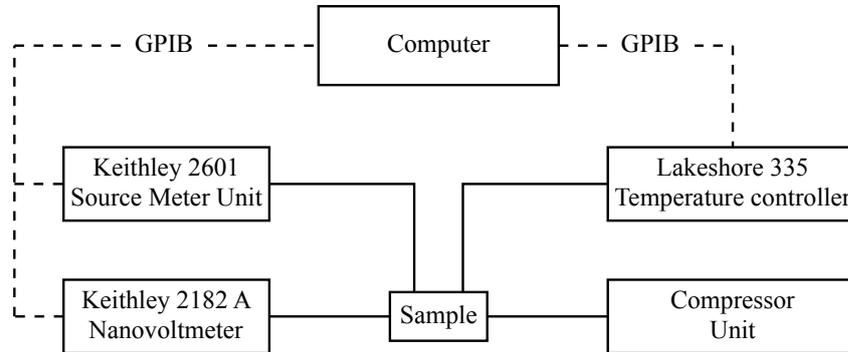
Figure 3.23.: Block diagram of the experimental setup for current-voltage measurements.

The sample was mounted on the cold head of the cryostat. The closed cycle cryostat combined with the heater kept the temperature of the sample between $4\,\text{K}$ and room temperature. The temperature was controlled by the Lakeshore 335 controller. The current-voltage structures, discussed in section 3.6 were measured in two-terminal. A Keithley 2601 source meter unit applied DC voltages of $\pm 1\,\text{V}$ and $\pm 5\,\text{V}$ with step sizes of $1\,\text{mV}$ and $5\,\text{mV}$, respectively. The voltages between the Fe-Fe, AuGe-AuGe and Fe-AuGe contacts were detected by the Keithley 2182A nanovoltmeter. A computer with LabView software and *GPIB* control automated the experiments.

4. Results and discussion

The significant material differences between ferromagnets and semiconductors can lead to major disadvantages in regard to spin-injection and spin-detection experiments as discussed in chapter 1. The fabrication of ferromagnetic metal/semiconductor hybrid structures is challenging where the process parameters have an impact on the properties of their interfaces. Relaxation mechanisms during deposition lead to crystal defects and might degrade the structural and electrical properties of the structures. Also magnetic axes and magnetic anisotropies of the ferromagnet, the behavior of magnetic domains during external magnetic field sweeps and electrical parameters as the applied voltage, current and interfacial resistance are crucial factors related to lateral spin-valve experiments. In this thesis the investigations focus on the structural, magnetic and electrical properties of the hybrid systems: iron on modulation-doped GaAs (001), iron on MgO on modulation-doped GaAs (001) and iron on inverted, modulation-doped InAs heterostructure.

4.1. Iron on modulation-doped GaAs (001)

The following comprises the investigations of iron on modulation-doped GaAs (001) structures. The section contains results about strain relaxation during the deposition of iron, in-plane magnetic properties as the crystal directions of magnetic axes and the magnetic anisotropies of the iron films and electrical properties of the iron/highly-doped GaAs interface. The sample design and deposition sequence of this structure are described in section 3.1.4.

4.1.1. Strain relaxation during the deposition of iron

This section presents the strain evolution during the deposition of iron films on modulation-doped GaAs (001). In-situ *RHEED* was applied to access the temporal course of surface morphology as well as in-plane lattice constant. Ex-situ *HRXRD* measurements were performed to investigate the out-of-plane lattice constant and texture of the deposited iron film.
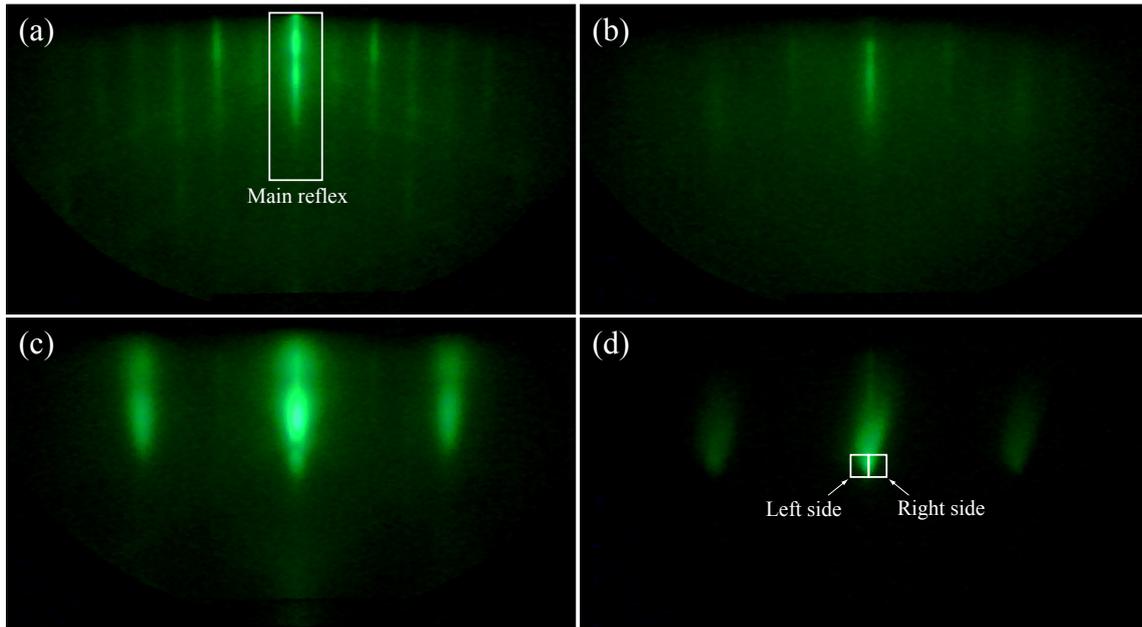
Figure 4.1.: *RHEED* pattern of (a) the GaAs substrate and of iron films grown on this substrate with layer thicknesses of (b) 0.4 nm, (c) 4.8 nm and (d) 80 nm, respectively.

Figure 4.1 shows *RHEED* patterns at various deposition stages. The electron beam was aligned in the [110] crystal direction. Before deposition of iron the semiconductor structures had an arsenic terminated surface with (2×4) surface reconstruction, as it is shown in Figure 4.1(a). During iron deposition streaky patterns arise as shown in Figures 4.1(b) to 4.1(d). The shape of the reflexes changes its form with increasing iron film thickness.

The temporal course of the *RHEED* patterns reveals that the intensity of the reflexes changes during deposition. This was examined by integrating the intensity of the main reflex (area delineated by a white box in Figure 4.1(a)) which mainly reflects the surface roughness. The blue curve in Figure 4.2 presents the integrated intensity data as a function of the iron layer thickness. The intensity drops immediately after the start of deposition. This decrease is most likely due to the formation of islands on the GaAs surface[115]. The subsequent increase of the intensity indicates coalescence and smoothing of the iron surface. Accordingly, with increasing film thickness the intensity decreases indicating roughening of the surface. Ex-situ atomic force microscopy measurements confirmed such surface roughening with increasing layer thickness.

Not only the intensities but also the shape of the reflexes changes with increasing iron film thickness. This was investigated by integrating the left and right side intensities of

the main reflex which are marked by squares in Figure 4.1(d). In Figure 4.2 the difference between the right and left side intensities is displayed by the red curve. The data reveal an asymmetric evolution of the reflex for thicknesses larger than 30 nm. This indicates that restructuring of the surface morphology took place by the formation of in-plane misaligned islands. A similar evolution of the main reflex's shape was observed for iron films on inverted, modulation-doped InAs heterostructures as described in section 4.4.
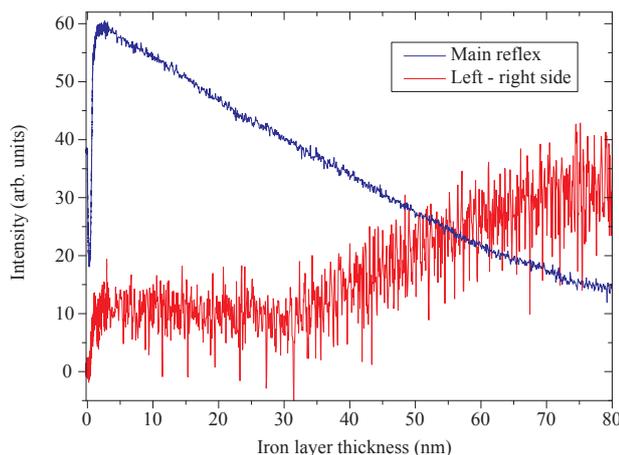
Figure 4.2.: Course of the integrated intensity of the main reflex (blue line) and the reflex asymmetry as a function of the iron layer thickness. The red line shows the difference between the intensities on the left- and right-side shoulder of the main reflex.

The strain evolution during the deposition of iron was investigated by accessing the in-plane lattice constant via *RHEED*. The lattice constant was extracted from the lateral distance between the *RHEED* reflexes of the iron film in Figure 4.1 and determined with respect to the GaAs lattice constant. This method is described in section 3.2.2. Figure 4.3 shows a plot of the such determined in-plane lattice constant of iron as a function of the iron layer thickness. The dashed lines mark half the lattice constant of GaAs (0.28267 nm) and the bulk value of iron (0.28664 nm). Clearly, at small layer thickness the data reflect the lattice constant of the GaAs substrate showing iron films with compressive strain. Accordingly, the in-plane lattice constant increases with increasing film thickness. The data form a distinct peak at the layer thickness of 0.6 nm and a plateau at intermediate film thicknesses. Above 50 nm the lattice constants merge to the bulk value of iron.

The *RHEED* patterns in Figure 4.1 indicate an epitaxial relationship between the iron and the underlying GaAs. As depicted in these images the lateral distance between two neighboring stripes in the pattern of the iron film is twice the distance as between the
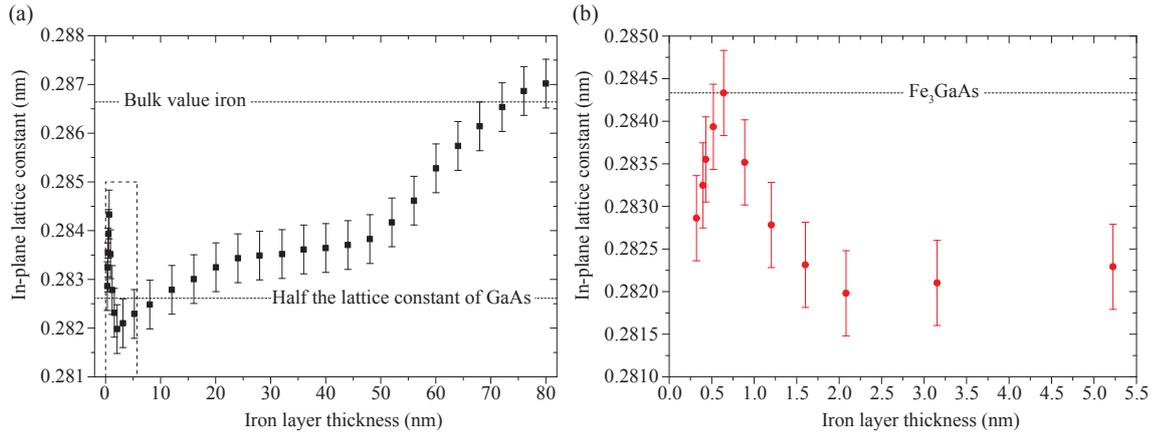
Figure 4.3.: (a) In-plane lattice constant of the iron films versus the layer thickness. (b) Closeup of the range marked with a dashed line in the left graph.

stripes generated by the GaAs. This is due to the fact that the lattice constant of iron (0.28664 nm) is roughly half the one of GaAs (0.56533 nm). With regard to an in-plane epitaxial relationship, the most likely alignment between iron (001) and GaAs (001) would be two iron unit cells for every GaAs unit cell to reduce the misfit strain to $\sim 1.4\,\%$. In contrast, 25 and 170 monolayers-thick iron films on (4×6) reconstructed GaAs (001) surfaces have been investigated with *RHEED* and reported to reveal tensile strain at similar substrate temperatures during iron deposition[17,116]. The results indicate that different surface reconstruction might lead to iron films with either tensile or compressive strain.

The evolution of the in-plane lattice constant of iron in Figure 4.3 reflects the relaxation process of the compressive strain. The peak which arises within the first monolayers in Figure 4.3 has the maximum of 0.28433 nm. This lattice constant can be assigned to the formation of Fe_3GaAs[17] which has half the magnetic moment of iron. Such pseudocubic hexagonal magnetic phases are known to grow epitaxially on GaAs (001)[117]. The formation of the Fe_3GaAs compound at the Fe/GaAs interface is limited by the number of gallium and arsenic atoms on the semiconductor surface. Since the surface is arsenic terminated, the gallium atoms restrict the size of the Fe_3GaAs intermixing layer at the interface. Filipe et al. determined two possible lattice constants of the pseudocubic Fe_3GaAs phase of $a = 0.2843$ nm and $a = 0.2886$ nm but observed just the larger one. This might suggest that Fe_3GaAs adapts itself to the GaAs (001) lattice with either of the two lattice constants related to different atomic orderings of the (2×4) and (4×6) surface reconstructions[118]. Previous studies have shown that interdiffusion of arsenic atoms can also lead to the formation of the compound Fe_2As at the interface[119, 120]. In the present study, remaining arsenic atoms which do not participate to the formation of Fe_3GaAs

might form Fe_2As with its equilibrium lattice constant of $0.544\,nm$[121]. The formation of Fe_2As leads to the minimum in the in-plane lattice constant at around $2.1\,nm$ nominal iron layer thickness. After the minimum, the lattice constants depict a plateau at $0.2835\,nm$ for thicknesses between $25\,nm$ and $40\,nm$. The relaxation of the iron lattice up to this lattice constant might be induced by defects originating from the intermixing of iron, arsenic and gallium atoms at the interface. At thicknesses beyond $50\,nm$ the iron lattice relaxes further and reaches its bulk lattice constant at about $80\,nm$. This final relaxation might be caused by the restructuring and the formation of in-plane misaligned islands.

HRXRD was employed to further investigate the hybrid structure. The black curve in Figure 4.4 shows data of the symmetrical scan along the crystal truncation rod of the GaAs [004] reflex. The experimental data were fitted using Pseudo-Voigt functions. The red solid line in Figure 4.4 displays the sum of the fits and the blue lines the fits to background and individual peaks, respectively. The dashed line marks the peak position for bulk unstrained iron. Data reveal two peaks that we associate to (002) iron peaks. They are located at smaller angles than the iron literature value.
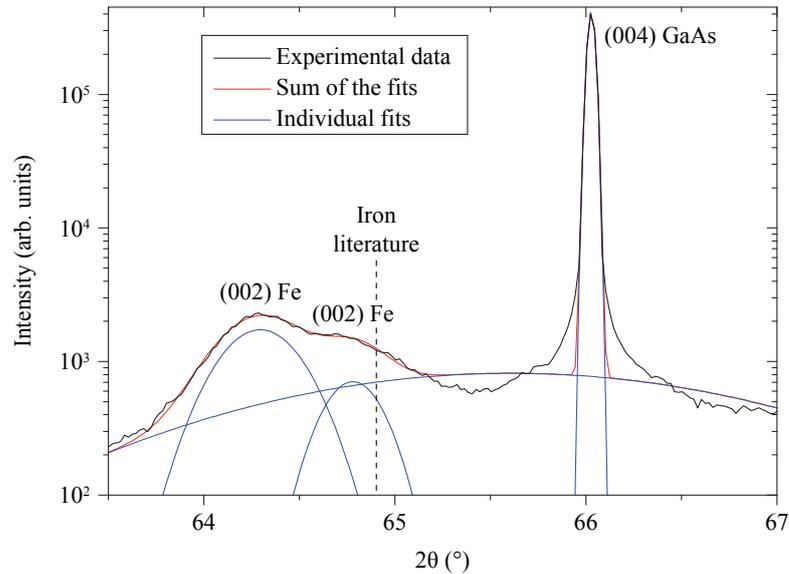
Figure 4.4.: Symmetrical $\omega - 2\theta$-scans of the $80\,nm$-thick iron film on modulation-doped GaAs (001) structure. The graph shows each calculated contribution of the different layers with the iron peaks at $64.3109\,°$ and $64.7939\,°$ as well as the calculated sum of the intensities.

The (002) peak positions of the iron were extracted from the fitted X-ray diffraction data in Figure 4.4 and used to determine the out-of-plane lattice constants of $0.2894\,nm$ and $0.2875\,nm$ with Bragg equation 3.3. The corresponding in-plane lattice constants

of $a = 0.2863$ nm and $a = 0.2869$ nm were calculated by assuming an isotropic in-plane lattice constant and the Poisson's ratio of 0.282[122]. Notice that the relaxed in-plane lattice constant is larger for the *RHEED* than for the *HRXRD* technique. This is due to the deeper penetration depth of the X-ray beam. It averages over all lattice constants of the iron film. In comparison, the average in-plane lattice constant of the *RHEED* data in figure 4.3 result in 0.2839 nm. The difference to the *HRXRD* data might be explained by further relaxation of the iron lattice after deposition.

Finally, the texture of the iron films was studied using pole figures. These were constructed by performing ω-scans at the ω-2θ position of the iron peaks for different in-plane crystal directions. The data revealed that the (002) planes of the iron are aligned parallel to the (001) planes of the GaAs substrate.

4.1.2. In-plane magnetic properties of the iron films

The magnetic properties of iron films on modulation-doped GaAs (001) were studied using the room-temperature *MOKE* method. In the first part of this section, two samples with 32 nm-thick and 8.2 nm-thick iron films were investigated to determine the crystal directions of the film's in-plane magnetic axes. In these measurements, the quadrupole magnet applied an unintentional external magnetic offset field. This field was directed perpendicular to the external magnetic field of the actual *MOKE* measurements. The offset field had an estimated magnitude of about -0.2 mT and thus slightly distorted the detected hysteresis loops. Subsequently, the quadrupole magnet was calibrated so that all subsequent measurements were performed without this offset magnetic field. During *MOKE* measurements the external magnetic field was swept from -90 mT to 90 mT in steps of about 0.2 mT. The second part of this section focuses on the thickness dependence of the in-plane magnetic anisotropies. It was studied by performing several Kerr measurements along an iron thickness gradient. The experimental *MOKE* setup, the calibration procedure of the samples, the methods to analyze the results and used terms as polar plot and magnitude of the magnetization vector are described in section 3.5.

32 nm-thick iron film with the external magnetic field along the [100] **crystal direction**

The data in Figure 4.5 reveal that the [100] crystal direction is a magnetic easy axis of the iron film[123]. The normalized longitudinal Kerr signal in Figure 4.5(a) displays a square hysteresis loop with abrupt switching of the magnetization to its saturation value at coercive fields of -1.5 mT and 1.0 mT. The normalized transversal Kerr signal in Figure 4.5(b) exhibits no features and is almost zero.

Figure 4.5(c) presents the polar plot of the reversal process of the normalized magnetization vector $\vec{M}_N(\psi)$ deduced from the normalized longitudinal and transversal Kerr signals. The vector changes its direction in a straight line along the [100] crystal direction while sweeping the external magnetic field.
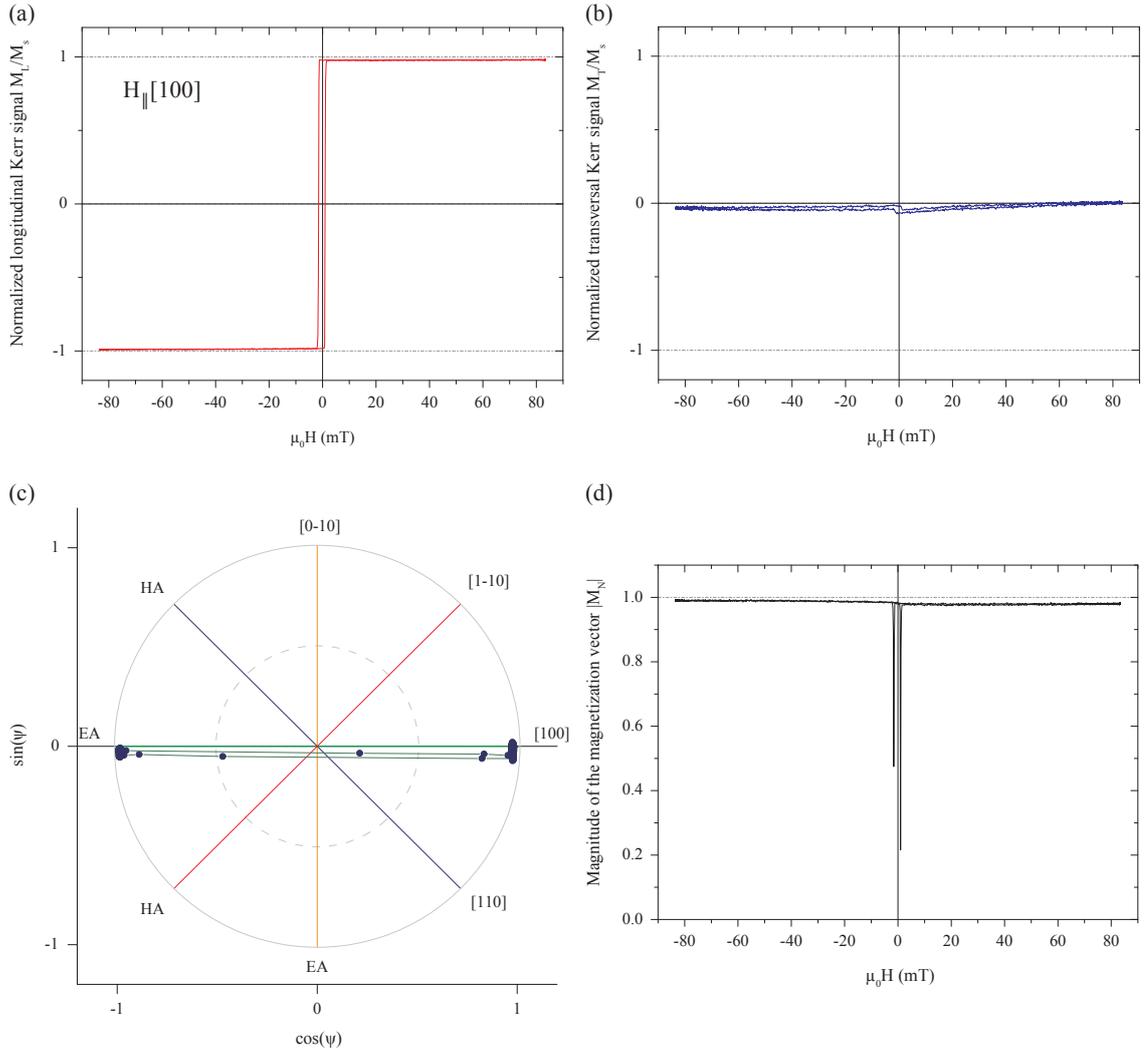
Figure 4.5.: 32 nm-thick iron film: The graphs in (a) and (b) display the normalized longitudinal and transversal Kerr signals versus the external magnetic field applied in the [100] crystal direction. The plot in (c) shows the reversal process of the magnetization vector $\vec{M}_N(\psi)$ as a function of the in-plane rotation angle ψ. The graph in (d) presents the magnitude of the normalized magnetization vector $|\vec{M}_N(\psi)|$ versus the external magnetic field. The polar plot and The data show a slight shift downwards caused by the magnetic offset field.

The magnitude of the magnetization vector $|\vec{M}_N(\psi)|$ is shown in Figure 4.5(d). The magnitude remains constant between magnetic saturations M_S and magnetic remanences M_R revealing monodomain states for positive and negative external magnetic fields. The magnetic remanence is the remaining magnetization if the external magnetic field vanishes. With increasing external magnetic field the magnitude of the magnetization vector drops indicating a multidomain state. This is depicted by the two sharp drops between -1.2 mT and -2.3 mT and 0.6 mT and 1.7 mT, respectively. At the coercive fields H_C domains exist with anti-parallel magnetization in the [100] and [$\bar{1}$00] crystal directions resulting in the vanishing magnetization vector.

32 nm-thick iron film with the external magnetic field along the [110] crystal direction

The data in Figure 4.6 reveal that the [110] crystal direction is a magnetic hard axis of the iron film relative to the magnetic easy axis in the [100] crystal direction[123]. The normalized longitudinal and transversal Kerr signals in Figure 4.6(a) and (b) show both hysteresis loops. By increasing the external magnetic field the magnetization components switch abruptly at coercive fields of -0.5 mT and 2.0 mT but not to its saturation value. Accordingly, the magnetization increases stepwise with increasing external magnetic field till it saturates again.

The polar plot in Figure 4.6(c) displays the reversal process of the normalized magnetization vector $\vec{M}_N(\psi)$ deduced from the normalized longitudinal and transversal Kerr signals. By sweeping the external magnetic field the vector rotates into the magnetic easy axis from its saturation value, changes its direction in a straight line along the [100] crystal direction at its coercive fields and rotates back into the [110] crystal direction. The data show a slight distortion caused by the offset magnetic field.

The magnitude of the magnetization vector $|\vec{M}_N(\psi)|$ is shown in Figure 4.6(d). In addition to the drops, the magnitude increases with increasing positive magnetic field. This behavior is probably caused by the magnetic offset field. The magnitude of the magnetization vector remains constant during rotation between magnetic saturations M_S and magnetic remanences M_R. This is described as coherent rotation of monodomain states. With increasing external magnetic field the magnitude drops indicating a multidomain state. This is depicted by the two sharp drops between -0.3 mT and -1.1 mT and 1.7 mT and 2.8 mT, respectively. At the coercive fields H_C a multidomain structure arises in which domains with anti-parallel magnetization result in a vanishing magnetization vector.
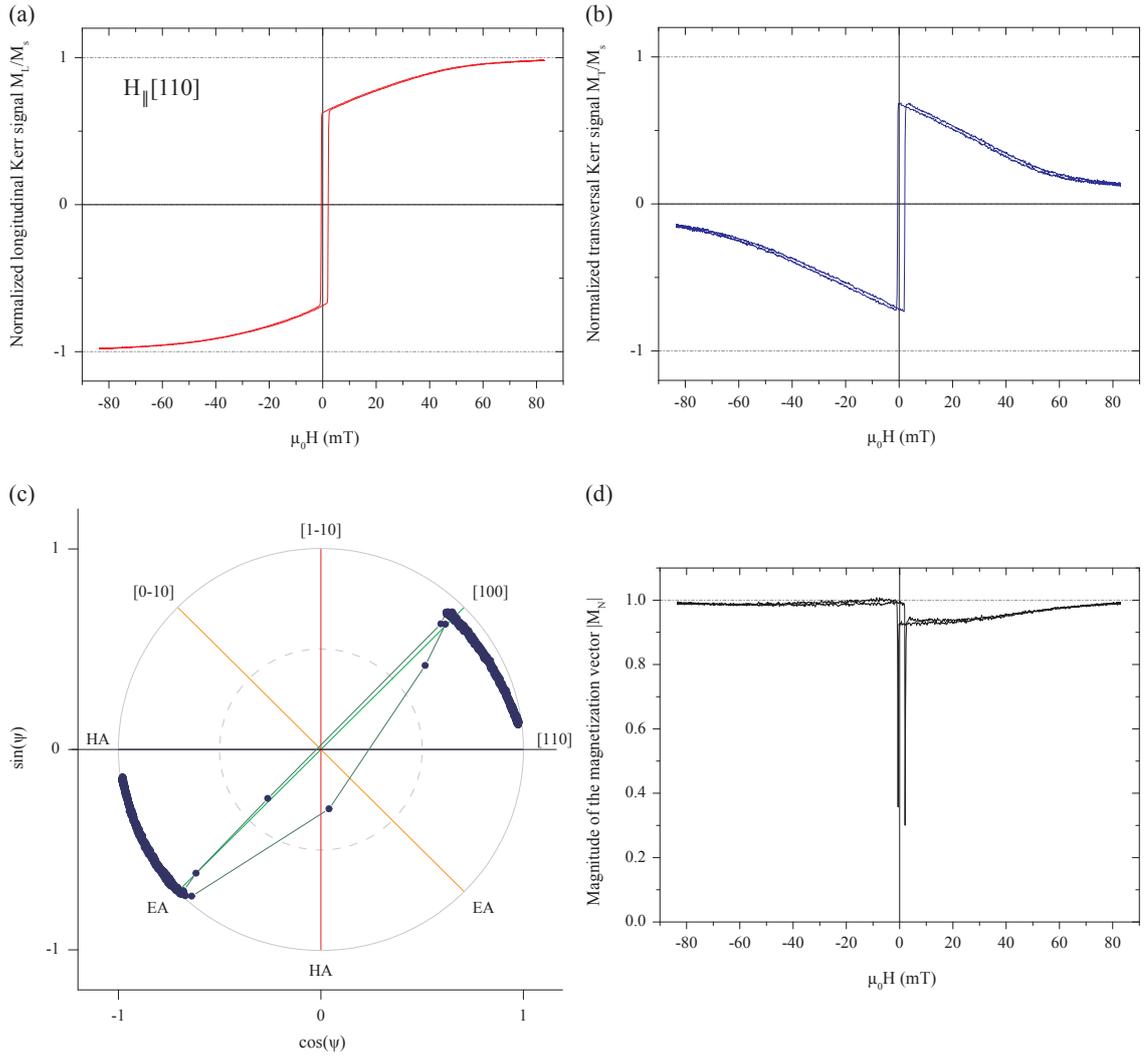
Figure 4.6.: 32 nm-thick iron film: The graphs in (a) and (b) display the normalized longitudinal and transversal Kerr signals versus the external magnetic field applied in the [110] crystal direction. The plot in (c) shows the reversal process of the magnetization vector $\vec{M}_N(\psi)$ as a function of the in-plane rotation angle ψ. The graph in (d) presents the magnitude of the normalized magnetization vector $|\vec{M}_N(\psi)|$ versus the external magnetic field.

The 32 nm-thick iron film reveals two equivalent magnetic hard axes in the [1$\bar{1}$0] and [$\bar{1}\bar{1}$0] crystal directions and two equivalent magnetic easy axes in the [010] and [100] crystal directions. These magnetic axes correspond to an in-plane cubic magnetic anisotropy K_4[115, 123] as shown in Figure 4.7. The magnitude data in Figure 4.5(d) and 4.6(d) show an asymmetry between negative and positive external magnetic fields. This might be caused by the magnetic offset field or due to a slight misalignment of the magnetic axis with the direction of the external magnetic field.
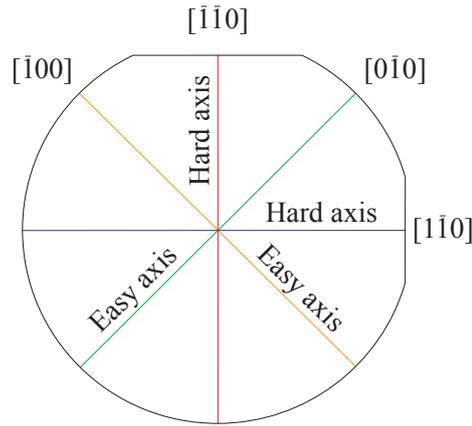
Figure 4.7.: 32 nm-thick iron film: Schematic of the cubic magnetic anisotropy K_4 of the 32 nm-thick iron film with the crystal orientations of its magnetic axes.

8.2 nm-thick iron film with the external magnetic field along the $[\bar{1}\bar{1}0]$ crystal direction

The data in figure 4.8 reveal that the $[\bar{1}\bar{1}0]$ crystal direction is a magnetic easy axis of the iron film[123]. The normalized longitudinal Kerr signal in Figure 4.8(a) displays a square hysteresis loop with abrupt switching of the magnetization to its saturation value at coercive fields of -1.3 mT and 1.9 mT. The normalized transversal Kerr signal in Figure 4.8(b) shows features at small external magnetic fields. This might be caused by a slight misalignment of the magnetic axis with the direction of the external magnetic field or due to the external offset field.

The polar plot in Figure 4.8(c) presents the reversal process of the normalized magnetization vector $\vec{M}_N(\psi)$ deduced from the normalized longitudinal and transversal Kerr signals. The data show a shift to negative magnetization values. This might be caused by a slight misalignment of the magnetic axis with the direction of the external magnetic field but most likely due to the magnetic offset field. By sweeping the magnetic field the vector changes its direction in a straight line parallel to the $[\bar{1}\bar{1}0]$ crystal direction.

The magnitude of the magnetization vector $|\vec{M}_N(\psi)|$ is shown in Figure 4.8(d). The magnitude remains almost constant between magnetic saturations M_S and magnetic remanences M_R revealing monodomain states. The asymmetry between positive and negative external magnetic fields is probably caused by a slight misalignment of the magnetic axis with the direction of the external magnetic field or due to the external offset field. The magnetic remanence is the remaining magnetization if the external magnetic field vanishes. With increasing external magnetic field the magnitude of the magnetization

vector drops indicating a multidomain state. This is depicted by the two sharp drops between $-1.1\,\text{mT}$ and $-1.7\,\text{mT}$ and $1.6\,\text{mT}$ and $2.4\,\text{mT}$, respectively. At the coercive fields H_C domains exist with anti-parallel magnetization in the $[\bar{1}\bar{1}0]$ and $[110]$ crystal directions resulting in a vanishing magnetization vector.
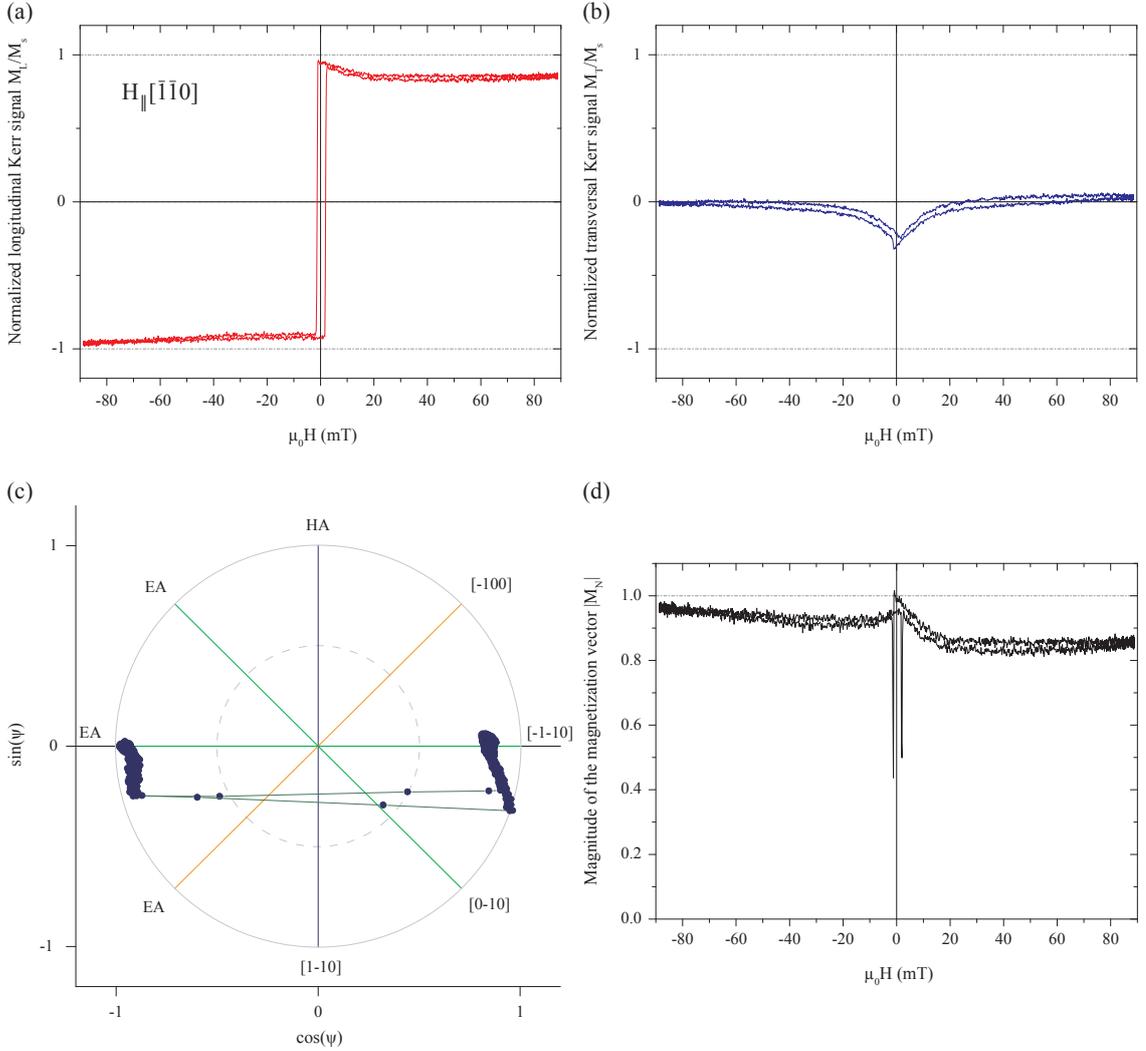
Figure 4.8.: 8.2 nm-thick iron film: The graphs in (a) and (b) display the normalized longitudinal and transversal Kerr signals versus the external magnetic field applied in the $[\bar{1}\bar{1}0]$ crystal direction. The plot in (c) shows the reversal process of the magnetization vector $\vec{M}_N(\psi)$ as a function of the in-plane rotation angle ψ. The graph in (d) presents the magnitude of the normalized magnetization vector $|\vec{M}_N(\psi)|$ versus the external magnetic field.

In contrast to the 32 nm-thick iron film the 8.2 nm-thick iron film reveals a magnetic hard axis in the $[1\bar{1}0]$ and a magnetic easy axis in the $[\bar{1}\bar{1}0]$ crystal direction. These magnetic axes are due to the in-plane uniaxial magnetic anisotropy K_U[115,123] as shown in Figure

4.9. In addition to the uniaxial anisotropy, the investigation of the 8.2 nm-thick iron film revealed two equivalent magnetic easy axes along the $[\bar{1}00]$ and $[0\bar{1}0]$ crystal directions. These magnetic easy axes are less distinct than the ones for the 32 nm-thick iron film indicating a weakly overlapped cubic anisotropy. The *MOKE* results of the 8.2 nm-thick iron film's hard and easy magnetic axes which are aligned parallel to the $[1\bar{1}0]$ and $[\bar{1}00]$ crystal directions are attached in the appendix section A.2.
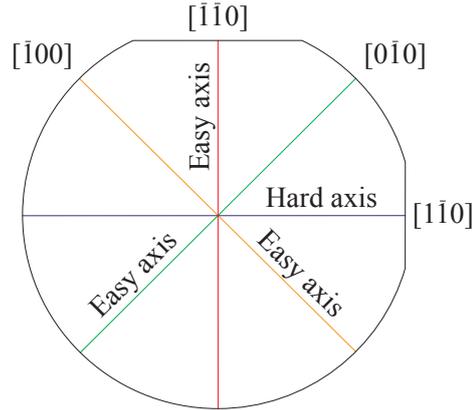
Figure 4.9.: 8.2 nm-thick iron film: Schematic of the cubic magnetic anisotropy K_4 of the 8.2 nm-thick iron film with the crystal orientations of its magnetic axes.

Thickness dependence of the in-plane magnetic anisotropies

The results from the 32 nm and 8.2 nm-thick iron films indicate that the in-plane magnetic anisotropies depend on the iron film's thickness. *MOKE* measurements for different iron film thicknesses were performed to investigate this dependency. The anisotropy constants K_U and K_4 for the uniaxial and cubic magnetic anisotropy were deduced from the shape of the hysteresis loops along the magnetic hard axis in the $[1\bar{1}0]$ crystal direction. The analysis method used to extract the anisotropy constants is described in section 3.5.2.

Figure 4.10 displays the dependence of the in-plane uniaxial anisotropy K_U, the cubic anisotropy K_4 and the coercive field $\mu_0 H_C$ on the iron layer thickness. The iron thickness gradient was fabricated with an especially designed tantalum mask in the metal *MBE* chamber. Thereby, changes in the anisotropies with the iron layer thickness could be studied systematically from one sample. The thickness gradient was confirmed by four-probe measurements calibrated with *RHEED* oscillations as described in section 3.3. Certain facts may limit the precision with which the layer thickness was determined along the thickness gradient. This is described at the end of section 3.5.2.
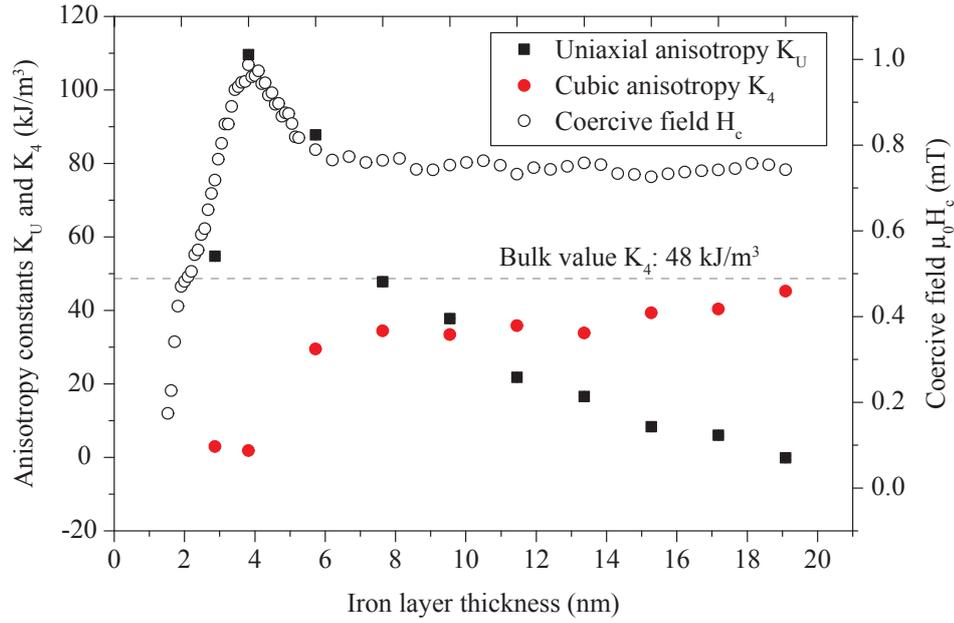
Figure 4.10.: The graph shows the in-plane magnetic anisotropy constants K_U and K_4 deduced from magnetic hard axis hysteresis loops in the $[1\bar{1}0]$ crystal direction as a function of the iron film thickness. The right side y-axis displays the coercive field $\mu_0 H_c$ along the iron thickness gradient.

Initially, at low iron coverages of about 0.5 nm, where the *RHEED* intensity in Figure 4.2 shows the drop in the beginning of deposition, impinging iron atoms formed small isolated islands. At this growth state the exchange coupling related to ferromagnetism was limited to the number of iron atoms within these islands. Thus, the small islands probably featured superparamagnetism or 2D-paramagnetism with Kerr effect signals smaller than the resolution of the used *MOKE* setup. The first Kerr signals were measured for thicknesses ≥ 1.3 nm. This indicates a stronger exchange interaction within the islands or between different islands leading to internal ferromagnetic ordering[124]. Also, intermixing and the formation of compounds at the interface[17,125] can reduce the magnetic moments and thus the coercivity. After the islands coalesce, the coercive field increases in Figure 4.10 reflecting the evolution of the Curie temperature toward its bulk value. This dependence is known as an effect of reduced dimensionality of the iron film[126]. The coercive field shows a maximum of $H_C = 1.1$ mT at 2.6 nm. Subsequently, H_C decreases for thicker iron films and converges at 0.75 mT. The decrease might be ascribed to surface roughening of the film[126,127].

At iron films thicker than 8 nm the cubic anisotropy dominates and converges to the bulk value of iron $K_4 = 48$ kJ/m^3[13]. By decreasing the iron coverage below 8 nm the cubic

anisotropy decreases and the uniaxial one becomes more significant. At smaller coverages below 2.6 nm the latter one decreases again. This is attributed to the evolution of the ferromagnetic signal. Other groups observed similar behavior of the magnetic anisotropies for iron films on GaAs (001) hybrid structures[13, 115].

4.1.3. Electrical properties of the iron/highly-doped GaAs interface

The electrical properties of the iron/highly-doped GaAs interface were investigated using the closed cycle cryostat and circle structures which are described in section 3.6. Current-voltage characteristics were collected in two-terminal geometry. The voltages were applied between two circle shaped iron contacts while measuring the current flowing through two similar interfaces. The applied voltage was swept from $-4\,\mathrm{V}$ to $4\,\mathrm{V}$ in steps of 1 mV. The current-voltage curves were conducted for sample temperatures between 9 K and 290 K varied in steps of 5 K. Further information about the experimental setup and the current-voltage measurements are supplied in section 3.7.

Figure 4.11(a) displays the current-voltage characteristics of the hybrid structure for sample temperatures of 9 K, 100 K, 200 K and 290 K. The inset depicts a sketch of the contacted hybrid structure. With decreasing temperature the shape of the curves deviate from the linear ohmic behavior at 290 K.

Figure 4.11(b) shows the differential resistance dU/dI multiplied by the total contact area $A = \pi \cdot 0.5^2\,\mathrm{mm}^2$ versus the applied voltage at sample temperatures between 9 K and 140 K. The data reveal a peak in resistance arising around zero bias with decreasing temperature. The curves are symmetrical for positive and negative voltages. At low temperatures the $R(V)$ curves show minima at around $\pm 2.5\,\mathrm{V}$ and maxima at around $\pm 3\,\mathrm{V}$.

The data in Figure 4.11(c) display the differential resistance dU/dI multiplied by the total contact area A at zero bias and 2.5 V as a function of the sample temperature between 9 K and 290 K. Both curves show minima at around 142.5 K. In contrast to the differential resistance at zero bias the data with an applied voltage of 2.5 V exhibit a maximum around 20 K. At 9 K the ZBR is about two times larger than at 290 K.

The data in figure 4.11(d) are the derivative dR/dT of the differential resistance. The graph reveals turning points and changes in the slope of the resistance curves of the data in Figure 4.11(c). While the negative slope of the ZBR increases monotonically below $142.5\,K$
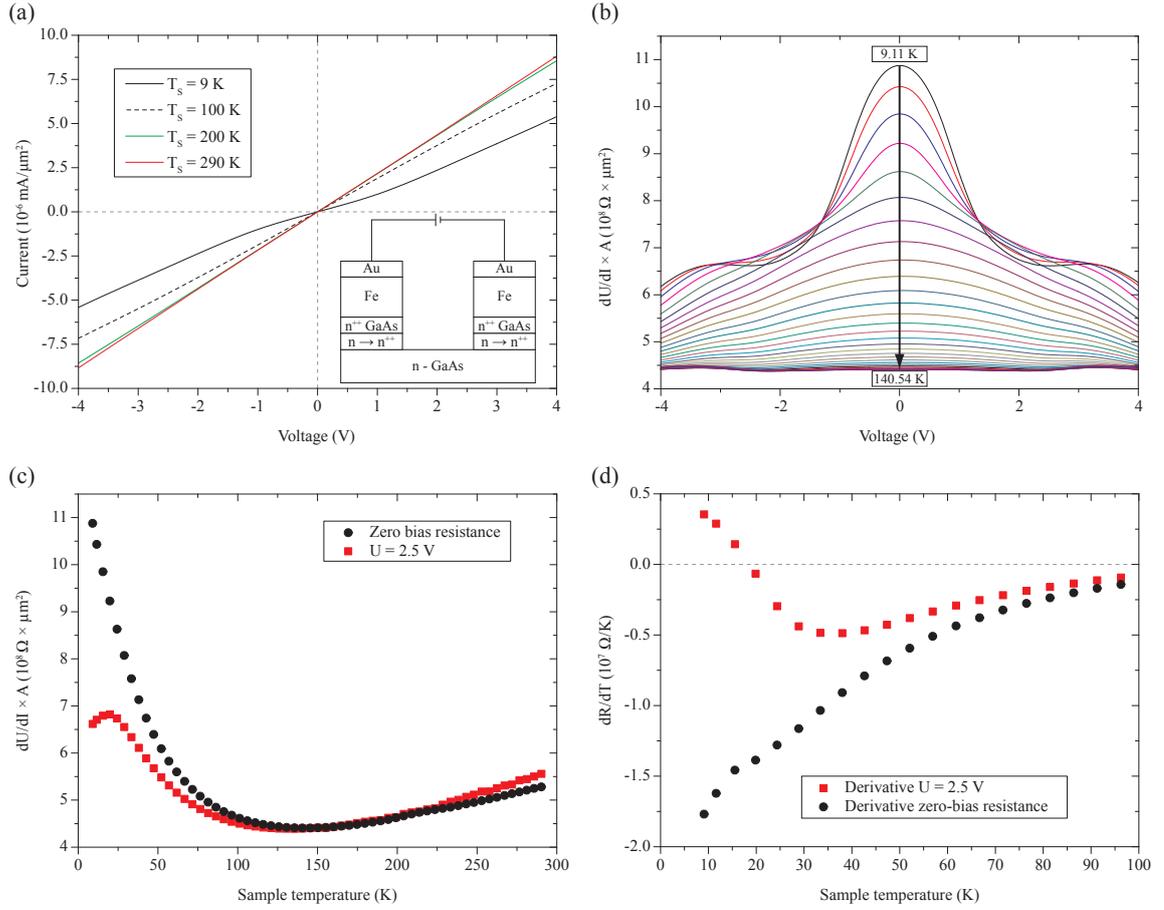
Figure 4.11.: (a) Current-voltage curves for different sample temperatures and a sketch of the contacted hybrid structure, (b) differential resistance multiplied by the total contact area as a function of voltage for various sample temperatures, (c) differential resistance multiplied by the total contact area versus the sample temperature and (d) derivative of the differential resistance dR/dT.

the sign of the slope of the resistance data for the applied voltage turns positive below $38\,\mathrm{K}$.

The deviation of the current-voltage curves from ohmic behavior at lower temperatures in Figure 4.11(a) indicates Schottky barriers at the iron/highly-doped GaAs interface. Previous studies have shown that Schottky barriers form at iron/GaAs interfaces[45, 46]. The $R(V)$ data in Figure 4.11(b) depict the impact of the Schottky barrier by the increasing resistance with decreasing temperature. The resistance curves in Figure 4.11(c) reveal that this impact starts below $142.5\,\mathrm{K}$. The barrier's resistance in Figure 4.11(b) decreases with increasing applied voltage. At low temperatures the $R(V)$ data show a drop at $\pm 2.5\,\mathrm{V}$. This behavior starts to develop below $38\,\mathrm{K}$ as the derivative data dR/dT versus the sample temperature reveal in Figure 4.11(d). The drop is most likely caused by electrical heating of the structure with the power of $5\,\mathrm{mW}$ thus increasing the conductivity

of the sample. Larger voltages than 2.5 V might lead to phonon scattering so that the resistance increases in 4.11(d). The resistance decreases again for voltages larger than ± 3 V. This is due to the thinner barrier at these higher electron energies.

In this experiment, the current flows through two Schottky barriers which are connected in series. By applying either negative or positive voltages one of the barriers will always be in forward and the other one in reverse bias. Therefore, both barriers have an impact on the current-voltage characteristics. The diploma thesis of Tobias Nickel[103] contains electrical investigation of two iron/highly-doped GaAs interfaces connected in series. In his study, fits of the current-voltage curves by applying the thermionic-emission theory led to the Schottky barrier height of $e\,\Phi_B = 12$ meV with the ideality factor of $n = 10$ at temperatures around 100 K. The high ideality factor indicates that other mechanisms than just thermionic emission have an impact on the carrier transport across the interface leading to the not reliable height of the Schottky barrier. Also the weak temperature dependence of the *ZBR* between 142.5 K and 9 K by factor of 2.4 related to the third Rowell criterion indicates that tunneling of electrons through the barrier may become more significant at low temperatures[19]. At the iron/highly-doped GaAs interface tunneling of electrons can also occur at room-temperature as discussed in section 2.1 for an ideal Schottky barrier. This has been observed with Fe/GaAs spin-light-emitting diodes[128] and also in Fe/Al$_x$Ga$_{1-x}$As/GaAs heterostructures with the electroluminescence polarization technique[129]. Intermixing at the interface and the formation of Fe$_3$GaAs interfacial layers as revealed by *RHEED* data in section 4.1.1 influence the transport across the interface[130] and might lower the tunneling probability.

In conclusion, iron on modulation-doped GaAs structures exhibited Schottky barriers at the iron/highly-doped GaAs interface. The tunneling probability of charge carriers through the barrier increased below 142.5 K and was reduced above this temperature. With regard to future spin-injection experiments, the ferromagnetic ternary Fe$_3$GaAs which formed at the iron/highly-doped GaAs interface during deposition might also influence the tunneling process of spins through the potential barrier[47,51]. Thereby, the sample temperature during deposition and also a post-annealing step are critical factors to enhance the injection efficiency of the hybrid structure.

4.2. Iron/MgO/modulation-doped GaAs (001)

This section focuses on the iron/MgO/modulation-doped GaAs (001) hybrid structures. In regard to fabricate spin injection and detection devices it is important to achieve smooth interface morphologies of the embedded MgO film. Therefore, the fabrication conditions such as substrate temperature, deposition rate and post-annealing are crucial factors toward high-quality MgO films. The following presents the results of the optimized fabrication process, the influence of MgO layer thickness and annealing on the electrical properties of the structure and the in-plane magnetic properties of the iron films.
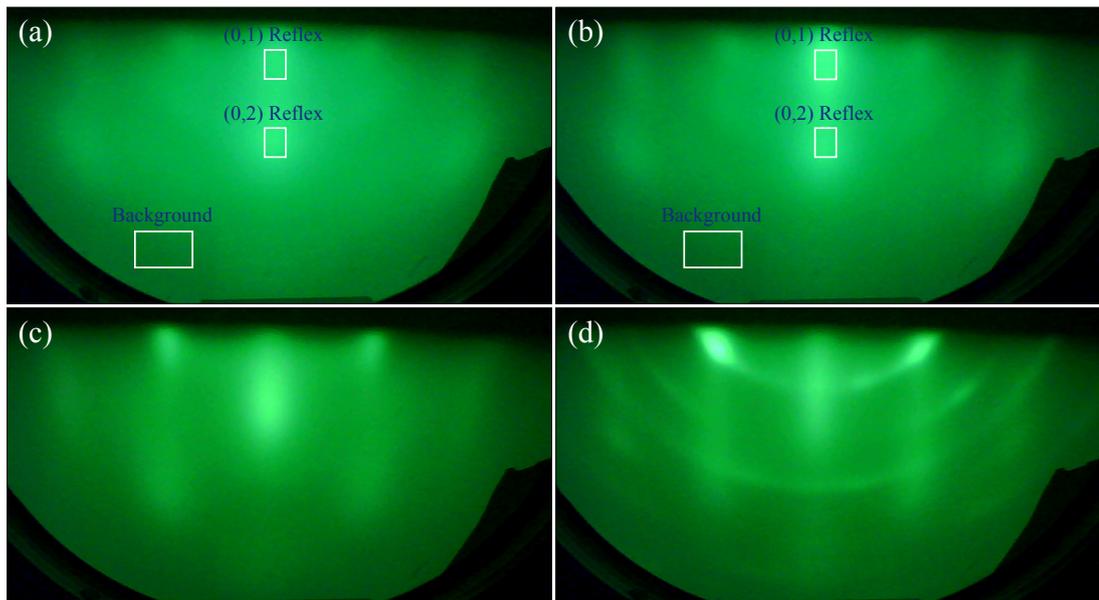
Figure 4.12.: *RHEED* pattern (a) of the as-deposited MgO film, (b) of the post-annealed MgO film, (c) after the deposition of $3.1\,\mathrm{nm}$ and (d) of $15\,\mathrm{nm}$-thick iron films. The white squares display the areas of the $(0, 1)$ reflex, the $(0, 2)$ reflex and the background intensity. These intensities were integrated over time to analyze the temporal course of the post-annealing process of the MgO film.

4.2.1. Epitaxial growth and structural properties

The modulation-doped GaAs (001) structures were fabricated using the C21 Riber *MBE* chamber. After semiconductor deposition streaky *RHEED* patterns ensured the GaAs (2×4) reconstruction and arsenic terminated surface. The MgO films were deposited using the MgO *MBE* chamber with an additional oxygen background pressure. Subsequently, the samples were post-annealed in the metal *MBE* chamber at $400\,°$ for three minutes. Finally, iron films and thin capping layers of gold were deposited on top of the MgO film. All samples were transferred in-vacuo between the

deposition steps. The fabrication process with its settings is described in section 3.1.4. During *RHEED* measurements the electron beam was aligned in the [110] crystal direction.

The *RHEED* images in Figure 4.12 present the optimized fabrication process of the hybrid structure at various stages of the deposition process. The *RHEED* patterns of the MgO film before and after the annealing step in Figure 4.12(a) and 4.12(b) depict that the intensities of the MgO reflexes and the background changed during annealing. This was examined by integrating the intensities (areas delineated by a white solid line). The graph in Figure 4.13(a) displays the integrated $(0,1)$ and $(0,2)$ reflex intensities with the background intensity subtracted. The temporal course of the $(0,1)$ and $(0,2)$ reflex intensities indicate smoothing of the MgO surface[131] and realignment of MgO crystals toward the (001) crystal direction. The background intensity in Figure 4.13(b) decreases with increasing annealing time due to the change in surface roughness. Thereby, prior at the MgO surface diffusive scattered electrons now contribute to diffraction at the (001) planes of the MgO crystals.
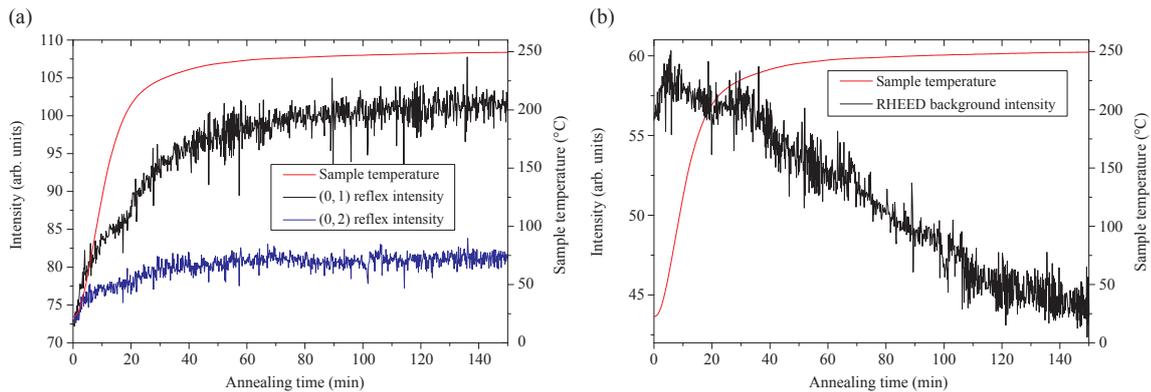
Figure 4.13.: The graphs present (a) the integrated $(0,1)$ and $(0,2)$ reflex intensities with the background intensity subtracted and (b) the integrated background intensity during annealing.

The *RHEED* pattern of the 5 nm-thick MgO film in Figure 4.12(b) indicates an epitaxial relation between the MgO film ($a_{\text{MgO, unstrained}} = 0.4216\,\text{nm}$[132]) and the GaAs substrate ($a_{\text{GaAs}} = 0.5653\,\text{nm}$) despite the large lattice mismatch of $\sim 25.4\,\%$. Similar but more distinct pattern were also observed by another group[133]. With regard to an in-plane epitaxial relationship, the most likely alignment between (001) MgO and (001) GaAs would be four MgO unit cells for every three GaAs unit cells[134, 135]. This alignment leads to the tensile strain of about $0.41\,\%$ with the MgO lattice constant of $a_{\text{MgO, strained}} = 0.4222\,\text{nm}$. Furthermore, the elongated spots in the *RHEED* pattern in Figure 4.12(b) suggest a polycrystalline structure of the MgO film.

The *RHEED* pattern of the 3.2 nm-thick iron film in Figure 4.12(c) reveals an epitaxial relationship to the lattice of the underlying MgO film. The most likely in-plane epitaxial relationship would be rotating the unit cell of iron against the one of MgO by 45°[133, 136]. This alignment leads to the tensile strain of about 3.67 % with the iron lattice constant of $a_{\text{Fe, strained}} = 0.2876$ nm. Certainly, if three iron unit cells are placed for every two MgO unit cells the lattice mismatch of ~ 2 % would be smaller. But this arrangement leads to compressive strain. It has been observed that iron growth in the Frank-van der Merwe mode up to a thickness of $2 - 3$ nm[137]. Accordingly, with increasing film thickness the misfit strain of about 3.67 % relaxes by the formation of islands and screw dislocations[137]. Figure 4.12(d) displays the *RHEED* pattern after the deposition of 15 nm iron. Reflexes arranged on Debye-Scherrer rings can be attributed to the formation of polycrystalline fractions caused by the relaxation of the misfit strain. In addition, streaks contribute to the *RHEED* pattern caused by the initially built-up misfit strain. This tensile strain component persists for 50 nm-thick iron films and also even thicker films[137, 138].

4.2.2. In-plane magnetic properties of the iron films

The in-plane magnetic properties of iron films on MgO/modulation-doped GaAs (001) structures were studied using the room-temperature *MOKE* method. A hybrid structure with a 20 nm-thick iron and 6 nm-thick MgO film was investigated to determine the crystal directions of the film's in-plane magnetic axes. *MOKE* measurements were also performed along an iron thickness gradient. The gradient was fabricated with an especially designed tantalum mask in the metal *MBE* chamber so that changes in the magnetic axes could be studied systematically on one sample with the exact same growth conditions. The thickness gradient was confirmed by four-probe measurements calibrated by *RHEED* oscillations as described in section 3.3. In these experiments, the external magnetic field was swept from -80 mT to 80 mT in steps of about 0.2 mT. The experimental *MOKE* setup, the calibration procedure of the samples, methods to analyze the results and the used terms as polar plot and magnitude of the magnetization vector are described in section 3.5.

External magnetic field along the $[1\bar{1}0]$ crystal direction

The data in figure 4.14 reveal that the $[1\bar{1}0]$ crystal direction is the magnetic easy axis of the iron film[133]. The normalized longitudinal Kerr signal in figure 4.14(a) shows a square hysteresis loop with abrupt switching of the magnetization to its saturation value at coercive fields of -1.1 mT and 2.6 mT. The normalized transversal Kerr signal in Figure 4.14(b) displays a small hysteresis loop as well with a peak at 2.4 mT. The shift of both

Kerr signals to positive external magnetic fields is most likely due to a not perfectly aligned applied magnetic field with the crystal axis.
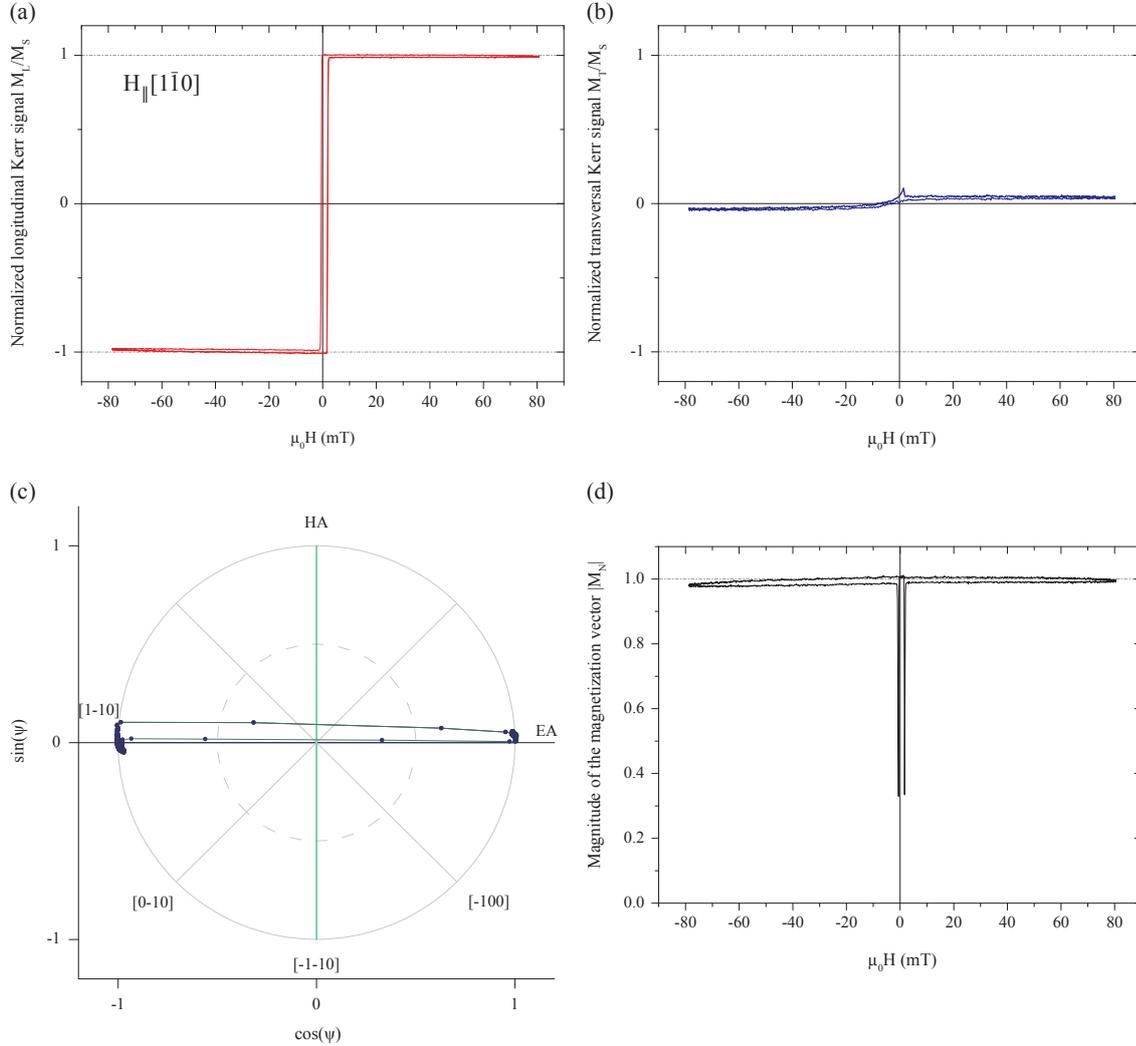
Figure 4.14.: 20 nm-thick iron film: The graphs in (a) and (b) display the normalized longitudinal and transversal Kerr signals versus the external magnetic field applied in the $[1\bar{1}0]$ crystal direction. The plot in (c) shows the reversal process of the magnetization vector $\vec{M}_N(\psi)$ as a function of the in-plane rotation angle ψ. The graph in (d) presents the magnitude of the normalized magnetization vector $|\vec{M}_N(\psi)|$ versus the external magnetic field.

The polar plot Figure 4.14(c) presents the reversal process of the normalized magnetization vector $\vec{M}_N(\psi)$ deduced from the normalized longitudinal and transversal Kerr signals. By sweeping the external magnetic field the vector changes its direction along the $[1\bar{1}0]$ crystal direction.

The magnitude of the magnetization vector $|\vec{M}_N(\psi)|$ in Figure 4.14(d) is constant between magnetic saturation M_S and magnetic remanence M_R revealing monodomain states. The magnetic remanence is the remaining magnetization if the external magnetic field vanishes. By sweeping the external magnetic field the magnitude decreases indicating a multidomain state as depicted by the two sharp drops between $-0.2\,\text{mT}$ and $-1.1\,\text{mT}$ and $1.6\,\text{mT}$ and $2.2\,\text{mT}$, respectively. At the coercive fields H_C domains exist with anti-parallel magnetization in the $[1\bar{1}0]$ and $[\bar{1}10]$ crystal directions resulting in a vanishing magnetization vector.
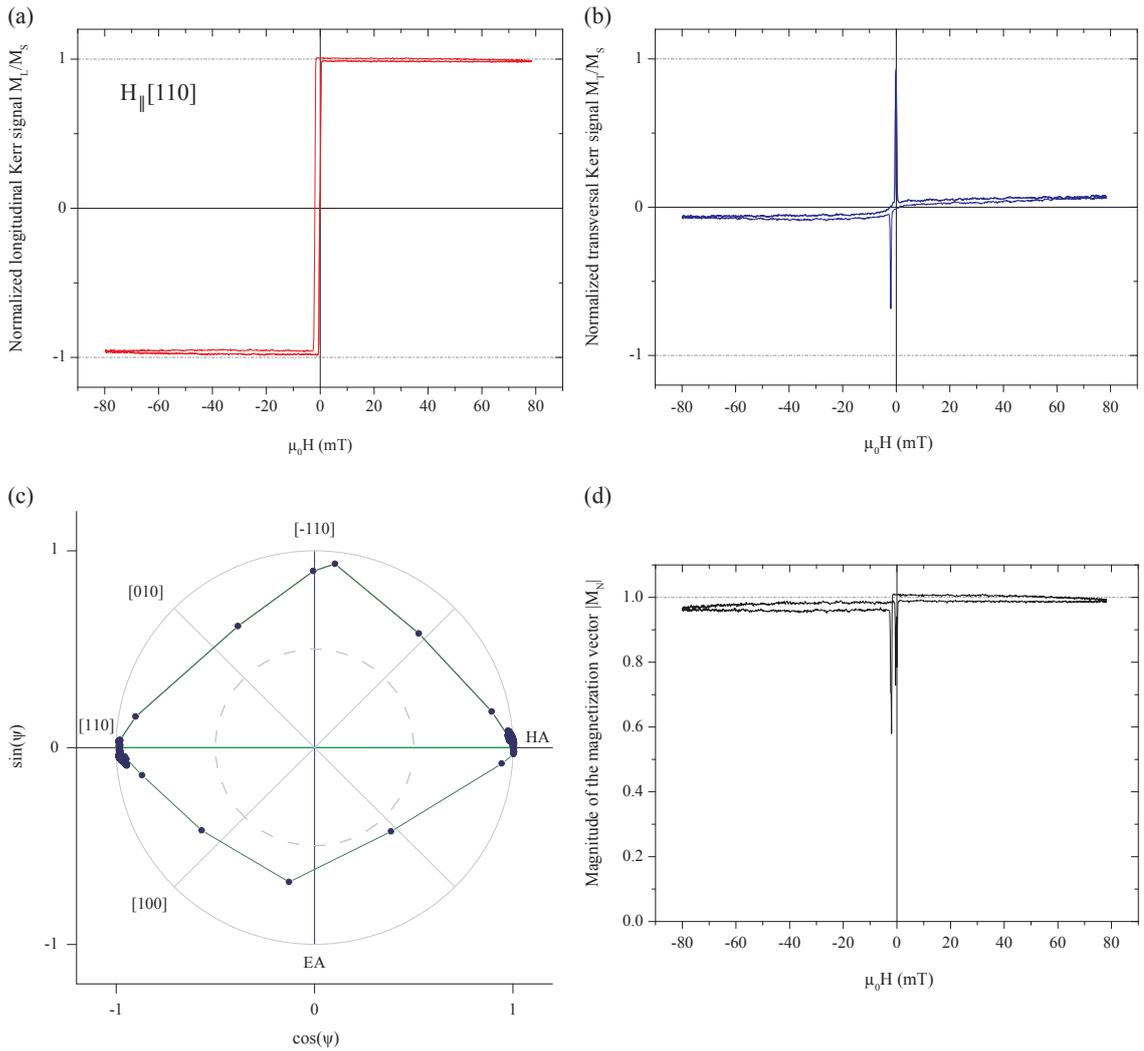
Figure 4.15.: 20 nm-thick iron film: The graphs in (a) and (b) display the normalized longitudinal and transversal Kerr signals versus the external magnetic field applied in the [110] crystal direction. The plot in (c) shows the reversal process of the magnetization vector $\vec{M}_N(\psi)$ as a function of the in-plane rotation angle ψ. The graph in (d) presents the magnitude of the normalized magnetization vector $|\vec{M}_N(\psi)|$ versus the external magnetic field.

External magnetic field along the [110] **crystal direction**

The data in Figure 4.15 reveal that the [110] crystal direction is the magnetic hard axis of the iron film relative to the magnetic easy axis in the [1$\bar{1}$0] crystal direction[133]. The normalized longitudinal Kerr data in Figure 4.15(a) show a square hysteresis loop with abrupt switching of the magnetization to its saturation value at coercive fields of -0.2 mT and -2 mT. The normalized transversal Kerr signal in Figure 4.15(b) depicts two peaks at magnetic fields of -0.1 mT and -2 mT and shows a small hysteresis loop. The shift of both Kerr signals to negative fields is most likely due to a not perfectly aligned applied magnetic field with the crystal axis.

Figure 4.15(c) presents the polar plot of the reversal process of the normalized magnetization vector $\vec{M}_N(\psi)$ deduced from the normalized longitudinal and transversal Kerr signals. By sweeping the magnetic field the vector rotates from the [110] into the opposite [$\bar{1}\bar{1}$0] crystal direction by crossing the magnetic easy axis of the film.

The magnitude of the magnetization vector $|\vec{M}_N(\psi)|$ in Figure 4.15(d) shows two sharp decreases between -1.5 mT and -2.6 mT and -0.7 mT and 0.5 mT, respectively. The magnitude is constant between magnetic saturations M_S and magnetic remanences M_R revealing monodomain states for positive and negative external magnetic fields. By sweeping the field the vector rotates into the opposite [$\bar{1}\bar{1}$0] crystal direction. Thereby, it crosses the magnetic easy axis of the film. The reduced magnitude during the reversal process indicates incoherent rotation of the magnetization vector in a multidomain state.
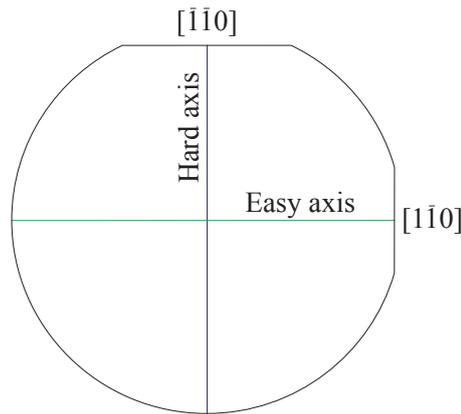
Figure 4.16.: 20 nm-thick iron film: Schematic of the uniaxial magnetic anisotropy K_U with the crystal orientations of its magnetic axes.

The investigated 20 nm-thick iron film on the 6 nm-thick MgO/modulation-doped GaAs structure revealed a magnetic hard axis in the $[\bar{1}\bar{1}0]$ and a magnetic easy axis in the $[1\bar{1}0]$ crystal direction. These magnetic axes are due to the in-plane uniaxial magnetic anisotropy K_U as shown in Figure 4.16. Further magneto-optic Kerr effect measurements along the iron thickness gradient showed no change in the magnetic anisotropy up to a iron film thickness of about 20 nm. This is not coherent with the results from other groups[133, 139]. They observed that the magnetic anisotropy changes to a cubic magnetic anisotropy for MgO film thicker than 1.2 monolayers and even thinner iron films than 20 nm. The difference might be due to a stronger coupling of the iron film to the underlying MgO/GaAs structure in the present study.

4.2.3. Electrical properties of the MgO films

The electrical properties of the iron/MgO/modulation-doped GaAs (001) structures with MgO barriers thicknesses of 2 nm, 4 nm and 6 nm were investigated using the closed cycle cryostat and circle structures which are described in section 3.6. Current-voltage characteristics were collected in two-terminal geometry. The voltages were applied between two circle shaped iron contacts while measuring the current flowing through two similar interfaces. The applied voltage was swept from -2.5 V to 2.5 V in steps of 1 mV. The current-voltage curves were recorded for sample temperatures between 10 K and 290 K varied in steps of 5 K. Further information about the experimental setup and the current-voltage measurements are supplied in section 3.7.

Sometimes it is necessary to anneal the hybrid structures in order to achieve ohmic contacts[131]. The influence of annealing on the electrical properties of MgO barriers was investigated by annealing the structures at the temperature of 400 °C for 3 min. Subsequently, current-voltage measurements were performed for applied voltages swept from -2.5 V to 2.5 V in steps of 1 mV and sample temperatures varied between 10 K and 290 K in steps of 5 K.

Figure 4.17 presents the current-voltage curves of the hybrid structures at the substrate temperature of $T_S = 10$ K 4.17(a) before and 4.17(b) after the annealing process. The inset in 4.17(a) depicts a sketch of the contacted structure. The data in Figure 4.17(a) reveal the expected dependence on the MgO barrier thickness. The thinner the barrier the larger the current density. The effect of annealing on the electrical properties of the hybrid structures was quantified by averaging the current densities at ± 2.5 V for each MgO thickness and determining the ratio between the current densities before and after
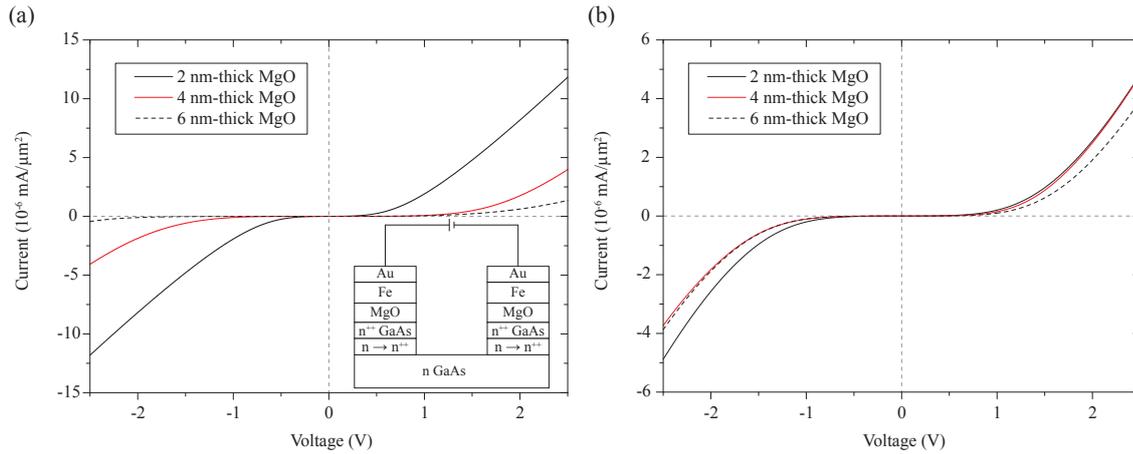
Figure 4.17.: Current-voltages curves for MgO layer thicknesses of 2 nm, 4 nm and 6 nm conducted at the substrate temperature of $T_S = 10$ K (a) before and (b) after annealing the samples at $400\,°\mathrm{C}$ for 3 min. The sketch in (a) shows the contacted hybrid structure.

the annealing. The calculation resulted in the 1.06 and 5.83 times higher and 2.44 times lower current densities for the 4 nm, 6 nm and 2 nm-thick MgO barrier after the annealing, respectively.

The current-voltage characteristics were further analyzed by deriving the data and extracting the zero bias resistance (ZBR) for temperatures between 10 K and 290 K. The graphs in Figure 4.18(a) and 4.18(c) display the ZBR and normalized ZBR as functions of the sample temperature before annealing the structures. Thereby, the resistance was multiplied by the total contact area $A = \pi \cdot 0.5^2\,\mathrm{mm}^2$. Clearly, the resistance increases with increasing MgO film thickness. All three curves show similar exponential temperature dependence above ~ 150 K. At lower temperatures the ZBR curve of the 2 nm-thick MgO film differs from this behavior. The data reveal a smaller steepness of the slope. In contrast, the 4 nm-thick and 6 nm-thick MgO films reveal a stronger temperature dependence as compared to the region above ~ 150 K. In case of the 6 nm-thick MgO film, no reliable ZBR data could be extracted from the $dR(V)$ curves for sample temperatures below ~ 100 K due to the high resistance of the MgO barrier.

The Figures 4.18(b) and 4.18(d) present the ZBR and normalized ZBR as functions of the sample temperature after the annealing process. The data was multiplied by the total contact area $A = \pi \cdot 0.5^2\,\mathrm{mm}^2$. Obviously, the annealing impacted the temperature dependence of the ZBR curves. Above ~ 150 K the curve of the 4 nm-thick MgO film kept almost unmodified, the one of the 6 nm-thick film shifted to lower resistances and of the
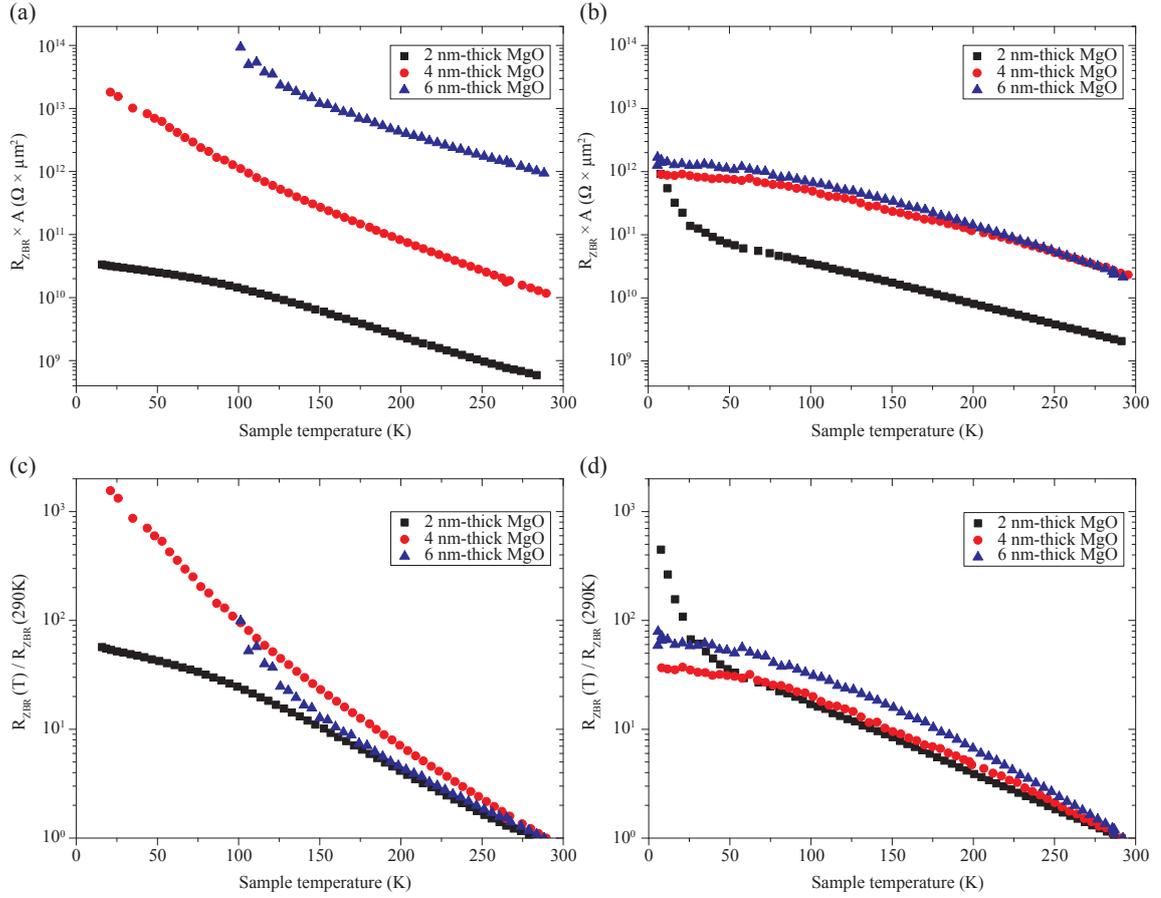
Figure 4.18.: Temperature dependence of the (a) *ZBR* and (c) normalized *ZBR* before and the (b) *ZBR* and (d) normalized *ZBR* after the annealing process for different MgO barrier thicknesses, respectively.

2 nm-thick film to higher resistances. At temperatures below $\sim 150\,\mathrm{K}$ the *ZBR* curves of the 4 nm-thick and of the 6 nm-thick film reveal a smaller slope than before the annealing. Notice that the *ZBR* curves of the 4 nm and 6 nm-thick MgO films have similar resistances and courses over the whole temperature range.

It has been observed that annealing of MgO/GaAs structures leads to reactions at the interface[71]. Xu et al. suggested the interdiffusion of excessive magnesium and oxygen atoms which are stored in the polycrystalline MgO layer. The authors confirmed the formation of GaO_x whose bonding is stronger than the one of GaAs and suggested the formation of Mg_xAs_y. The reactions at the interface and formation of these compounds can effect the form of the potential barrier and might lower its height[140].

In contrast to the 4 nm-thick and 6 nm-thick MgO films, the data of 2 nm-thick MgO film in Figures 4.18(b) and 4.18(d) reveals a strong increase in resistance at low temperatures.

This might indicate not only the formation of GaO_x and Mg_xAs_y compounds but also interdiffusion and intermixing of iron atoms at the interface[41]. Thereby, the annealing and thus realignment of the polycrystalline MgO might have been caused a poor surface coverage of the MgO film on the GaAs. Iron atoms would have been able to diffuse into the GaAs and form compounds with higher resistivity.
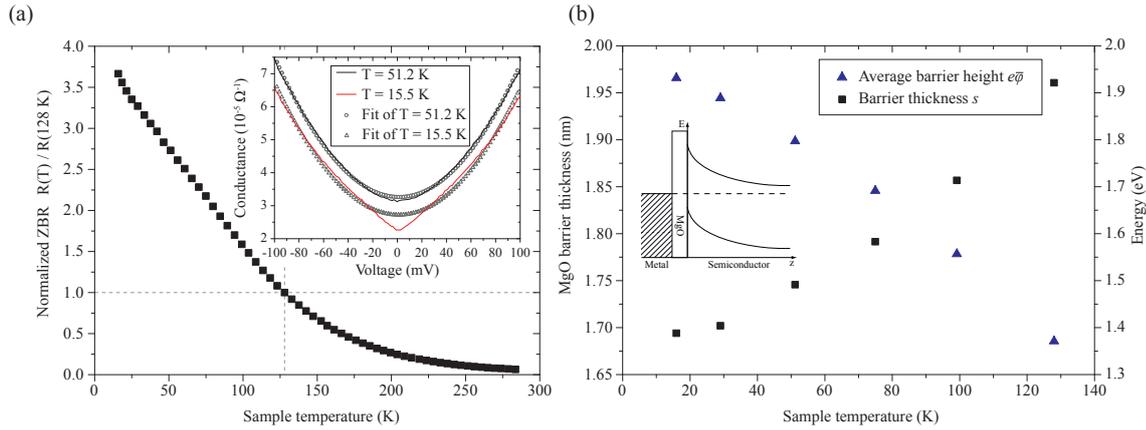
Figure 4.19.: The graph in (a) presents the normalized *ZBR* as a function of sample temperature. In the inset the red and black solid curves are conductance data taken at sample temperatures of $15.5\,\text{K}$ and $51.2\,\text{K}$, respectively. The grey triangles and circles are corresponding fits of the data. (b) Average height $\bar{\varphi}$ and thickness s of the potential barrier as a function of temperature. The inset shows a sketch of the hybrid structure's energy-band diagram.

Without annealing the hybrid structure with the $2\,\text{nm}$-thick MgO film seems to be the most promising candidate in relation to tunneling through the potential barrier. As discussed in section 2.2 the third Rowell criterion, a weak insulating-like temperature dependence of the *ZBR*, definitely confirms tunneling as the dominant transport path and rules out pinholes in the thin film. The normalized *ZBR* $R(T)/R(128\,\text{K})$ data as a function of the sample temperature in Figure 4.19(a) reveal a weak linear temperature dependence below $128\,\text{K}$ compared with the $4\,\text{nm}$ and $6\,\text{nm}$-thick MgO films. Based on the third Rowell criterion and observations from other groups[8, 9, 54, 70] it can be concluded that tunneling is the dominant transport mechanism through the $2\,\text{nm}$-thick MgO barrier.

The inset in Figure 4.19(a) presents two examples of conductance curves and corresponding fits of the data for the hybrid structure with the $2\,\text{nm}$-thick MgO film at sample temperatures of $15.5\,\text{K}$ and $51.2\,\text{K}$. The fits matches the data by $98.1\,\%$ and $99.7\,\%$, respectively. The data were fitted with the Brinkman, Dynes and Rowell model for an asymmetric barrier by applying equation 2.9. The parabolic fit of the model yield the

coefficients $K_0\left(\bar{\varphi}, s\right)$, $K_1\left(\bar{\varphi}, \Delta\varphi, s\right)$ and $K_2\left(\bar{\varphi}, s\right)$ which result in the average height $\bar{\varphi}$, the thickness s and asymmetry $\Delta\varphi$ of the potential barrier as shown in the equations 2.10 - 2.12. The average height $\bar{\varphi}$ and thickness s in figure 4.19(b) and also the not shown asymmetry $\Delta\varphi$ of the barrier exhibit a strong temperature dependence. The data seem to converge for low temperatures at around $15.5\,\mathrm{K}$ at values of $e\bar{\varphi} = 1.97\,\mathrm{eV}$, $s = 1.69\,\mathrm{nm}$ and $e\Delta\varphi = 0.18\,\mathrm{eV}$.

The temperature dependence of the characteristic tunnel barrier parameters might be explained by the positive band bending at the MgO/highly-doped GaAs interface[141, 142]. The depletion region is depicted by a sketch of the structure's energy-band diagram in the inset in Figure 4.18(b). The model of Brinkman, Dynes and Rowell describes the effective barrier of trapezoidal shaped tunnel barriers between two materials. It might be not sufficient to completely describe the electron tunneling transport across the interfaces of the iron/MgO/modulation-doped GaAs structure with the rectangular shaped barrier on the semiconductor side. Combinations of different transport models might have to be consider to completely describe the electron transport across the potential barriers[131].

In contrast to the hybrid structure with the $2\,\mathrm{nm}$-thick MgO film the ones with the $4\,\mathrm{nm}$ and $6\,\mathrm{nm}$-thick MgO exhibit a stronger temperature dependence of the *ZBR* in Figures 4.18(a) and 4.18(c). This indicates a reduced tunneling probability. Thermionic-field emission might dominate the electron transport through the barrier also at low temperatures.

4.3. Inverted, modulation-doped InAs heterostructures

The relative high electron mobilities and spin-orbit interaction makes inverted, modulation-doped InAs heterostructures appealing for spintronic applications. A major issue in the fabrication of the heterostructures is the lack of a substrate with suitable lattice parameter. This led to the design of the metamorphic $In_xAl_{1-x}As$ buffer layers to accommodate the lattice mismatch between GaAs and InAs. The first study in section 4.3.1 investigates the strain relaxation within these buffer layers with and without an additional AlAs/GaAs superlattice (*SL*). The second part in section 4.3.2 focuses on the influence of the indium content on the surface morphology of the InAs heterostructure and the transport properties of the embedded two-dimensional electron gas.

4.3.1. Strain relaxation in metamorphic InAlAs buffers

This study comprises the investigation of strain relaxation processes in step-graded metamorphic $In_xAl_{1-x}As$ buffer layers with an additional AlAs/GaAs *SL* using *HRXRD* and atomic force microscopy (*AFM*)[143]. The results are compared to a reference sample with an identical layer design except the AlAs/GaAs *SL*. The relaxation of the individual layers was accessed by symmetrical $\omega - 2\theta$ scans along the crystal truncation rod in the vicinity the GaAs [004] reflex. The texture of the metamorphic buffer is discussed by constructing pole figures of the GaAs substrate, the underlying AlAs/GaAs *SL*, as well as the bottom and top metamorphic buffer layers. The layer design of the metamorphic $In_xAl_{1-x}As$ buffer is presented in figure 4.20(a).

The surfaces of the top $In_{0.75}Al_{0.25}As$ layer on the sample in Figure 4.20(b) and the reference in Figure 4.20(c) reveal a cross-hatch morphology. The periodic surface structures within the cross-hatches have a maximal height of $30\,nm$ and average roughness of $RMS= 3.67\,nm$ and $RMS= 7.70\,nm$, respectively. The height variations for the sample with *SL* are anisotropic and much smaller in the [$\bar{1}10$] crystal direction than in the [110] direction. The *AFM* image of the $In_{0.75}Al_{0.25}As$ layer surface in Figure 4.20(b) indicates that relaxation took place within the metamorphic buffer. The inset of Figure 4.20(b) shows a line scan along the [110] direction, and indicates an asymmetric surface morphology. The formation of this morphology is probably due to a number of α- and β-dislocations which released strain within the buffer layers[37, 144]. The sample without the AlAs/GaAs *SL* in Figure 4.20(c) shows a homogeneous, scaly surface. Furthermore, there are holes on the surface with edges along $< 010 >$ directions. These features are attributed to defects resulting from the strain relaxation process. It seems that the defects arise in pairs on the surface. The inset of Figure 4.20(c) shows the linescan along the

[110] direction. It is marked with a dashed white line on the surface. The holes exhibit diameters of up to 800 nm and depths of about 80 nm.
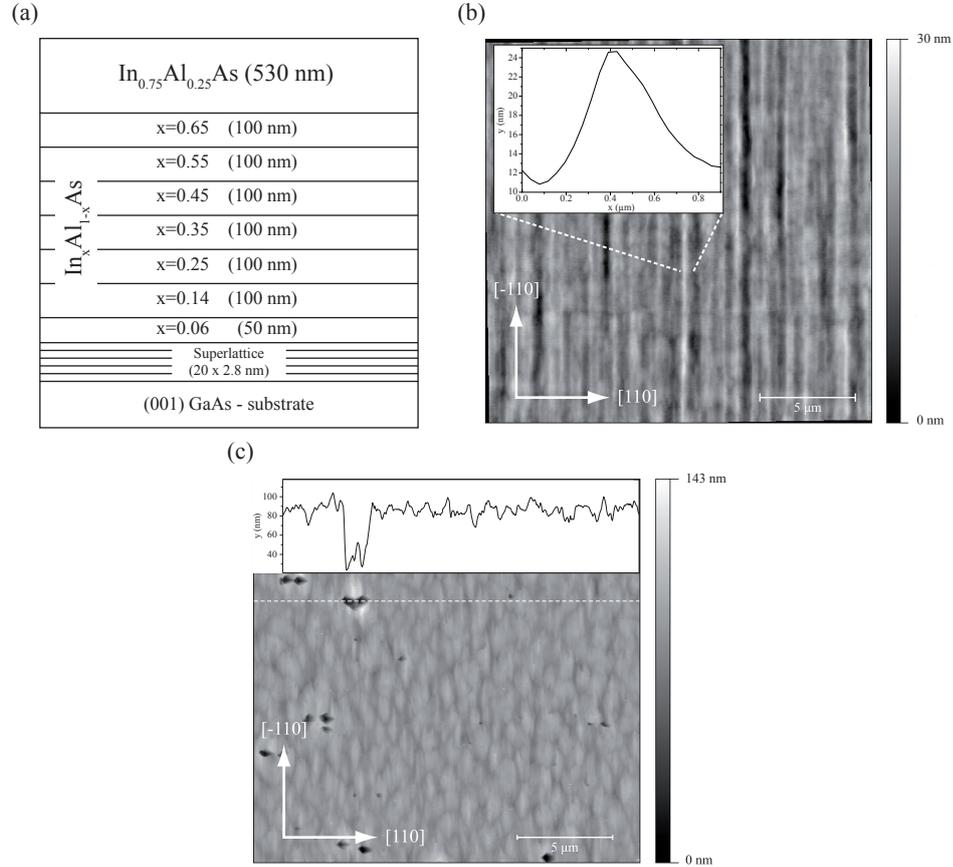
Figure 4.20.: (a) Sample design of the metamorphic $In_xAl_{1-x}As$ buffer heterostructure. (b) Atomic force microscopy image of the $In_{0.75}Al_{0.25}As$ top-layer surface morphology of the sample with AlAs/GaAs *SL*. The inset shows the zoomed line scan at the marked position. (c) *AFM* image of the $In_{0.75}Al_{0.25}As$ top-layer surface morphology of the reference sample without AlAs/GaAs *SL*. The inset shows the line scan at the marked position along the [110] direction.

Figure 4.21 shows the [004] $\omega - 2\theta$-scans of the GaAs, $In_xAl_{1-x}As$ metamorphic buffer and $In_{0.75}Al_{0.25}As$ layer peaks with (black curve) and without (red curve) an AlAs/GaAs *SL*. The theoretical peak positions marked with the dashed lines in Figure 4.21 are calculated using Vegard's law from the nominal indium contents of the layers according to the growth protocol and the Riber 32p *MBE* system calibration.

In the case of the virtual substrate with an AlAs/GaAs *SL*, the peaks of the $In_xAl_{1-x}As$ metamorphic buffer layers, as well as the $In_{0.75}Al_{0.25}As$ layer are well pronounced with a
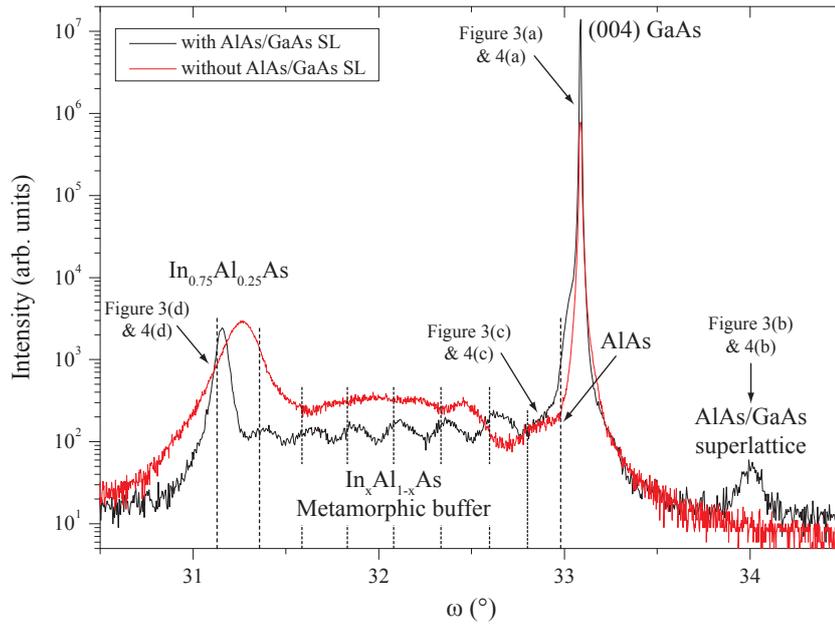
Figure 4.21.: Symmetrical $\omega - 2\theta$-scan along crystal truncation rod of GaAs (004) and $\mathsf{In}_x\mathsf{Al}_{1-x}\mathsf{As}$ (004) peaks. The dashed lines are expected ω values of AlAs and the $\mathsf{In}_x\mathsf{Al}_{1-x}\mathsf{As}$ layers (corresponding x values are shown in figure 4.20(a))

full width of half maximum (*FWHM*) of $0.059\,°$. The shoulder to the left of the GaAs peak is due to the AlAs layers of the AlAs/GaAs *SL*. Furthermore, it has been confirmed experimentally by an asymmetrical scan along the [115] peak that the layers are fully relaxed. The experimental peak positions are in agreement with the expected ones. The nominal versus experimentally calculated indium content deviate by only $2\,\%$. In addition, a satellite peak at $\omega \approx 34°$ is associated with the AlAs/GaAs *SL*. Based on simulation calculations, another peak is expected at $\omega \approx 32°$. However, it cannot be observed due to the overlapping diffraction signals of the metamorphic buffer.

The *HRXRD* scan of the reference sample in Figure 4.21 shows clear peaks at the angles associated with the GaAs substrate and the $\mathsf{In}_{0.75}\mathsf{Al}_{0.25}\mathsf{As}$ top-layer. The InAlAs top-layer peak has a large *FWHM* of $0.168\,°$. A relaxation of the top layer up to $92\,\%$ was determined by comparing scans of the [004] and [115] peaks. As a result of the incomplete strain relaxation in the reference sample, the peaks associated with the $\mathsf{In}_{0.75}\mathsf{Al}_{0.25}\mathsf{As}$ top-layer and step-graded $\mathsf{In}_x\mathsf{Al}_{1-x}\mathsf{As}$ layers are shifted to smaller vertical lattice constants.

In both *HRXRD* investigations in Figure 4.21 broadening of the peaks is caused by incomplete lattice relaxation combined with in-plane fluctuations of indium content within the metamorphic buffer. The stress caused by lattice mismatch is most likely

reduced through the formation of dislocations at the interfaces[145]. Indium diffusion during growth has consequences on the interface roughness[146]. Indium concentration fluctuations within the layers were also observed as black/white contrasts in transmission electron micrographs (*TEM*) of comparable heterostructures in the [110] direction[37]. In particular, in the reference sample containing no AlAs/GaAs *SL*, the peak to valley ratio is very low and the peaks are strongly broadened. In the sample with the AlAs/GaAs *SL*, the topmost layers of the buffer contain much less defects than in the reference without *SL*. This result is consistent with the *FWHM* of these layer-related peaks in figure 4.21, whereby the *FWHM* of the sample without AlAs/GaAs *SL* is 2.8 times bigger.

The texture of the buffer layers was analyzed by constructing [004] reflex pole figures of the GaAs substrate, AlAs/GaAs *SL*, $In_{0.06}Al_{0.94}As$ buffer layer and $In_{0.75}Al_{0.25}As$ layer. The measurements covered intervals of $0° < \psi < 4°$ and $0° < \phi < 360°$ in steps of $\Delta\psi = 0.5°$.
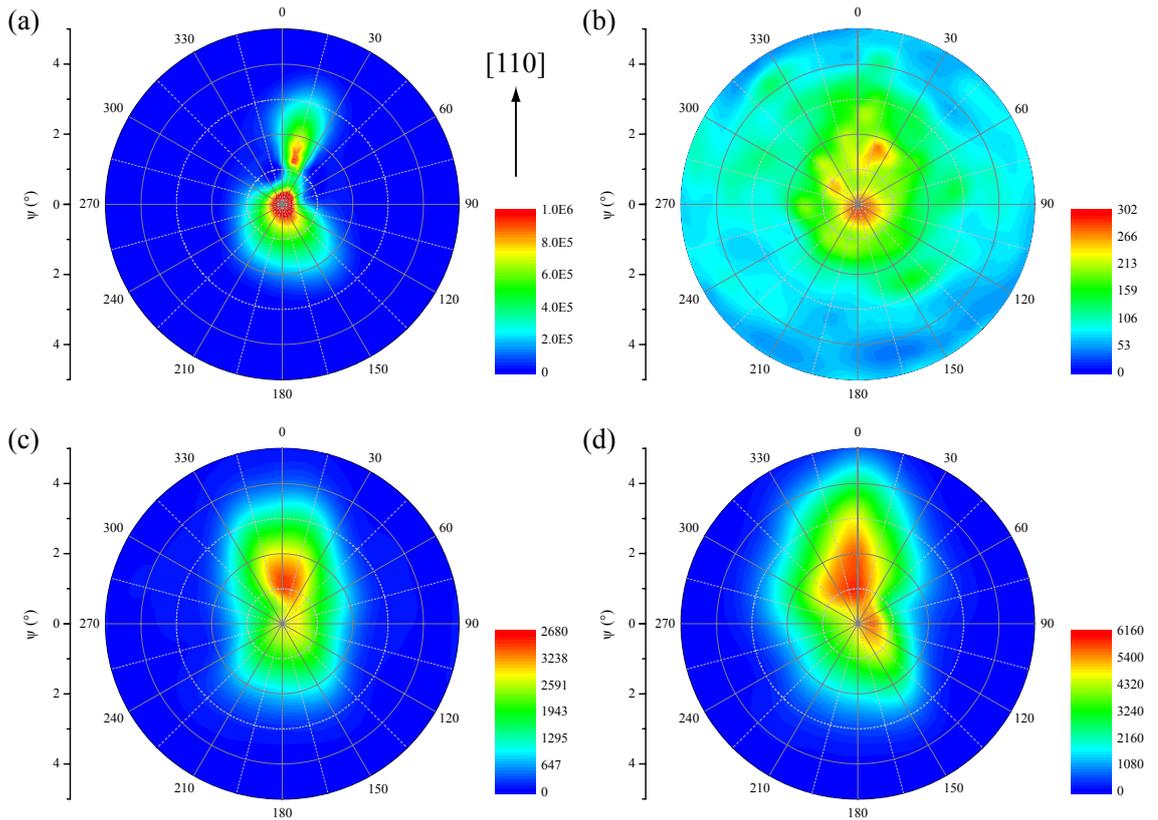
Figure 4.22.: Pole figures of the layer stack with additional AlAs/GaAs *SL* of the (004) peaks of (a) the GaAs-substrate, (b) the AlAs/GaAs *SL*, (c) the $In_{0.06}Al_{0.94}As$ layer and (d) the $In_{0.75}Al_{0.25}As$ layer.

Figure 4.22 shows pole figures of the GaAs [004] substrate peak, AlAs/GaAs *SL* peak, $In_{0.06}Al_{0.94}As$ layer peak and $In_{0.75}Al_{0.25}As$ layer peak, respectively. The maxima of diffracted intensity from the GaAs substrate peak is observed in Figure 4.22(a) at $\psi = 0°$. This pole figure shows an additional peak which is tilted by an angle $\psi \sim 1.4°$ relative to the GaAs substrate. The peak is about 30 degrees broad and occurs at $\phi \sim 15°$. Figure 4.22(b) shows diffraction intensities originating from the AlAs/GaAs *SL* on top of the GaAs substrate. Two peaks similar to those of the GaAs substrate are observed. The peaks are surrounded by a distorted intensity cloud, which indicates multiple dislocations in the vicinity of the AlAs/GaAs *SL*. The pole figure in 4.22(c) shows the $In_{0.06}Al_{0.94}As$ layer above the AlAs/GaAs *SL*. An asymmetrical-shaped peak can be observed at $\phi = 3.60°$ and $\psi = 1.16°$. This broadened peak has a long axis in the [110] crystal directed and a shorter one in the [$\bar{1}$10] crystal direction. Figure 4.22(d) shows the strongly asymmetrically broadened $In_{0.75}Al_{0.25}As$ layer peak. Another smaller peak can be observed at $\phi = 81°$, $\psi = 0.36°$.
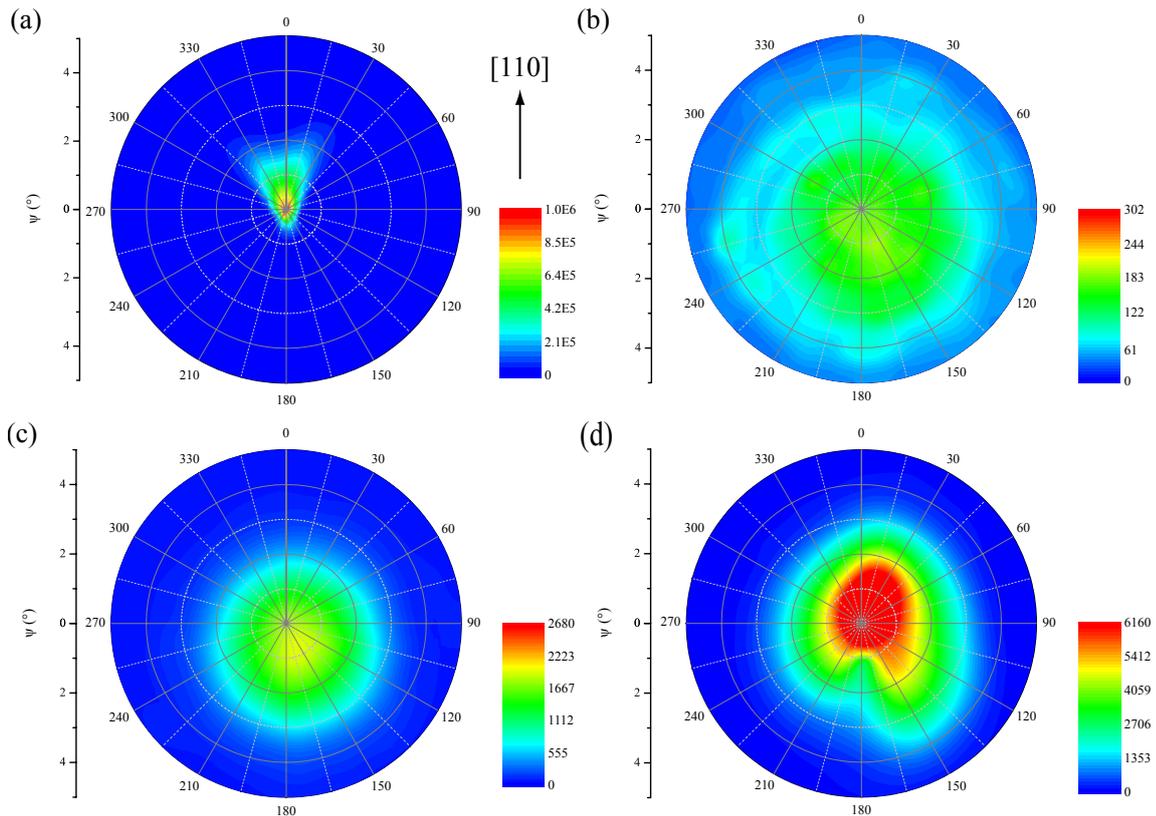
Figure 4.23.: Pole figures of the reference layer stack, that contains no AlAs/GaAs *SL*. Pole figure of the (004) peaks of (a) the GaAs-substrate, (b) the position where the AlAs/GaAs *SL* was measured, (c) the $In_{0.06}Al_{0.94}As$ layer and (d) the $In_{0.75}Al_{0.25}As$ layer.

Figure 4.23 shows the corresponding pole figures of the reference sample taken at the same angular positions as the ones in Figure 4.22, i.e., in Figure 4.23(a) the pole figure is taken at the GaAs [004] substrate peak, in Figure 4.23(b) at the position where the satellite AlAs/GaAs *SL* peak was measured, in Figure 4.23(c) at the $In_{0.06}Al_{0.94}As$ peak and in Figure 4.23(d) at the $In_{0.75}Al_{0.25}As$ layer peak. The color scale of the pole figures is identical to those in Figure 4.22. The GaAs substrate peak is observed at $\psi = 0\,°$. Note the considerable large foothill in the [110] direction in Figure 4.23(a). In contrast to the sample with AlAs/GaAs *SL*, Figure 4.23(b) shows no distinct peaks at the position where the satellite peak of the AlAs/GaAs *SL* was measured but the intensities of the GaAs foothill. The pole figure in 4.23(c) shows the first $In_{0.06}Al_{0.94}As$ layer above the GaAs substrate. The maximum of the peak occurs at $\psi = 0.7\,°$ and $\phi = 155\,°$ whereby the intensity is distributed isotropic from there on. Figure 4.23(d) shows the pole figure of the top metamorphic buffer layer. It has a maximum located at $\psi = 0.15\,°$ and $\phi = 50\,°$ and is asymmetrically broadened.

The texture, i.e., crystallographic orientation distribution of the sample with AlAs/GaAs *SL* in Figure 4.22 indicate that the strain within the metamorphic buffer relaxed via the combination of a pure and a simple shear components[147]. The results show that the AlAs/GaAs *SL* absorbed strain in the virtual substrate caused by lattice mismatch of the overgrown $In_xAl_{1-x}As$ metamorphic buffer. This is coherent with other investigations on similar structures[30, 37, 38]. From the presence of two distinct peaks in the pole figures of the AlAs/GaAs *SL* in Figure 4.22(b), which replicate those originating from the surface, it can be concluded that the dislocations propagate through the AlAs/GaAs *SL* into the GaAs substrate. This defect propagation led to the formation of distinctly twisted fractions in the substrate. These fractions are tilted crystallites which are separated and surrounded by defects. The twisted fractions give an idea of the mechanism by which the stress within the system has been reduced.

The comparison of samples with and without AlAs/GaAs *SL* clearly shows different strain relaxation behaviour. The introduction of an AlAs/GaAs *SL* released the strain more efficiently. It has been shown in previous studies that the introduction of an AlAs/GaAs *SL* enhances the carrier mobility in modulation-doped InAs heterostructures[38]. Thus, in the case of InAs heterostructures, twisted fractions located in the buffer layers are not necessarily bad since the AlAs/GaAs *SL* enables the structure to achieve a higher electron mobility than in samples containing no *SL* in the buffer. Complete strain relaxation and absence of defects in the top layer of the structure is obviously more important.

In the case of the sample with AlAs/GaAs *SL*, the *SL* layers are tilted by large angles of $\psi \approx 1.5°$ and $\phi \approx 20°$. It indicates that the *SL* absorbed stress caused by the overgrown metamorphic buffer layers. The stress was probably reduced by misfit and threading dislocations confined in the AlAs/GaAs *SL*. It has been shown that threading dislocations are located predominantly in the AlAs/GaAs *SL*[38]. The tilt of the [004] peak of the *SL* is further supported by our *AFM* topograph (figure 4.20(b)), which reveals periodic structures with a periodicity of $100\,\text{nm} - 350\,\text{nm}$ and tilt angles between $\psi = 1.2° - 1.8°$. Our results are consistent with the *TEM* study on similar structures[37]. In this investigation, the presence of black/white contrasts in a transmission electron micrograph indicates the same tilt. The micrograph shows periodic vertical contrast lines with a periodicity of $120\,\text{nm} - 340\,\text{nm}$ and a tilt angle of about $\psi = 1.5°$. The data of the reference in figure 4.23 show no strong tilt of the [004] peak. This result is also consistent with the transmission electron micrograph[37] and the *AFM* topography (figure 4.20(c)).

As discussed by Romanov et al.[145], the introduction of intentionally strained layers can reduce the density of threading dislocations. In this study, the introduction of a strained AlAs/GaAs *SL* before growth of the step-graded metamorphic $In_xAl_{1-x}As$ buffers reduced strain and the density of threading dislocations[37]. Strain is released by the activation of dislocation sources at the interfaces of the $In_xAl_{1-x}As$ metamorphic buffer and the AlAs/-GaAs *SL*. These misfit dislocations move along the interfaces and leave the structure. The threading dislocation density is decreased by annihilation through induced defect interaction.

4.3.2. Influence of the indium content on the transport properties of the InAs/In_xGa$_{1-x}$As quantum well

This section focuses on the influence of the indium content on the transport properties of inverted, modulation-doped InAs heterostructures. In 2004, Dr. Ch. Heyn fabricated a sample series with different indium contents x in the top $In_xAl_{1-x}As$ layer of the metamorphic buffer and the vicinity of the quantum well region. The nominal indium contents were $x = 0.60$, $x = 0.65$, $x = 0.70$ and $x = 0.75$ according to the fabrication protocol. The layer design of the heterostructure is shown in Figure 3.7(b).

The indium content of the $In_xAl_{1-x}As$ layers was investigated using *HRXRD*. Symmetrical $\omega - 2\theta$ scans in the vicinity of the GaAs [004] reflex were performed along the crystal truncation rod. The indium contents were determined by extracting the $In_xAl_{1-x}As$ layer peak positions and using Vegard's law. In addition, asymmetrical scans of the [115] reflex

confirmed that the layers are fully relaxed. The data revealed slightly higher indium contents of $x = 0.617$, $x = 0.672$, $x = 0.718$ and $x = 0.767$ compared with the nominal indium contents expected from the Riber 32p *MBE* system calibration.

Figure 4.24 displays *AFM* images of the top $In_xAl_{1-x}As$ layer surface morphology. The structures show cross-hatch morphologies with periodicities between 100 nm and 300 nm in the [110] and about $1\,\mu$m in the [$\bar{1}$10] crystal direction[148]. The periodic structures within the cross-hatch have a maximal height of 30 nm and average roughnesses of $RMS= 3.73$ nm, $RMS= 3.7$ nm, $RMS= 3.38$ nm and $RMS= 2.67$ nm for the indium contents of $x = 0.617$, $x = 0.672$, $x = 0.718$ and $x = 0.767$, respectively. The height variations in the [$\bar{1}$10] direction are much smaller compared to the [110] crystal direction. Clearly, the periodic structure vanishes with decreasing indium content in the [$\bar{1}$10] crystal direction and the asymmetry of the surface morphology increases.
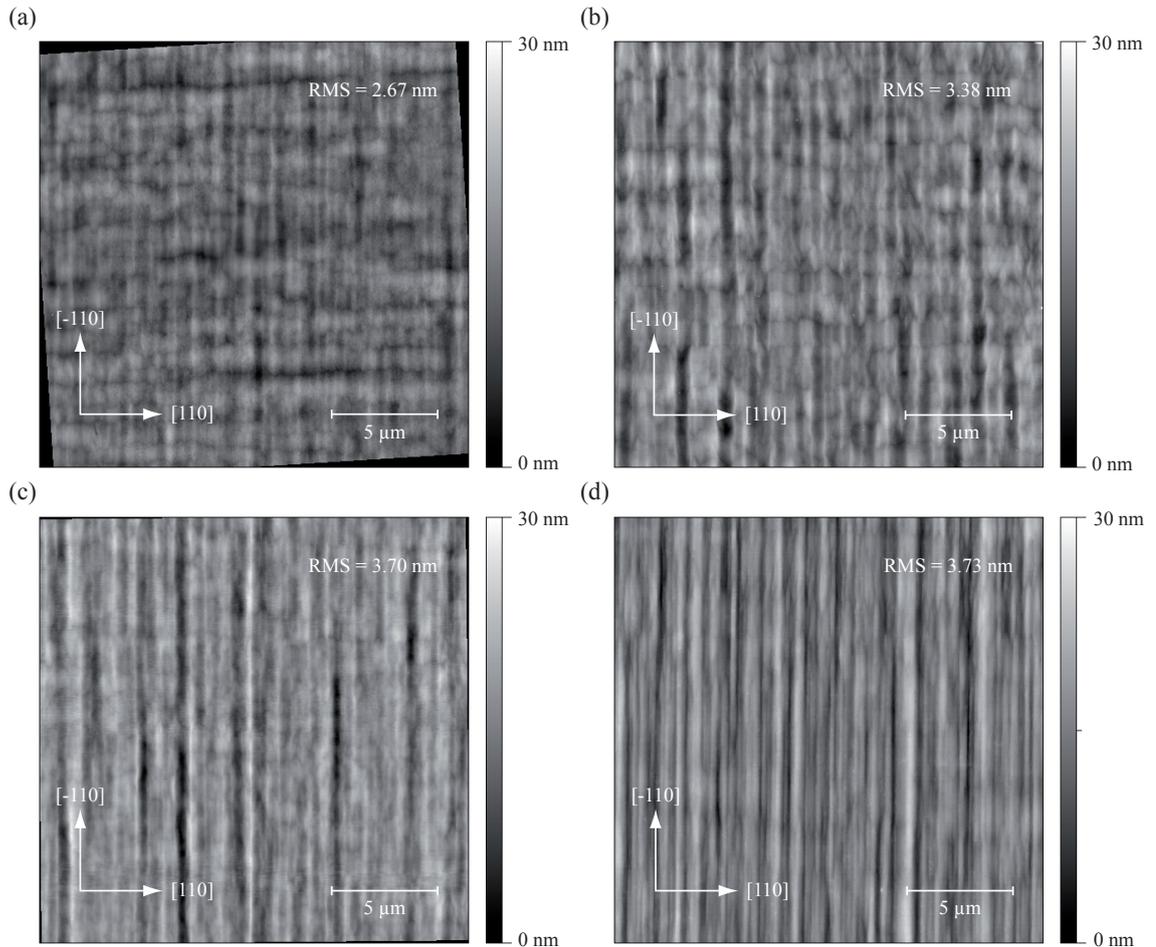
Figure 4.24.: *AFM* micrographs of the top $In_xAl_{1-x}As$ layer surface morphology with the indium contents of (a) $x = 0.767$, (b) $x = 0.718$, (c) $x = 0.672$ and (d) $x = 0.617$.

In 2004, Dr. S. Löhr performed magneto-transport measurements on the presented heterostructures at helium temperature. In 2011, L. Liefeith conducted similar magneto-transport measurements for other sample pieces of this InAs heterostructure series[149]. The data from the Shubnikov-de Haas oscillations and the quantum Hall effect was used to characterize the electron mobility μ of the embedded two-dimensional electron system for various carrier concentrations n_s[150]. In both investigations the carrier concentration was varied using an infrared light-emitting diode with the wavelength of $\sim 940\,\mathrm{nm}$. The preparation of the L-Hallbar structure used to measure the Shubnikov-de Haas oscillations and the quantum Hall effect in two different crystal direction simultaneously is described in section 3.6. Further information about the experimental setup and the magneto-transport measurements are supplied in section 3.7.
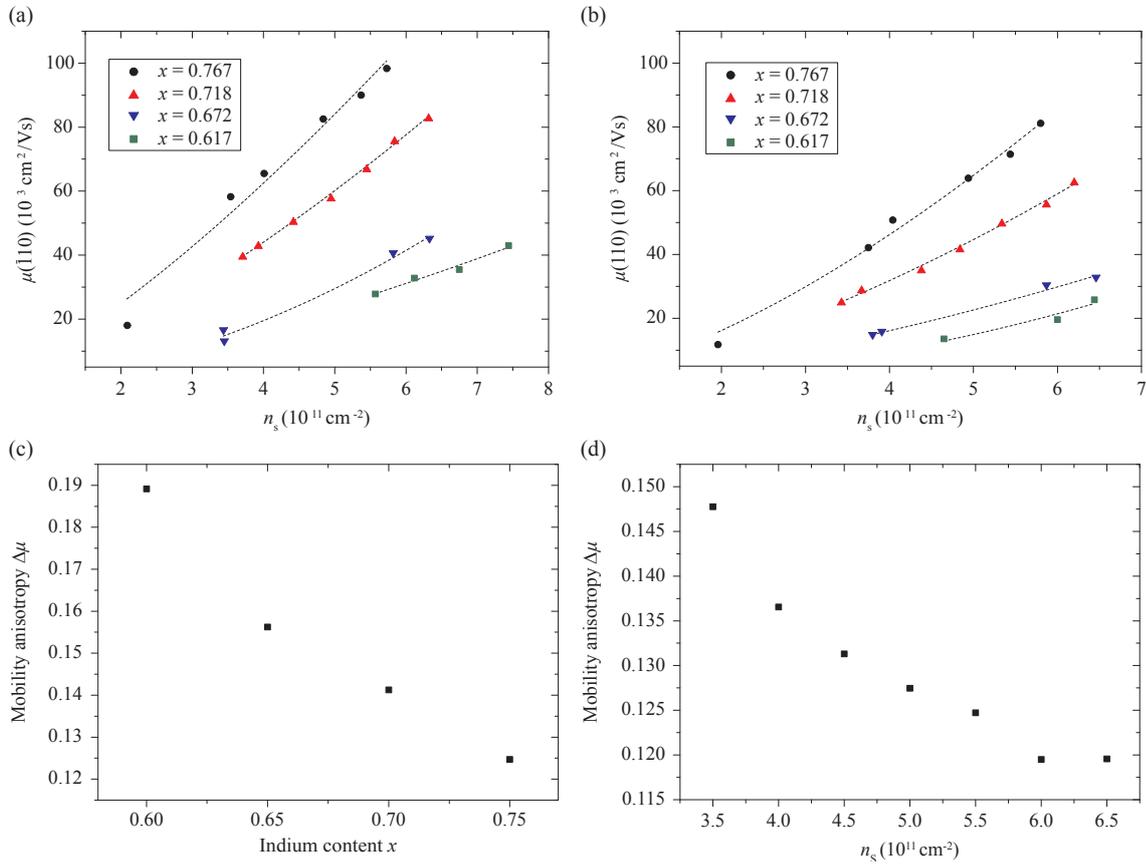
Figure 4.25.: Transport properties of modulation-doped InAs heterostructures with indium contents of $x = 0.617$, $x = 0.672$, $x = 0.718$ and $x = 0.767$. The graphs in (a) and (b) depict the electron mobility as a function of the carrier concentration in the $[\bar{1}10]$ and $[110]$ crystal directions, (c) the mobility anisotropy versus the indium content for the carrier concentration of $n_s = 5.5 \times 10^{11}\,\mathrm{cm}^{-2}$ and (d) the mobility anisotropy as a function of the carrier concentration for the indium content of $x = 0.767$.

Figure 4.25 presents the data from the magneto-transport measurements of Dr. S. Löhr. Figure 4.25(a) and 4.25(b) show the electron mobility μ as a function of the carrier concentration n_s in the $[\bar{1}10]$ and $[110]$ crystal directions for various indium contents. In the graphs the dashed lines depict fits of the allometric form $\mu \sim n_s^{\gamma}$. Clearly, the electron mobility is systematically lower in the $[110]$ than in the $[\bar{1}10]$ crystal direction[30]. The data show that the mobility increases with increasing carrier concentration and decreases with decreasing indium content. The magneto-transport measurements of L. Liefeith revealed similar results for the electron mobilities of these heterostructures.

Figure 4.25(c) displays the anisotropy of the mobility versus the indium content x for the carrier concentration of $n_s = 5.5 \times 10^{11}\,\mathrm{cm}^{-2}$. Here, the mobility anisotropy $\Delta\mu$ is defined as: $(\mu([\bar{1}10]) - \mu([110]))/(\mu([\bar{1}10]) + \mu([110]))$. The data reveal that the anisotropy decreases with increasing indium content.

The graph in Figure 4.25(d) shows the electron mobility anisotropy as a function of the carrier density for the structure with the indium content of $x = 0.75$. The anisotropy decreases with increasing carrier concentration and seems to converge for higher electron densities. Screening of the impurity potentials[151] might explain the decreasing anisotropy with increasing carrier density in the InAs quantum well region. In the $In_xGa_{1-x}As$ quantum well region this effect has been discussed by the transmission of carriers with higher energy which thus can overcome the energy barriers of the undulated conduction band profile[152].

The formation of the cross-hatch morphologies in Figure 4.24 is most likely due to anisotropic generation and different densities of α- and β-dislocations[37, 144]. These dislocations released the misfit strain within the metamorphic buffer layers[143]. It has been shown that charged threading dislocations can act as extended remote impurities impacting the electron mobility asymmetrical in these heterostructures[153–155]. The allometric fits of the electron mobility as a function of the carrier concentration in Figure 4.25(a) and 4.25(b) yield the average exponents of $\gamma = 1.51 \pm 0.13$ in the $[\bar{1}10]$ and of $\gamma = 1.64 \pm 0.23$ in the $[110]$ crystal direction. These values indicate that mainly remote impurities due to remote impurity doping and threading dislocations limit the mobility of the electrons in the two-dimensional electron gas[156, 157]. Accordingly, the different densities of threading dislocations in the $[110]$ and $[\bar{1}10]$ crystal direction would lead to the observed anisotropic electron mobility in the quantum well region. Ercolani et al. have shown that conduction band minimum modulations due to indium fluctuations lead to transport asymmetries in $In_xGa_{1-x}As$ quantum wells[152]. In the case of inverted,

modulation-doped InAs heterostructures the wave function of the electron system is mainly located in the InAs layer[158] so that the contribution of the conduction band modulation in the $In_xGa_{1-x}As$ layer to the transport anisotropy might be not as strong as anisotropic scattering at charged threading dislocations in the InAs layer. But notice, that a modulated strain field may be present in the InAs layer caused by the surrounded $In_{1-x}Ga_xAs$ leading to modulations of the conduction band minimum energy in the InAs well[30, 152].

At low indium contents the relaxation of misfit strain between the $In_xGa_{1-x}As$ and the InAs could also lead to the reduced electron mobility due to formation of dislocations at the $InAs/In_xGa_{1-x}As$ interface. The InAs layer has the critical thickness of about $6\,nm$ for the structure with an indium concentration of $x = 0.75$[148]. In the case of lower indium concentrations the InAs might relax for thicknesses smaller than $6\,nm$.

The evolution of the anisotropic surface morphologies in Figure 4.24 and the mobility anisotropy in Figure 4.25(c) suggests strong correlation between structural and transport properties of these heterostructures. The *AFM* images in Figure 4.24 show an decreasing anisotropy of the surface morphology with increasing indium content reflected by the decreasing average roughness. The arising periodic features in the $[\bar{1}10]$ crystal direction for higher indium concentrations indicate relaxation within the $In_xAl_{1-x}As$ metamorphic buffer. This relaxation is related to the increasing misfit strain between the GaAs substrate and the $In_xAl_{1-x}As$ layers with increasing indium content. Accordingly, the observed anisotropic relaxation leads to a higher density of threading dislocations within the structure in the $[\bar{1}10]$ crystal direction which most likely results in the decreasing mobility anisotropy.

The magneto-transport and *AFM* investigations accessed the structural and transport properties of the inverted, modulation-doped InAs heterostructures with indium contents of $60\,\%$, $65\,\%$, $70\,\%$ and $75\,\%$. The results suggest correlation between the morphology of the surface and electron mobility of the two-dimensional electron gas. With regard to future spin-injection experiments, a higher indium content within the top $In_xAl_{1-x}As$ layers of the metamorphic buffer and the $In_xGa_{1-x}As$ layers below and above the InAs region leads to a lower the density of dislocations in the vicinity of the quantum well region. This reduces the events of electron-impurity scattering and increases the spin lifetime related to the Elliott-Yafet spin relaxation mechanism[57].

4.4. Iron on inverted, modulation-doped InAs heterostructure

The following section comprises the investigations of iron films deposited on inverted, modulation-doped InAs heterostructures. It contains results about strain relaxation during the deposition of iron, in-plane magnetic properties as the crystal directions of magnetic axes and magnetic anisotropies of the iron films and electrical properties of the iron/$In_x Al_{1-x}$As interface. The sample design and deposition sequences of this structure are described in section 3.1.4.

4.4.1. Strain relaxation during the deposition of iron

This study focuses on investigating the strain evolution of iron films on inverted, modulation-doped InAs heterostructure during the deposition of iron. In this regard, in-situ *RHEED* was applied to access the temporal course of surface morphology as well as the in-plane lattice constant. During *RHEED* measurements the electron beam was aligned in the [110] crystal direction. Ex-situ *HRXRD* measurements were performed to investigate the out-of-plane lattice constant and texture of the iron films.
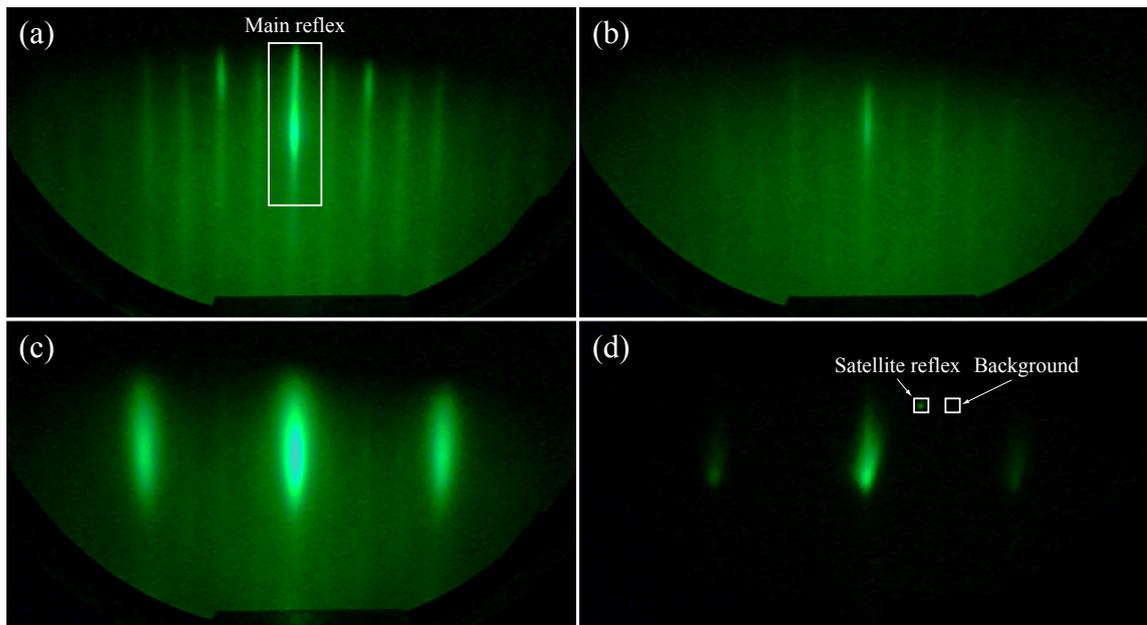
Figure 4.26.: *RHEED* pattern of (a) the $In_{0.75}Al_{0.25}$As substrate and of iron films deposited with 0.4093 nm/min on this substrate with layer thicknesses of (b) 0.4 nm, (c) 4.8 nm and (d) 80 nm, respectively.

Figure 4.26 shows *RHEED* patterns of the $In_{0.75}Al_{0.25}$As substrate as well as iron films at various stages of the deposition process. Before deposition of iron the semiconductor

structures had an arsenic terminated surface with a (2×4) surface reconstruction, as it is shown in Figure 4.26(a). During iron deposition streaky patterns arise as shown in Figures 4.26(b) to 4.26(d). The shape of the reflexes change its form with increasing iron film thickness.
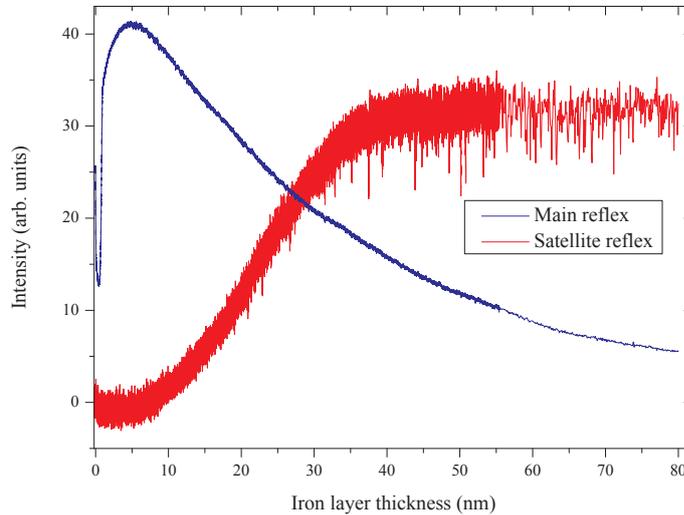
Figure 4.27.: Course of the integrated intensity of the main and the satellite reflex as a function of the iron layer thickness.

The temporal course of the *RHEED* patterns reveals that the intensity of the reflexes changes during deposition. This was examined by integrating the intensity of the main reflex (area delineated by a white solid line in Figure 4.26(a)) which mainly reflects the roughness of the surface. The blue curve in Figure 4.27 presents the integrated intensity data as a function of the iron layer thickness. The intensity drops immediately after the start of deposition. This decrease is most likely due to the formation of islands on the $In_{0.75}Al_{0.25}As$ surface[16]. The subsequent increase of the intensity indicates coalescence and smoothing of the iron surface. Accordingly, with increasing film thickness the intensity decreases indicating roughening of the surface. Ex-situ atomic force microscopy measurements confirmed such surface roughening with increasing layer thickness.

The *RHEED* pattern of the 80 nm-thick iron film features an satellite reflex arising during iron deposition. This reflex is marked by a square in Figure 4.26(d). The intensity course of the satellite reflex was investigated by integrating its and the background's intensity and plotting whose difference as a function of the iron layer thickness. The red curve in Figure 4.27 reveals that the reflex arises at thicknesses larger than ~ 5 nm. This and also the change of the main reflex's shape indicate restructuring of the surface morphology and the formation of in-plane misaligned islands on the surface of the iron film.
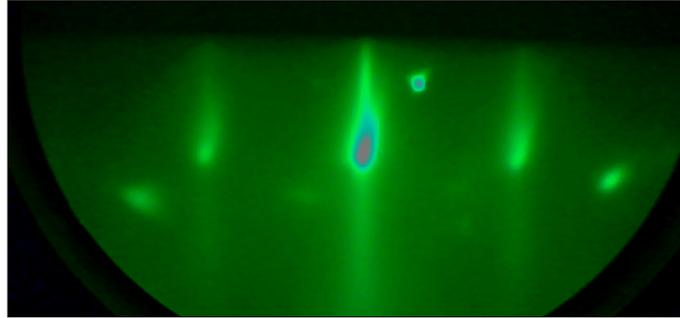
Figure 4.28.: *RHEED* pattern of a 80 nm-thick iron film fabricated with the deposition rate of 0.58nm/min.

A sample with the higher deposition rate of 0.58 nm/min and same iron film thickness depicted similar and even more pronounced features supporting the assumption of in-plane misaligned islands. Figure 4.28 shows the *RHEED* pattern of the 80 nm-thick iron film. In addition, the data reveal an asymmetric evolution the main reflex's shape. This is also the case for iron films on modulation-doped GaAs (001) structures as discussed in section 4.1.1.

The *RHEED* patterns in Figure 4.26 indicate an epitaxial relationship between the iron and the $In_{0.75}Al_{0.25}As$. Thereby, the lateral distance between two neighboring stripes in the pattern of the iron film is twice the distance as between the stripes generated by the $In_{0.75}Al_{0.25}As$. This is due to the fact that the lattice constant of iron (0.28664 nm) is roughly half the one of $In_{0.75}Al_{0.25}As$ (0.59776 nm). In regard to an in-plane epitaxial relationship, the most likely alignment between (001) iron and (001) $In_{0.75}Al_{0.25}As$ would be two iron unit cells for every $In_{0.75}Al_{0.25}As$ unit cell to reduce the tensile strain to $\sim 3.8\%$.

The strain evolution during the deposition of iron was investigated by accessing the in-plane lattice constant via *RHEED*. The lattice constant was extracted from the lateral distance between the *RHEED* reflexes of the iron film in Figure 4.26 and determined with respect to the $In_{0.75}Al_{0.25}As$. The method is described in section 3.2.2. Figure 4.29 shows the evolution of the such determined in-plane lattice constant of iron on $In_{0.75}Al_{0.25}As$ and in comparison also of iron on GaAs versus the iron layer thickness. The dashed lines mark half the lattice constant of $In_{0.75}Al_{0.25}As$ (0.29888 nm) and GaAs (0.28267 nm) and the bulk value of iron (0.28664 nm), respectively. Clearly, at small layer thickness the data reflect the lattice constants of $In_{0.75}Al_{0.25}As$ and GaAs showing iron films with tensile and compressive strain. At these small layer thicknesses the strain of the iron films on $In_{0.75}Al_{0.25}As$ is larger than on GaAs. With increasing film thickness the in-plane
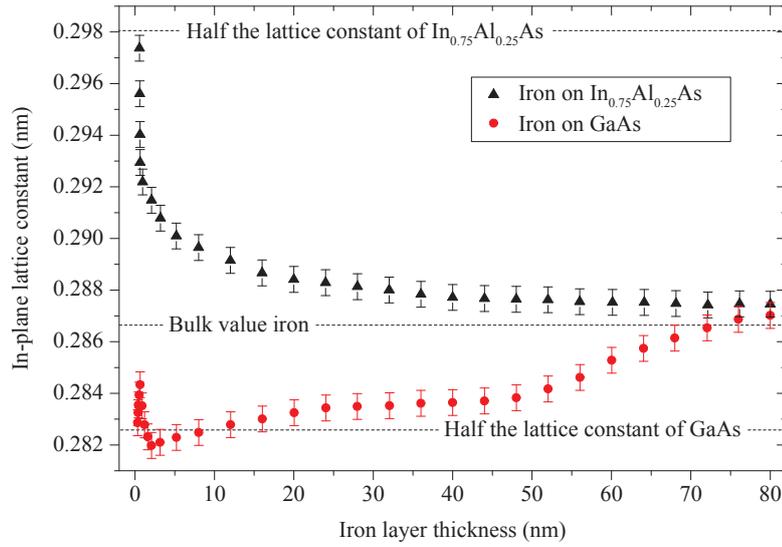
Figure 4.29.: (a) In-plane lattice constant of iron films on $In_{0.75}Al_{0.25}As$ and on GaAs as a function of the iron layer thickness.

lattice constant of iron on $In_{0.75}Al_{0.25}As$ decreases monotonically till it reaches the unstrained iron bulk value. At thicknesses beyond 5 nm the misfit strain is probably released by restructuring and the formation of in-plane misaligned islands as discussed above.

HRXRD was employed to further investigate the iron film on the inverted, modulation-doped InAs heterostructure. The black curve in Figure 4.30 shows data of a symmetrical scan along the crystal truncation rod of the GaAs [004] reflex. The experimental data were fitted using Pseudo-Voigt functions. The red solid line in Figure 4.30 displays the sum of the fits and the blue lines the individual fits. The dashed line marks the peak position for bulk unstrained iron. The experimental (002) iron peak is located at larger angles than the iron literature value. The leftmost peak in Figure 4.30 arises from the top $In_{0.75}Al_{0.25}As$ layer of the metamorphic buffer. The peaks of the metamorphic buffer between the $In_{0.75}Al_{0.25}As$ and the (002) iron peak are due to $In_xAl_{1-x}As$ layers with increasing indium content from larger to smaller angles.

In order to determine the out-of-plane lattice constant of the iron film the (002) iron peak position was extracted from the fitted X-ray diffraction data in Figure 4.30. The out-of-plane lattice constant resulted in 0.2847 nm using equation 3.3. The corresponding in-plane lattice constant of $a = 0.2877$ nm was calculated by assuming an isotropic in-plane lattice constant and the Poisson's ratio of 0.282[122]. Notice that the relaxed in-plane lattice constant is larger for the *RHEED* than for the *HRXRD* technique. This is due to
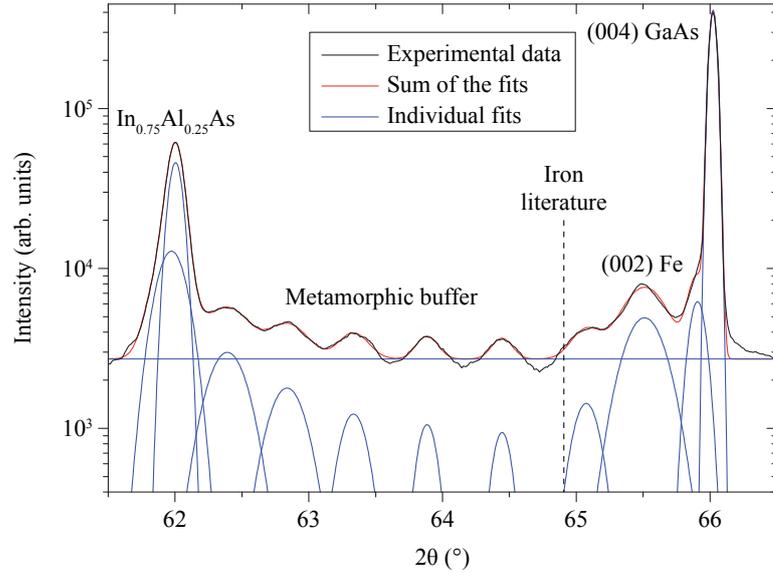
Figure 4.30.: Symmetrical $\omega - 2\theta$-scans and fits of the $80\,\mathrm{nm}$-thick iron film on inverted, modulation-doped InAs heterostructure. The graph shows each calculated contribution of the different layers as well as the calculated sum of the intensities.

the deeper penetration depth of the X-ray beam. It averages over all lattice constants of the iron film. In comparison, the average in-plane lattice constant of the *RHEED* data in figure 4.29 result in $0.2895\,\mathrm{nm}$. The difference to the *HRXRD* data might be explained by further relaxation of the iron lattice after deposition.

The texture of the iron films was studied by performing ω-scans at the ω-2θ position of the iron peaks for different in-plane crystal directions. The data revealed that the (002) planes of the iron are tilted by an angle of about $0.6°$ in the [110] crystal direction with respect to the GaAs substrate. This tilt is associated with elastic strain relaxation within the $\mathrm{In}_x\mathrm{Al}_{1-x}\mathrm{As}$ metamorphic buffer as discussed in section 4.3.1[143]. An additional iron peak was tilted in the opposite [$\bar{1}\bar{1}0$] crystal direction by an angle ω of about $0.3°$.

4.4.2. In-plane magnetic properties of the iron films

The in-plane magnetic properties of iron films on inverted, modulation-doped InAs heterostructures were studied using the room-temperature *MOKE* method. In the first part of this section, $8\,\mathrm{nm}$ and $3.2\,\mathrm{nm}$-thick iron films were investigated to determine the crystal directions of the film's in-plane magnetic axes. In these measurements, the external magnetic field was swept from $-90\,\mathrm{mT}$ to $90\,\mathrm{mT}$ in steps of about $0.2\,\mathrm{mT}$ for several rotation angles ψ. The second part focuses on the thickness dependence of the in-plane

magnetic anisotropies. It was studied by performing several Kerr measurements along an iron thickness gradient. The experimental *MOKE* setup, the calibration procedure of the samples, methods to analyze the results and used terms as polar plot and magnitude of the magnetization vector are described in section 3.5.
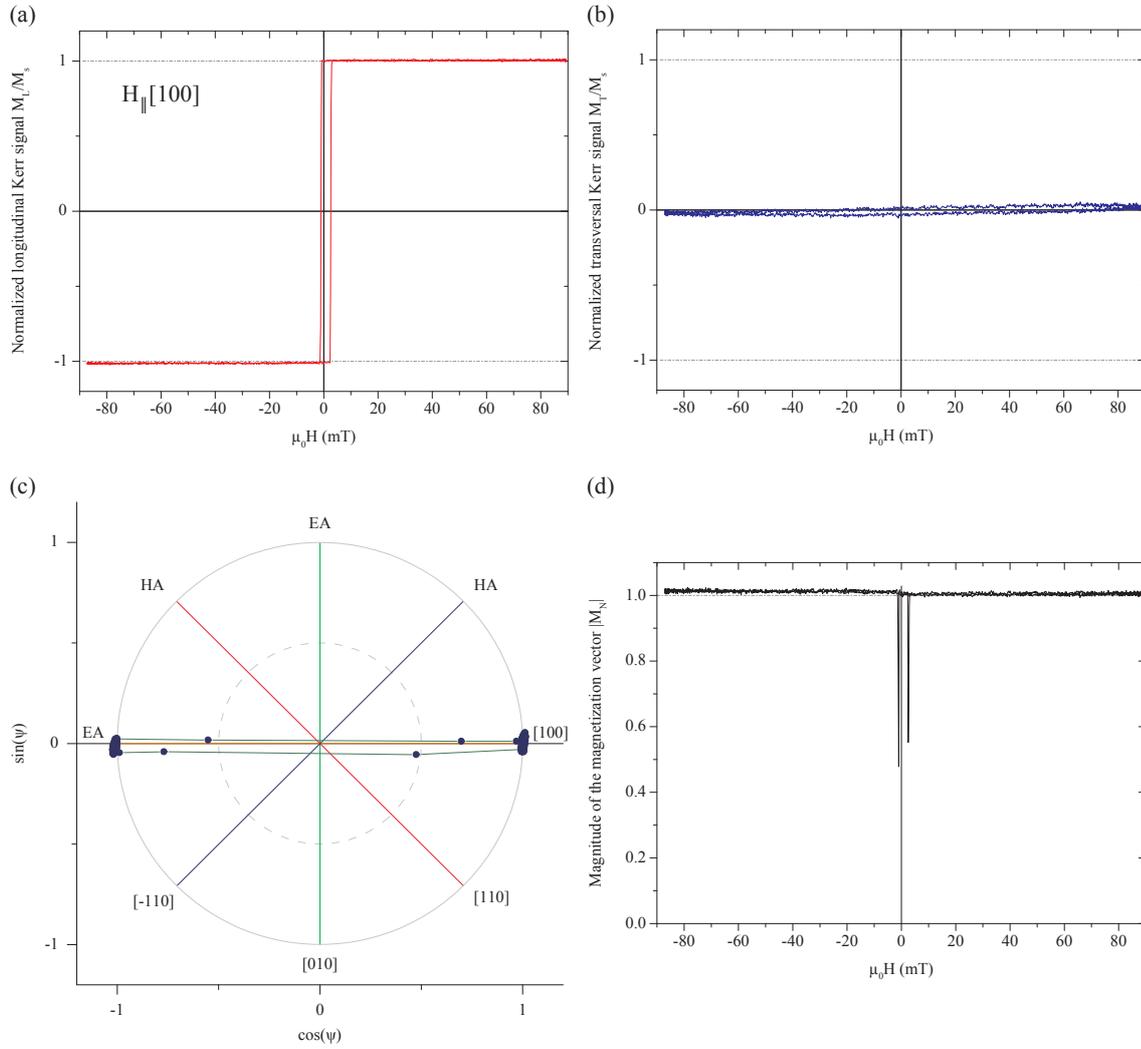
Figure 4.31.: 8 nm-thick iron film: The graphs in (a) and (b) display the normalized longitudinal and transversal Kerr signals versus the external magnetic field applied in the [100] crystal direction, (c) the reversal process of the magnetization vector $\vec{M}_N(\psi)$ as a function of the in-plane rotation angle ψ and (d) the magnitude of the normalized magnetization vector $|\vec{M}_N(\psi)|$ versus the external magnetic field.

8 nm-thick iron film with the external magnetic field along the [100] crystal direction

The data in Figure 4.31 reveal that the [100] crystal direction is a magnetic easy axis of the iron film[159]. The normalized longitudinal Kerr data in Figure 4.31(a) display a

square hysteresis loop with abrupt switching of the magnetization to its saturation value at coercive fields of $-1.1\,\text{mT}$ and $2.6\,\text{mT}$. The normalized transversal Kerr signal in Figure 4.31(b) shows no distinct features.

The polar plot Figure 4.31(c) illustrates the reversal process of the normalized magnetization vector $\vec{M}_N(\psi)$ deduced from the normalized longitudinal and transversal Kerr signals. By sweeping the external magnetic field the vector changes its direction in a straight line along the [100] crystal direction.

The magnitude of the magnetization vector $|\vec{M}_N(\psi)|$ in Figure 4.31(d) is constant between magnetic saturation M_S and magnetic remanence M_R revealing monodomain states. The magnetic remanence is the remaining magnetization if the external magnetic field vanishes. By sweeping the external magnetic field the magnitude decreases indicating a multidomain state as depicted by the two sharp drops between $-0.8\,\text{mT}$ and $-1.6\,\text{mT}$ and $2.3\,\text{mT}$ and $3.1\,\text{mT}$, respectively. At the coercive fields H_C domains exist with anti-parallel magnetization in the [100] and [$\bar{1}$00] crystal directions resulting in a vanishing magnetization vector.

8 nm-thick iron film with the external magnetic field along the [1$\bar{1}$0] crystal direction

The data in Figure 4.32 reveal that the [1$\bar{1}$0] crystal direction is a magnetic hard axis of the iron film relative to the magnetic easy axes in the [100] crystal direction[104, 159]. The normalized longitudinal and transversal Kerr data in Figure 4.32 (a) and (b) show both hysteresis loops. The magnetization switches abruptly at coercive fields of $-0.9\,\text{mT}$ and $2.5\,\text{mT}$ but not to its saturation value. Subsequently, the magnetization increases slowly with increasing external magnetic field till it saturates.

Figure 4.32(c) displays the reversal process of the normalized magnetization vector $\vec{M}_N(\psi)$ deduced from the normalized longitudinal and transversal Kerr signals. The reversal process depicts coherent as well as incoherent rotation of the normalized magnetization vector[104]. Initially, a monodomain state exist in magnetic saturations M_S. By sweeping the external magnetic field the vector first rotates toward one of the magnetic easy axes. Subsequently, the magnetization vector jumps into the other magnetic easy axis. During this jump the magnitude $|\vec{M}_N(\psi)|$ of the vector is reduced between $-1.3\,\text{mT}$ and $-1.8\,\text{mT}$ and $-1.3\,\text{mT}$ and $-0.6\,\text{mT}$ as shown in Figure 4.32(d). This indicates a multidomain state with non-parallel magnetic moments. The individual domains are aligned along the magnetic easy axes to minimize their internal energy. During the jump, the split domains

flip sequentially then from one into the other magnetic easy axis. Further increase of the external magnetic field leads to a second jump into the other magnetic easy axis. Domain splitting occurs again as depicted by the reduced magnitude of the magnetization vector in Figure 4.32(d) between $2.1\,\text{mT}$ and $2.9\,\text{mT}$ and $2.5\,\text{mT}$ and $3.3\,\text{mT}$, respectively. During this jump the magnetic domains are aligned to different magnetic easy axes as during the first jump. Finally, a monodomain state is again created in magnetic saturation in the opposite crystal direction.
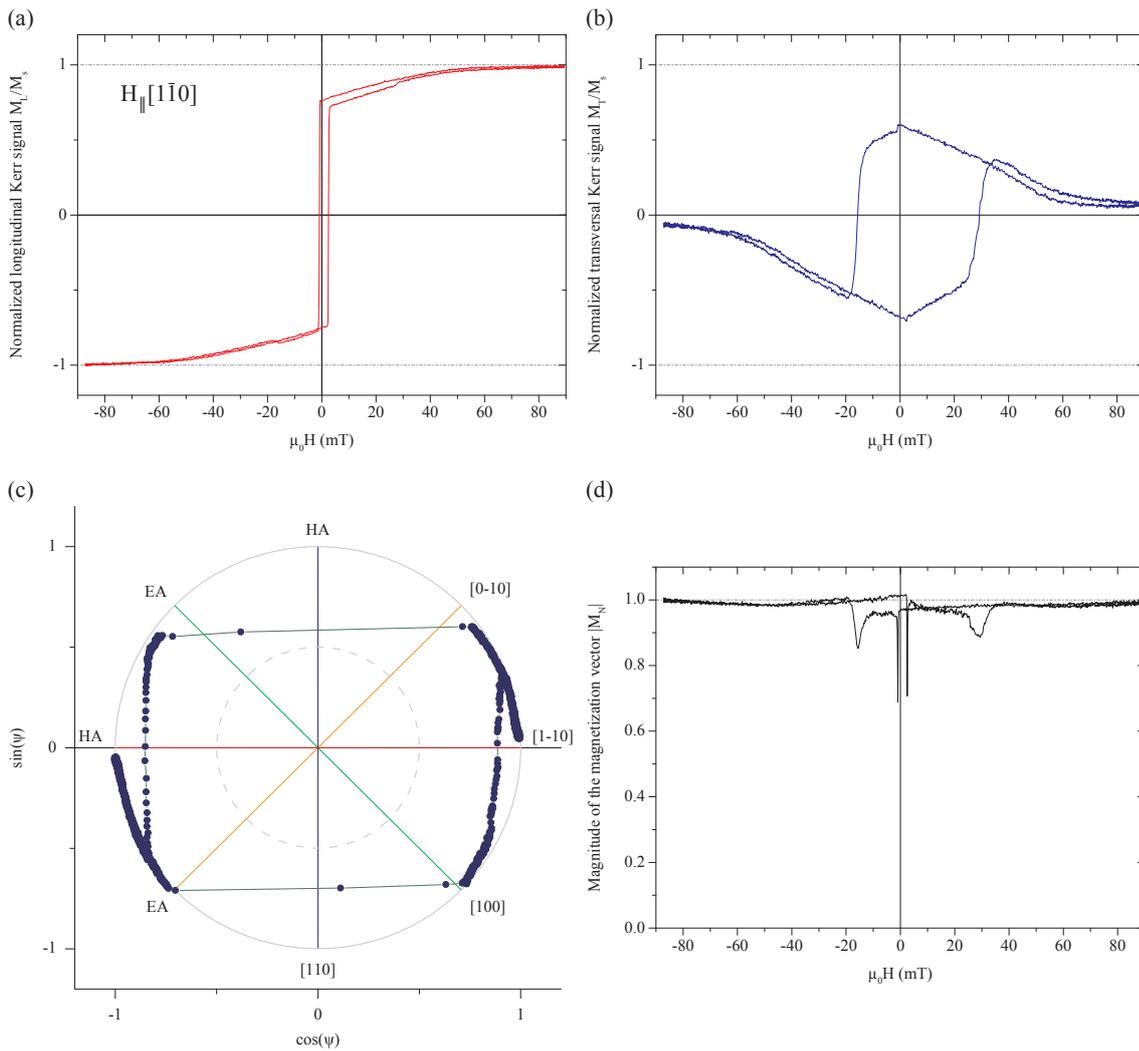
Figure 4.32.: $8\,\text{nm}$-thick iron film: The graphs in (a) and (b) display the normalized longitudinal and transversal Kerr signals versus the external magnetic field applied in the $[1\bar{1}0]$ crystal direction, (c) the reversal process of the magnetization vector $\vec{M}_N(\psi)$ as a function of the in-plane rotation angle ψ and (d) the magnitude of the normalized magnetization vector $|\vec{M}_N(\psi)|$ versus the external magnetic field.
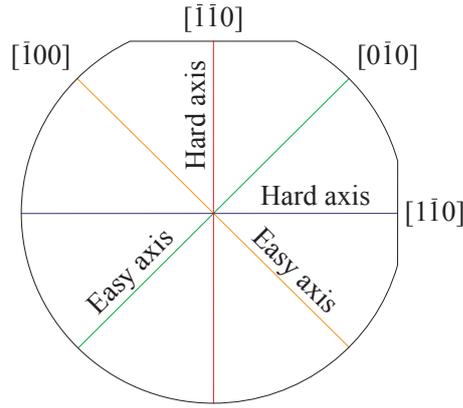
Figure 4.33.: 8 nm-thick iron film: Schematic of the cubic magnetic cubic K_4 of the 8 nm-thick iron film with the crystal orientations of its magnetic axes.

In conclusion, the results of the 8 nm-thick iron film reveal two equivalent magnetic hard axes in the $[\bar{1}\bar{1}0]$ and $[1\bar{1}0]$ crystal directions and two equivalent magnetic easy axes in the $[0\bar{1}0]$ and $[\bar{1}00]$ crystal directions. These magnetic axes can be attributed to the in-plane cubic magnetic anisotropy K_4[159] as shown in Figure 4.33. During magnetic field sweeps, the reversal process revealed an one-jump process when the field was applied along the magnetic easy axes and a two-jump process along the magnetic hard axes.

3.2 nm-thick iron film with the external magnetic field along the $[\bar{1}\bar{1}0]$ crystal direction

The data reveal that the $[\bar{1}\bar{1}0]$ crystal direction is the magnetic easy axis of the iron film[159]. The normalized longitudinal Kerr data in Figure 4.34(a) displays a square hysteresis loop with abrupt switching of the magnetization at coercive fields of -1.1 mT and 2.6 mT. The normalized transversal Kerr signal in Figure 4.34(b) shows no distinct features.

The polar plot in Figure 4.34(c) illustrates the reversal process of the normalized magnetization vector $\vec{M}_N(\psi)$ deduced from the normalized longitudinal and transversal Kerr signals. By sweeping the magnetic field the vector changes its direction in a straight line along the $[\bar{1}\bar{1}0]$ crystal direction.

The magnitude of the magnetization vector $|\vec{M}_N(\psi)|$ in Figure 4.34(d) is constant between saturation M_S and the remanence M_R revealing monodomain states. By sweeping the external magnetic field the magnitude decreases indicating a multidomain state as depicted by the two sharp drops between -0.1 mT and -1.5 mT and 1.6 mT and 3.2 mT, respectively. At the coercive fields H_C domains exist with anti-parallel magnetization in the $[\bar{1}\bar{1}0]$ and $[110]$ crystal directions resulting in a vanishing magnetization vector.
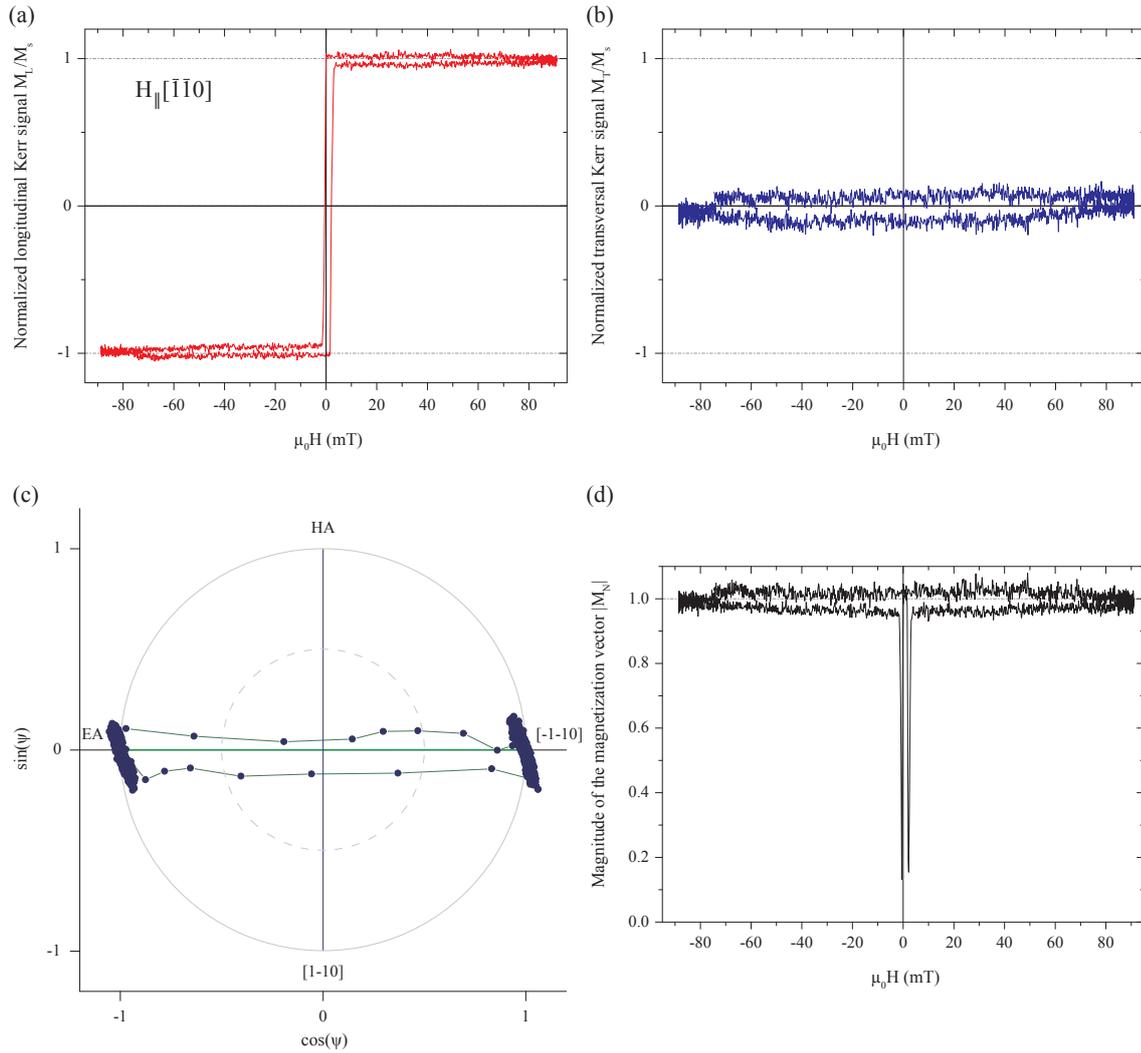
Figure 4.34.: 3.2 nm-thick iron film: The graphs in (a) and (b) display the normalized longitudinal and transversal Kerr signals versus the external magnetic field applied in the $[\bar{1}\bar{1}0]$ crystal direction, (c) the reversal process of the magnetization vector $\vec{M}_N(\psi)$ as a function of the in-plane rotation angle ψ and (d) the magnitude of the normalized magnetization vector $|\vec{M}_N(\psi)|$ versus the external magnetic field.

3.2 nm-thick iron film with the external magnetic field along the $[1\bar{1}0]$ crystal direction

The data reveal that the $[1\bar{1}0]$ crystal direction is the magnetic hard axis of the iron film relative to the magnetic easy axis in the $[\bar{1}\bar{1}0]$ crystal direction[159]. The normalized longitudinal and transversal Kerr data in Figure 4.35(a) and (b) show both hysteresis loops. The magnetization switches at coercive fields of -1.1 mT and 2.1 mT. It increases slowly with increasing external magnetic field till it saturates.

The polar plot in Figure 4.35(c) illustrates the reversal process of the normalized magnetization vector $\vec{M}_N(\psi)$ deduced from the normalized longitudinal and transversal Kerr signals. By sweeping the magnetic field the vector rotates in a circle into the opposite $[\bar{1}10]$ crystal direction. The magnitude of the magnetization vector $|\vec{M}_N(\psi)|$ in Figure 4.34(d) is reduced at around $-40\,\mathrm{mT}$ and shows a drop at $60\,\mathrm{mT}$. The asymmetry of the reduced magnitude around zero external magnetic field might indicate a not perfect alignment of the magnetic axis with the external magnetic field.
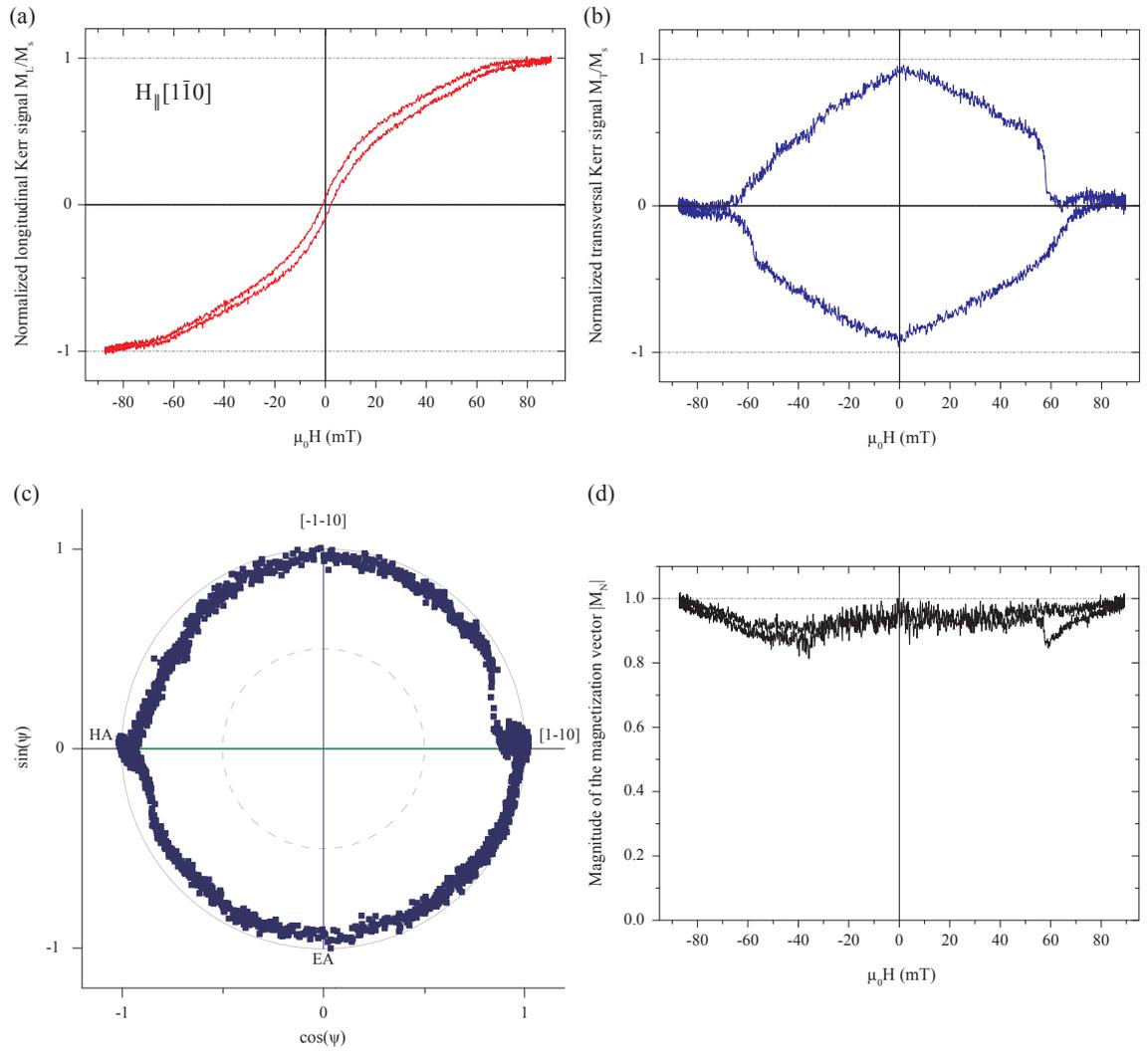
Figure 4.35.: 3.2 nm-thick iron film: The graphs in (a) and (b) display the normalized longitudinal and transversal Kerr signals versus the external magnetic field applied in the $[1\bar{1}0]$ crystal direction, (c) the reversal process of the magnetization vector $\vec{M}_N(\psi)$ as a function of the in-plane rotation angle ψ and (d) the magnitude of the normalized magnetization vector $|\vec{M}_N(\psi)|$ versus the external magnetic field.

The reversal process and magnitude indicates coherent rotation of the magnetization vector. Initially, a monodomain state exist in magnetic saturations M_S. By sweeping the field the vector rotates into the opposite direction of the magnetic hard axis by crossing the film's magnetic easy axis. Thereby, the monodomain state exists throughout the whole rotation of the magnetization vector.
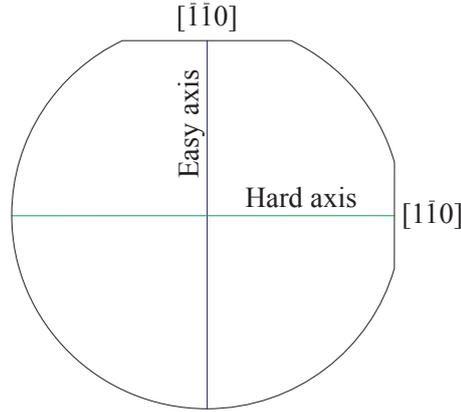
Figure 4.36.: 3.2 nm-thick iron film: Schematic of the cubic magnetic anisotropy K_4 of the 3.2 nm-thick iron film with the crystal orientations of its magnetic axes.

The 3.2 nm-thick iron film reveals a magnetic hard axis in the $[1\bar{1}0]$ crystal direction and a magnetic easy axis in the $[\bar{1}\bar{1}0]$ crystal directions. These magnetic axes can be attributed to the in-plane uniaxial magnetic anisotropy K_U[159] as shown in Figure 4.36.

Thickness dependence of the in-plane magnetic anisotropies

The results from the 8 nm and 3.2 nm-thick iron films reveal that the in-plane magnetic anisotropies depend on the thickness of the iron layer. *MOKE* measurements for different iron thicknesses were performed to investigate this dependency. The anisotropy constants K_U and K_4 for the uniaxial and cubic magnetic anisotropy were deduced from the shape of the hysteresis loops along the magnetic hard axis in the $[1\bar{1}0]$ crystal direction. The analysis method used to extract the anisotropy constants is described in section 3.5.2.

Figure 4.37 displays the dependence of the in-plane uniaxial anisotropy K_U and cubic anisotropy K_4 on the iron layer thickness. The iron thickness gradient was fabricated with an especially designed tantalum mask in the metal *MBE* chamber. Thereby, changes in the anisotropies with the iron layer thickness could be studied systematically from one sample. The thickness gradient was confirmed by four-probe measurements calibrated with *RHEED* oscillations as described in section 3.3. Certain facts may limit the precision
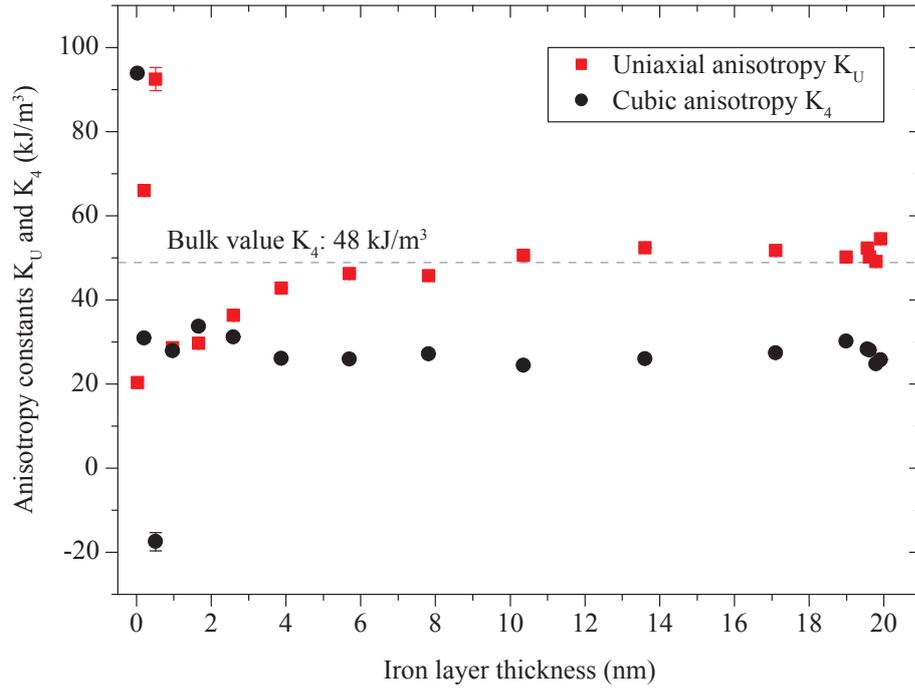
Figure 4.37.: The graph shows the in-plane magnetic anisotropy constants K_U and K_4 deduced from magnetic hard axis hysteresis loops in the $[1\bar{1}0]$ crystal direction. The constants are plotted as functions of the iron layer thickness.

with which the layer thickness was determined along the thickness gradient. This is described at the end of section 3.5.2.

Initially, at low iron coverages of about 0.5 nm, where the *RHEED* intensity shows the drop in the beginning of deposition, impinging iron atoms formed small isolated islands. At this growth state the exchange coupling related to ferromagnetism is limited to the number of iron atoms within these islands. Thus, the small islands probably yielded superparamagnetism or 2D-paramagnetism with Kerr effect signals smaller than the resolution of the used *MOKE* setup. The first Kerr signals were measured at thicknesses ≥ 0.04 nm. This indicates a stronger exchange interaction within the islands or between different islands leading to internal ferromagnetic ordering[124]. Also, intermixing and the formation of compounds at the interface[105] can reduce the magnetic moments at low iron coverages.

At 0.21 nm and 0.51 nm the uniaxial and cubic anisotropy constants in Figure 4.37 do not follow the monotonic behavior of the curves. In these cases the model for $H(M_{L,N})$ in equation 3.10 is not sufficient to describe the more square shaped hysteresis loops.

These hysteresis loops with the corresponding fits are attached in the appendix section A.1.

At iron films thicker than 2.59 nm the cubic anisotropy dominates and converges to the bulk value of iron $K_4 = 48 \, \text{kJ/m}^3$[13]. By decreasing the iron coverage below 2.59 nm the cubic anisotropy decreases and the uniaxial one becomes more significant. Similar behavior of the anisotropies were observed for iron on $In_{0.52}Al_{0.48}As$ hybrid systems[105, 159]. In those studies, a 9 nm-thick $In_{0.52}Al_{0.48}As$ layer was deposited on a 400 nm-thick InGaAs buffer layer fabricated on an InP substrate. The authors observed a purely interfacial origin of the uniaxial anisotropy and suggested an anisotropic bonding at the ferromagnet/semiconductor interface as it has been shown for iron on GaAs hybrid systems[110, 111]. Since the iron on $In_{0.52}Al_{0.48}As$ system has similar material properties than the one on $In_{0.75}Al_{0.25}As$ the anisotropic bonding might also explain the origin of the uniaxial anisotropy in this study.

Iron on modulation-doped GaAs (001) and iron on $In_{0.75}Al_{0.25}As$ revealed analogous behavior of the anisotropy constants for varying iron film thicknesses. However, in the latter case the curves were shifted to lower iron coverages. This might be explained as follows: The in-plane strain of the iron lattice differed on both semiconductor structures for low iron coverages as shown in the section 4.4.1. Also the surfaces exhibited different morphologies. The $In_{0.75}Al_{0.25}As$ revealed a cross-hatch morphology whereby the GaAs was atomically flat. The different strain and surface morphologies of the substrates might led to varying nucleation behavior and island growth at the initial phase of the iron deposition. This can result in different developments of the exchange coupling thus to a shift of the two curves against each other.

The evolution of the Kerr ellipticity signals for varying iron coverages on GaAs (001) and on $In_{0.75}Al_{0.25}As$ is displayed in the appendix section A.3. The data ensure that the tantalum mask had the same position during iron deposition for both samples. Thus, the iron thickness gradient was the same in the cases of iron on GaAs and iron on $In_{0.75}Al_{0.25}As$.

4.4.3. Electrical properties

This section comprises the investigations on the electrical properties of iron films on inverted, modulation-doped InAs heterostructures. The first part focuses on the electrical characteristics of the two-dimensional electron gas (*2DEG*) which is embedded in the inverted, modulation-doped InAs heterostructures at helium temperature. In regard to future spin-valve experiments the electron transport between iron electrodes and $Au_{0.88}Ge_{0.12}$

contacts through the *2DEG* was investigated for various temperatures. The second part contains results on the electrical properties of the iron/In$_x$Al$_{1-x}$As interface for different indium contents x. The modulation-doped In$_x$Al$_{1-x}$As structure contains no *2DEG*.

4.4.3.1. Iron on inverted, modulation-doped InAs heterostructure

During iron deposition the tantalum mask was used to cover the molybdenum block and also outer parts of the wafer as discussed in section 3.3. In this study, sample pieces from these outer parts of the wafer without the deposited iron were used to perform the magneto-transport experiments. Shubnikov-de Haas oscillation and Hall effect measurements were performed at helium temperature to characterize the electron mobility μ and carrier concentration n_s of the embedded *2DEG*[150, 158]. The L-Hallbar structure which is described in section 3.6 was used to measure the Shubnikov-de Haas oscillations and the Quantum Hall effect in two different crystal directions, simultaneously. Further information about the experimental setup and the magneto-transport measurements are supplied in section 3.7.

The following results of the electron mobility and the carrier concentration are the average values obtained from both the Shubnikov-de Haas oscillation and the Hall effect measurements. Without illumination the electron system revealed the carrier concentration and electron mobility of $n_s = 5.64 \cdot 10^{11} \, \text{cm}^{-2}$ and $\mu = 52539 \, \text{cm}^2/\text{Vs}$ in the [110] crystal direction and of $n_s = 5.74 \cdot 10^{11} \, \text{cm}^{-2}$ and $\mu = 59613 \, \text{cm}^2/\text{Vs}$ in the [$\bar{1}$10] crystal direction. By illuminating the structure using an infrared *LED* with a wavelength of $\sim 940 \, \text{nm}$ the carrier concentration and electron mobility increased to $n_s = 8.47 \cdot 10^{11} \, \text{cm}^{-2}$ and $\mu = 59873 \, \text{cm}^2/\text{Vs}$ in the [110] crystal direction and of $n_s = 8.59 \cdot 10^{11} \, \text{cm}^{-2}$ and $\mu = 69130 \, \text{cm}^2/\text{Vs}$ in the [$\bar{1}$10] crystal direction. The results of these magneto-transport measurements ensured the presence of an active *2DEG* system embedded in the InAs heterostructure. The data revealed no parallel conductance.

The temperature-dependent current-voltage characteristics were collected in two-terminal geometry. The voltages were applied between an iron and an Au$_{0.88}$Ge$_{0.12}$ contact. The latter one contacts the InAs channel as sketched in Figure 4.38. The contacts were circle shaped with a diameter of $1 \, \text{mm}$. The applied voltage was varied from $-0.75 \, \text{V}$ to $0.75 \, \text{V}$ in steps of $1 \, \text{mV}$ while measuring the current flowing through the structure. The current-voltage curves were conducted for sample temperatures between $10 \, \text{K}$ and $283 \, \text{K}$ in steps of $5 \, \text{K}$.
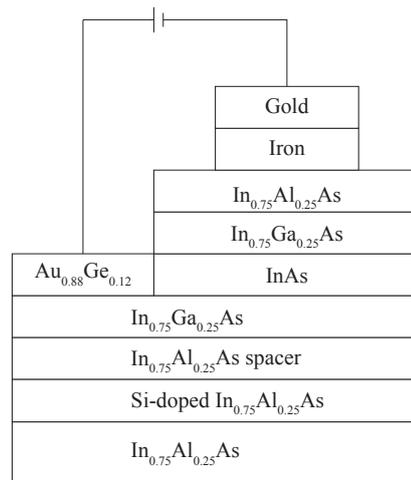
Figure 4.38.: Sketch of the contacted hybrid structure.

The graph in Figure 4.39(a) presents the differential resistance dU/dI multiplied by the total contact area $A = \pi \cdot 0.5^2\,\mathrm{mm}^2$ as a function of the applied voltage. The sample temperatures were varied between $10\,\mathrm{K}$ and $32\,\mathrm{K}$. The curves are asymmetrical for positive and negative voltages. This is probably due to different serial resistances or different electrical active areas at the $Au_{0.88}Ge_{0.12}/InAs$ and iron/$In_{0.75}Al_{0.25}As$ interfaces. Around zero bias the resistance data reveal a peak arising with decreasing temperature indicating Schottky barriers at the interfaces[48, 160]. With increasing applied voltage the differential resistance drops and increases for larger voltages. This is most likely due to electron-electron or electron-impurity scattering events in the *2DEG* channel.
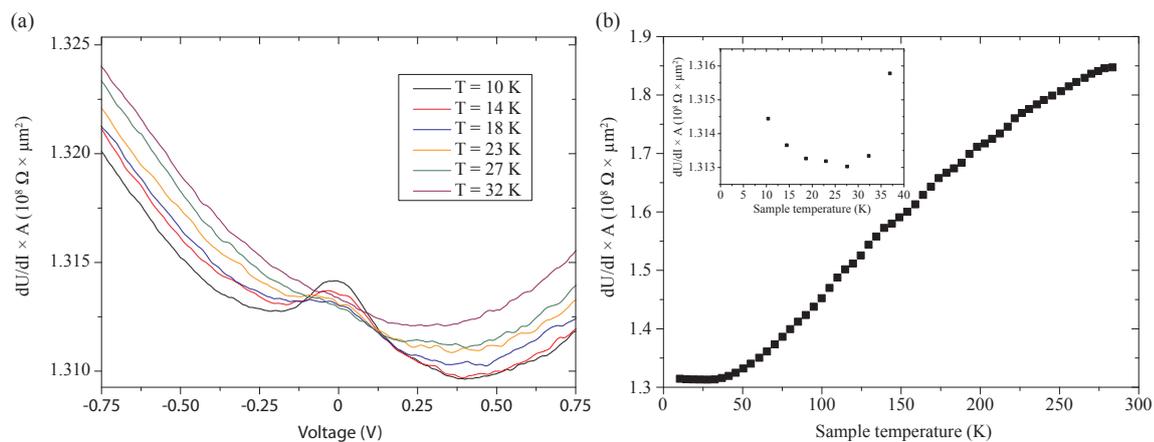
Figure 4.39.: (a) Differential resistance as a function of voltage for various sample temperatures and (b) temperature dependence of the zero-bias resistance.

Figure 4.39(b) shows the zero-bias resistance (ZBR) as a function of temperature. Above $\sim$ 32 K the curve reveals the expected temperature dependence[161]. The increase in resistance below 32 K is probably caused by low Schottky barriers at the $Au_{0.88}Ge_{0.12}$/InAs and iron/$In_{0.75}Al_{0.25}$As interfaces since the barrier heights are expected to be low for higher indium contents[48, 160]. At 10 K the resistance is about 1.7 times smaller than at 283 K. The weak temperature dependence of the ZBR below 32 K is consistent with the third Rowell criterion in section 2.1 indicating that tunneling is the dominant transport mechanism through the barrier.

4.4.3.2. Iron on modulation-doped In_xAl_{1-x}As structures

This section focuses on the electrical properties of the interface between the iron film and the top In_xAl_{1-x}As layer of the modulation-doped InAs heterostructure. Therefore, two iron on modulation-doped In_xAl_{1-x}As hybrid structures were investigated with indium contents of 75 % and 65 %. The layer design of these structures which contain no *2DEG* is shown in Figure 3.7(c). Unfortunately, structures with indium contents of 60 % and 70 % could not be fabricated due to defective III/V-semiconductor *MBE* chambers. The current-voltage characteristics were collected in two-terminal geometry using the closed cycle cryostat and circle structures which are described in section 3.6.

Iron on modulation-doped $In_{0.75}Al_{0.25}$As

In the case of the iron on modulation-doped $In_{0.75}Al_{0.25}$As structure, voltages were applied between two circle shaped iron contacts from -0.5 V to 0.5 V in steps of 1 mV while measuring the current flowing through two similar interfaces. The current-voltage curves were conducted for sample temperatures between 8 K and 289 K in steps of 5 K. Figure 4.40(a) shows the differential resistance dU/dI multiplied by the total contact area $A = \pi \cdot 0.5^2\,mm^2$ as a function of the applied voltage. The sample temperatures was varied between 8 K and 35 K. The inset depicts a sketch of the contacted hybrid structure. The data reveal a small peak in resistance arising around zero bias with decreasing temperature. This indicates Schottky barriers at the iron/$In_{0.75}Al_{0.25}$As interface[48, 160]. The curves are slightly asymmetrical for positive and negative voltages. This asymmetry is probably due to different serial resistances or electrical active areas of the interfaces.

The temperature characteristics of the ZBR curves in Figure 4.40(b) can be explained by different contributions. Probably mainly phonon scattering causes the resistance to decrease as temperature decreases till the curve reaches a minimum around 35 K. At 8 K
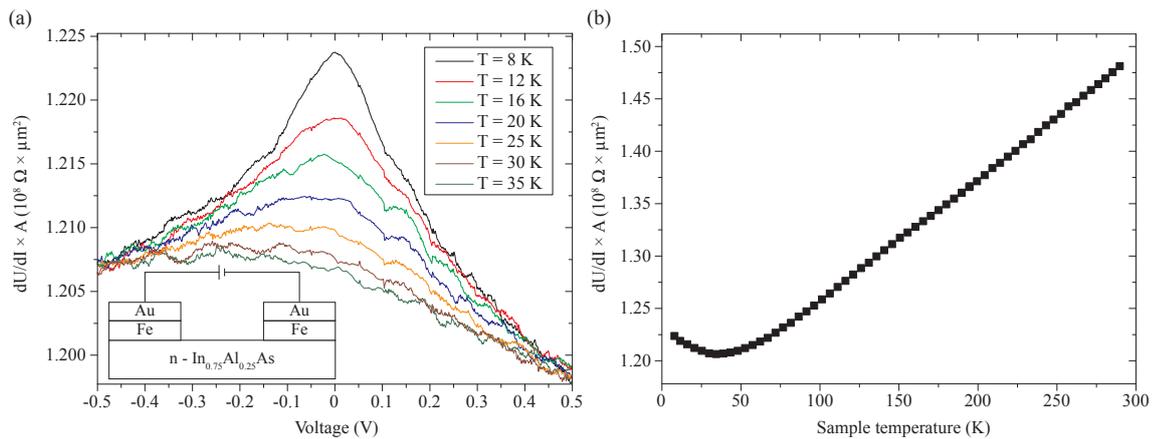
Figure 4.40.: Iron on modulation-doped $In_{0.75}Al_{0.25}As$: (a) differential resistance as a function of the applied voltage for various sample temperatures and a sketch of the contacted hybrid structure and (b) temperature dependence of the zero-bias resistance.

the resistance is about 1.2 times smaller than at 289 K. The increase in resistance below 35 K is most likely caused by low Schottky barriers at the iron/$In_{0.75}Al_{0.25}As$ interface. This is similar to the iron film on modulation-doped InAs heterostructure discussed in the last section. Below 35 K the temperature dependence of the *ZBR* complies with the third Rowell criterion in section 2.1 indicating that tunneling is the dominant transport mechanism through the barrier.

Iron on modulation-doped $In_{0.65}Al_{0.35}As$

The hybrid structure with the indium content of 65 % was investigated by performing current-voltage measurements between a circle shaped iron and a circle shaped $Au_{0.88}Ge_{0.12}$ contact. The latter one contacts the highly-doped $In_{0.65}Al_{0.35}As$ back-gate as shown in Figure 4.41(a) with a *ZBR* of about $6.28 \cdot 10^8 \, \Omega \cdot \mu m^2$ at 8 K. This *ZBR* is about 127 times smaller than the one between the iron film and the low-doped $In_{0.65}Al_{0.35}As$ top layer. Thus, the *ZBR* of the back-gate contact is insignificant compared to the contact resistance at the iron/$In_{0.65}Al_{0.35}As$ interface. The voltage between iron and $Au_{0.88}Ge_{0.12}$ was varied from $-0.5\,V$ to $0.5\,V$ in steps of $1\,mV$ while measuring the current flowing through the structure. The current-voltage curves were conducted for sample temperatures between $8\,K$ and $289\,K$ in steps of $5\,K$.

Figure 4.41(b) shows the current-voltage characteristics for various temperatures between $8\,K$ and $289\,K$. With increasing temperature the shape of the curves changes from the typical diode to a linear ohmic one. This can be attributed to the serial resistance of the structure of about $1.69 \cdot 10^8 \, \Omega \cdot \mu m^2$ which prevails at higher temperatures.
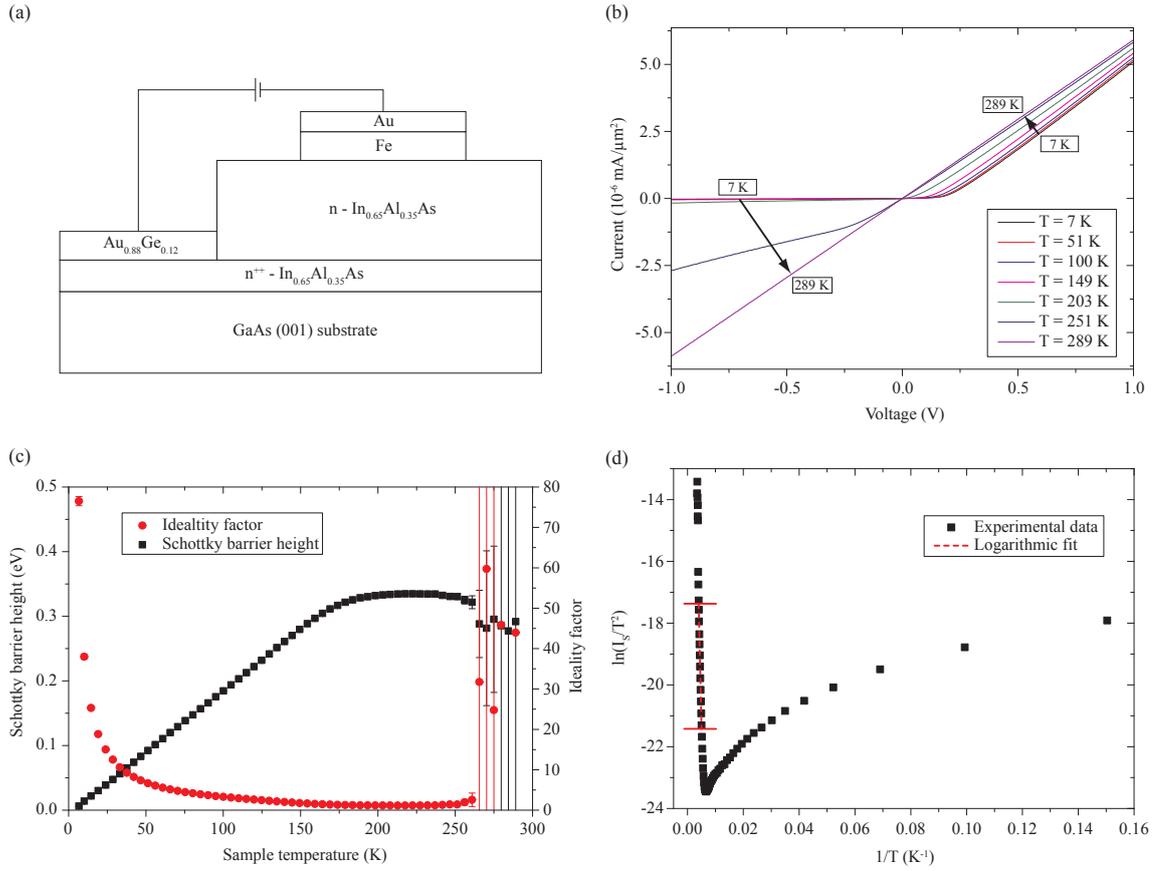
Figure 4.41.: Iron on modulation-doped $In_{0.65}Al_{0.35}As$: (a) Sketch of the contacted hybrid structure, (b) temperature dependence of the current-voltage characteristics, (b) the barrier height and ideality factor versus the sample temperature, (d) Richardson plot and logarithmic fit of the data.

The current-voltage curves were further analyzed by fitting the positive voltage branches as described in section 2.1. The fits yielded the coefficients α and β. Figure 4.41(c) presents the resulting barrier height φ_B and ideality factor n as a function of the sample temperature. The barrier heights were determined with the Richardson constant of $A^* = 9.61\,\mathrm{A/(cm^2\,K^2)}$. The Richardson constant was calculated using equation 2.2 and the effective mass of $m^* = 0.08^{[162]}$. The data show a strong temperature dependence of both the barrier height and the ideality factor. At around $217\,\mathrm{K}$ the ideality is close to unity with $n = 1.14$ and the Schottky barrier has the height of $\varphi_B = 334.7\,\mathrm{meV}$. At temperatures above $\sim 237\,\mathrm{K}$ the parameters exhibit an increasing temperature dependence with large error bars. The temperature dependence of the data reveals that the thermionic-emission theory of Bethe can only be applied in the temperature range between $\sim 210\,\mathrm{K}$ and $\sim 237\,\mathrm{K}$. At temperatures of $T < 210\,\mathrm{K}$ and $T > 237\,\mathrm{K}$ other transport mechanisms can occur like thermionic-field emission, tunneling through the barrier and recombination in

the depletion region due to impurities in the barrier. The strong temperature dependence under reverse bias supports this assumption.

A Richardson plot was constructed to determine the barrier height φ_B and the Richardson constant A^* in the temperature range between $\sim 210\,\mathrm{K}$ and $\sim 237\,\mathrm{K}$. The characteristic parameters φ_B and A^* were obtained from the coefficients of a fit of the $\ln\left(I_0/T^2\right)$ as a function of the inverse of the temperature as described in section 2.1. Figure 4.41(d) shows the Richardson plot and the logarithmic fit of the data. The fit with the quality of $99.64\,\%$ yielded the coefficients $a = -2.22 \pm 0.31$ and $b = -3806.75 \pm 68.59\,\mathrm{K}$ which resulted in the Richardson constant of $A^* = 13.77\,\mathrm{A/(cm^2\,K^2)}$ and the barrier height of $\varphi_B = 328\,\mathrm{meV}$. The Richardson constant obtained from the fit is larger than the above calculated one of $A^* = 9.61\,\mathrm{A/(cm^2\,K^2)}$. This is probably due to different indium contents in the $\mathrm{In}_x\mathrm{Al}_{1-x}\mathrm{As}$ in this study compared to others[162] affecting the effective mass of the electrons. The barrier height of $\varphi_B = 328\,\mathrm{meV}$ seems to be reliable compared to barrier heights of $\mathrm{Au/In}_x\mathrm{Ga}_{1-x}\mathrm{As}$ and $\mathrm{Al/In}_x\mathrm{Ga}_{1-x}\mathrm{As}$ junctions[48, 160].

In conclusion, the results of the iron on modulation-doped $\mathrm{In}_x\mathrm{Al}_{1-x}\mathrm{As}$ hybrid structures revealed that the electrical properties of the iron/$\mathrm{In}_x\mathrm{Al}_{1-x}\mathrm{As}$ interface change with the indium content in the $\mathrm{In}_x\mathrm{Al}_{1-x}\mathrm{As}$ layer. The data indicated that the Schottky barrier at this interface can be tuned by varying the indium content.

5. Conclusions

The conclusions give an overview about the main results of this thesis, followed by an outlook of selected aspects for future developments and experiments.

Summary

The goal of this work was to fabricate and investigate the structural, magnetic as well as electrical properties of the following iron-based III/V-semiconductor hybrid structures: iron on modulation-doped GaAs (001), iron/MgO/modulation-doped GaAs (001) and iron on inverted, modulation-doped InAs heterostructure. The structures were fabricated using regular III/V-semiconductor molecular-beam epitaxy (*MBE*) chambers and two custom-built chambers for the deposition of ferromagnetic metals and insulating MgO films. Thereby, the metal *MBE* chamber was assembled and the MgO *UHV* chamber constructed and assembled within the framework of this thesis. The functionality of the chambers was improved based on data from the deposition processes.

Epitaxial relationships and strain relaxation between the materials of the hybrid systems were investigated using in-situ reflection high-energy electron diffraction (*RHEED*) and ex-situ high-resolution X-ray diffraction (*HRXRD*) techniques.

- The *RHEED* data indicated an epitaxial relationship between iron films and modulation-doped GaAs (001) structures. At low film thicknesses the evolution of the in-plane lattice constant is consistent with the formation of Fe_3GaAs and also indicates the compound Fe_2As. The in-plane compressive misfit strain of $\sim 1.4\%$ is most likely partially relaxed by the formation of these interfacial layers. The iron lattice relaxes probably further by the formation of in-plane misaligned island.

- An epitaxial relationship was observed between iron films and the top $In_{0.75}Al_{0.25}As$ layer of inverted, modulation-doped InAs heterostructures. The evolution of the in-plane lattice constant of iron revealed that the tensile misfit strain of $\sim 3.8\%$ decreases monotonically with increasing iron film thickness. At iron film thicknesses

larger than 5 nm powder-like *RHEED* signals indicated that the strain was most likely released by the formation of in-plane misaligned islands.

- The *RHEED* pattern of MgO films deposited on GaAs indicated an epitaxial relationship to the GaAs lattice with the alignment of four MgO unit cells for every three GaAs unit cells. The data also suggested a polycrystalline structure of the MgO films. Iron films deposited on top of these MgO films revealed an epitaxial relationship as well. Thereby, iron rotated its unit cell against the one of MgO by 45°. The tensile strain of $\sim 0.56\,\%$ was partially released by the formation of islands. Surprisingly, the initial misfit strain component persisted even for iron film thicknesses of up to 50 nm.

Room-temperature magneto-optic Kerr effect (*MOKE*) measurements were performed to investigate the in-plane magnetic properties of the epitaxial iron films.

- The results revealed thickness-dependent uniaxial and cubic anisotropies for iron films on GaAs and $In_{0.75}Al_{0.25}As$ with coercive fields between 1 mT and 2 mT. In the latter case and at iron coverages below 0.5 nm, the data suggested bigger sizes or higher densities of iron islands compared to iron films on GaAs. This might be explained by the difference in misfit strain between iron films deposited on GaAs and on $In_{0.75}Al_{0.25}As$.

- Thickness-independent uniaxial anisotropies were observed for iron films on MgO/modulation-doped GaAs (001) structures. Thereby, the magnetic axes are rotated by 90° compared to the ones of the uniaxial anisotropies of iron films on GaAs and on $In_{0.75}Al_{0.25}As$. The hysteresis loops revealed coercive fields of about 1 mT.

- During the reversal process the magnitude of the magnetization vector revealed monodomain states between magnetic saturation and magnetic remanence if it remained constant. Multidomain states were identified with reduced magnitude of the magnetization vector.

The electrical properties of the hybrid structures were accessed by conducting two-terminal current voltage measurements between macroscopic contacts.

- Schottky barriers form at the iron/highly-doped GaAs interface with low zero-bias resistances (*ZBR*) of about $5.5 \cdot 10^{8}\,\Omega \cdot \mu m^{2}$ at 9 K. Both, the temperature dependence of the *ZBR* and the relative large ideality factor suggested that a combination of thermionic-field emission and tunneling prevails below 142.5 K.

- The iron/MgO/modulation-doped GaAs (001) structures revealed *ZBR* larger than $5\cdot 10^{12}\,\Omega{\cdot}\mu m^2$ for the 6 nm-thick and 4 nm-thick and about $1.25{\cdot}10^{11}\,\Omega{\cdot}\mu m^2$ for the 2 nm-thick MgO film at 10 K. In the latter case, tunneling was identified as the dominant transport mechanism below 128 K. Post-annealing of the hybrid structures probably led to the formation of the interfacial compounds GaO_x and Mg_xAs_y. Current-voltage characteristics revealed that annealing and thus intermixing drastically changes the electrical resistivity of the interfaces.

- Current-voltage characteristics of iron on inverted, modulation-doped InAs heterostructures indicated Schottky barriers at the iron/top $In_{0.75}Al_{0.25}As$ layer interface. Further investigation of iron on modulation-doped $In_{0.75}Al_{0.25}As$ structures revealed Schottky barriers at the metal/semiconductor interface with *ZBR* of about $6\cdot 10^7\,\Omega\cdot\mu m^2$ at 8 K. The *ZBR's* temperature dependence indicated that thermionic-field emission and tunneling are the dominant transport mechanisms below 35 K. A modulation-doped $In_xAl_{1-x}As$ structure with the lower indium content of $x = 0.65$ resulted in a higher barrier of 328 meV with the *ZBR* of about $8\cdot 10^{10}\,\Omega\cdot\mu m^2$ at 8 K. Thereby, thermionic-field emission and tunneling through the barrier increases below 210 K.

The strain relaxation mechanisms of step-graded metamorphic $In_xAl_{1-x}As$ buffers on GaAs (001) substrates with an additional AlAs/GaAs superlattice (*SL*) were investigated using *HRXRD* and atomic force microscopy (*AFM*) techniques.

- The strain between the GaAs and the top $In_{0.75}Al_{0.25}As$ layer is relaxed through the AlAs/GaAs *SL*. Strain is reduced by the activation of dislocation sources at the interfaces of the $In_xAl_{1-x}As$ metamorphic buffer layers.

- Periodic sections are displaced within the metamorphic buffer. This is associated with elastic strain relaxation, which contributes to the reduction of the defect density at the surface.

Magneto-transport and *AFM* measurements were perfomred to investigate the influence of indium content variations in the top $In_xAl_{1-x}As$ metamorphic buffer layer and vicinity of the two-dimensional electron gas on the transport properties and surface morphology of inverted, modulation-doped InAs heterostructures.

- The data revealed correlation between structural and electrical properties. The doping concentration dependence of the electron mobility revealed that remote impurity scattering is the main limiting factor for the electron mobility. Lattice relaxation

within the 4 nm-thick InAs layer, and thus the generation of misfit dislocations, suggested scattering at charged dislocations as the main reason for the reduced electron mobility at low indium contents.

Future prospects

Some of the results obtained in the present study can serve as basis for further investigations and supply relevant information for future spin-injection experiments.

In order to further understand the spin-injection from ferromagnets into semiconductors it is important to investigate ferromagnet/semiconductor interface and identify compounds which can form during the deposition process. In-situ *RHEED* measurements revealed the formation of Fe_3GaAs and Fe_2As interfacial layers at the iron/highly-doped GaAs interface. In the case of iron on $In_{0.75}Al_{0.25}As$, the *RHEED* technique could not access such compounds due to the tensile strained in-plane lattice constant of iron. The Auger spectrometer of the metal *MBE* chamber can be used to investigate in-situ the deposition process of iron and identify possible compounds at the iron/$In_xAl_{1-x}As$ interface.

In this work, it has been shown that domain-splitting can occur during the reversal process of the magnetization vector. It is an important aspect regarding spin-valve experiments. If the rectangle iron stripes of the spin-valve geometry are aligned along magnetic easy axes of the iron films mainly single domains will inject just one spin sort during magnetic field sweeps. But if the electrodes are aligned along magnetic hard axes domain splitting reduces the detection signal's magnitude in local or non-local geometry. Thus, the electrodes should be aligned along magnetic easy axes to achieve distinct spin-valve effects.

The coercive fields of the ferromagnetic films can vary between room and helium temperature. This has been observed for iron films on GaAs (001)[163] where the coercive field increases by a factor of about 30 below 30 K. Temperature-dependent *MOKE* measurements of iron films on $In_{0.75}Al_{0.25}As$ and on MgO/GaAs structures should be considered in order to estimate the in-plane switching fields of the iron electrodes in spin-valve experiments at low temperatures. Another aspect is the shape anisotropy of such ferromagnetic rectangle shaped electrodes. *MOKE* investigations of different sized iron electrodes and varying distances between the electrodes should be performed in order to determine the switching fields related to the shape anisotropy.

Up to the present no results have been reported on all-electrical spin injection and detection experiments of iron/MgO/modulation-doped GaAs (001) systems in local and non-local configuration. In this regard iron/MgO/modulation-doped GaAs (001) hybrid structures with 2 nm-thick MgO films are promising candidates to conduct spin-valve measurements as discussed in section 4.2.3. The results of those investigations could be compared to the ones for example of $Co_{0.50}Fe_{0.50}$ on MgO/n-GaAs structures[164].

Another prospect is all-electrical spin-valve experiments with the iron on inverted, modulation-doped InAs heterostructure hybrid system in the local and non-local configuration. Möller et al. achieved spin injection efficiencies of $\sim 2\%$ from cobalt electrodes into the two-dimensional electron gas of the InAs heterostructure using the cleaved-edge overgrowth technique[165]. In the present work, the iron on InAs heterostructure hybrid structures were fabricated in-vacuo to ensure epitaxial relationships and avoid unintentional oxidization of the iron/$In_{0.75}Al_{0.25}As$ interface. The low iron/$In_{0.75}Al_{0.25}As$ interface resistances, the temperature dependence of the ZBR indicating tunneling and that iron is less reactive on InAs[16] than on GaAs surfaces makes this hybrid structure appealing to achieve spin injection along the vertical (001) crystal direction. Notice that the higher the indium within the top $In_xAl_{1-x}As$ layers of the metamorphic buffer and the $In_xGa_{1-x}As$ layers below and above the InAs region the lower is the density of dislocations in the vicinity of the quantum well region. This reduces electron-impurity scattering and increases the spin lifetime related to the Elliott-Yafet spin relaxation mechanism[57].

Future research might focus on the promising Heusler alloys Fe_3Si[166] and Co_2FeSi[11, 167] which could serve as ferromagnetic electrodes deposited on inverted, modulation-doped InAs heterostructures in all-electrical spin-valve experiments. Advantageously, the Heusler materials have a high degree of spin polarization at the Fermi level[10, 168] and room-temperature ferromagnetism[169, 170]. It might be possible to fabricate thin epitaxial films of these Heusler alloys with less dislocation densities as in the case of iron films on $In_{0.75}Al_{0.25}As$ despite the large tensile misfit strain of $\sim 5.4\%$[166] and $\sim 5.7\%$[171] to the top $In_{0.75}Al_{0.25}As$. The alloys could be fabricated with the metal MBE chamber and the structural properties as epitaxial relationship, lattice phases and stoichiometry investigated with in-situ $RHEED$, AFM, $HRXRD$ and Auger spectroscopy, respectively. But diffusion barriers made out of oxide are needed to avoid intermixing at the interface[50] which might reduce the spin-injection efficiency. These barriers would also allow the formation of the favored L2$_1$ phase at higher deposition temperatures[76] without degenerating the interface by intermixing[41]. Such barriers with controlled thickness can either be fabricated by depositing thin polycrystalline MgO films or oxidizing the semiconductor's surface.

A. Additional magneto-optic Kerr data

A.1. Hysteresis loop fits of iron on $In_{0.75}Al_{0.25}As$ hybrid structure

The graphs in Figure A.1 present branches of the hysteresis loops and the corresponding fits for positive external magnetic fields for different iron layer thicknesses. In the cases of 0.21 nm and 0.51 nm-thick iron films, the model $H(M_{L,N})$ is not sufficient to describe the data.
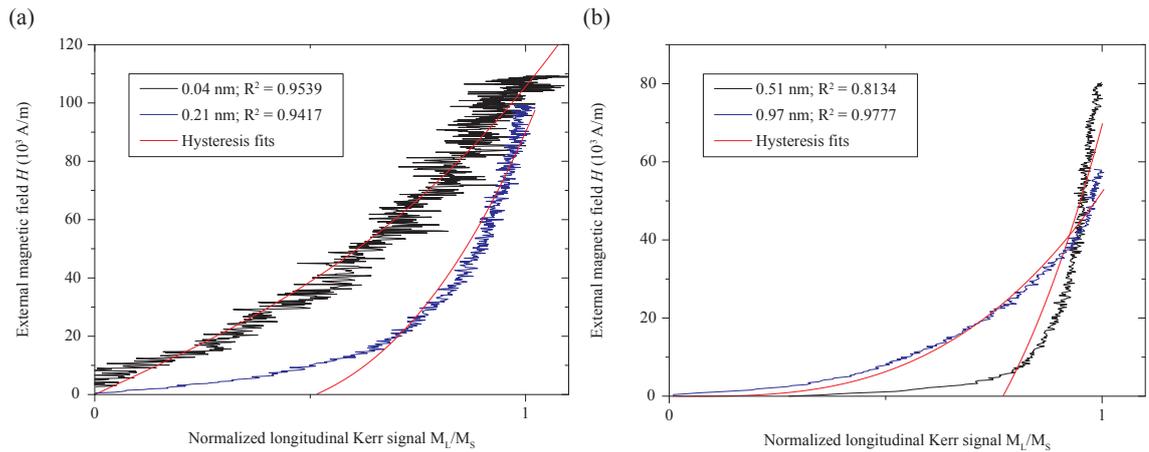
Figure A.1.: Fits of the positive branch of the hysteresis loops at (a) 0.04 nm and 0.21 nm and (b) 0.51 nm and 0.97 nm.

A.2. In-plane magnetic axes of the 8.2 nm-thick iron film on GaAs

The graphs below show the other characteristic magnetic axes of the 8.2 nm-thick iron film on GaAs. The Kerr signals reveal a strong distortion caused by the magnetic offset field which was discussed in section 4.1.2. Figure A.2 displays the normalized (a) longitudinal and (b) transversal Kerr signals and (d) the magnitude of the magnetization vector as

a function of the external magnetic field, respectively. Figure A.2(c) shows the polar plot of the magnetization vector. The external magnetic field was applied along the $[1\bar{1}0]$ crystal direction. The reversal process of the magnetization vector indicates a magnetic hard axis of the iron film relative to the magnetic easy axis in the $[\bar{1}\bar{1}0]$ crystal direction[123].
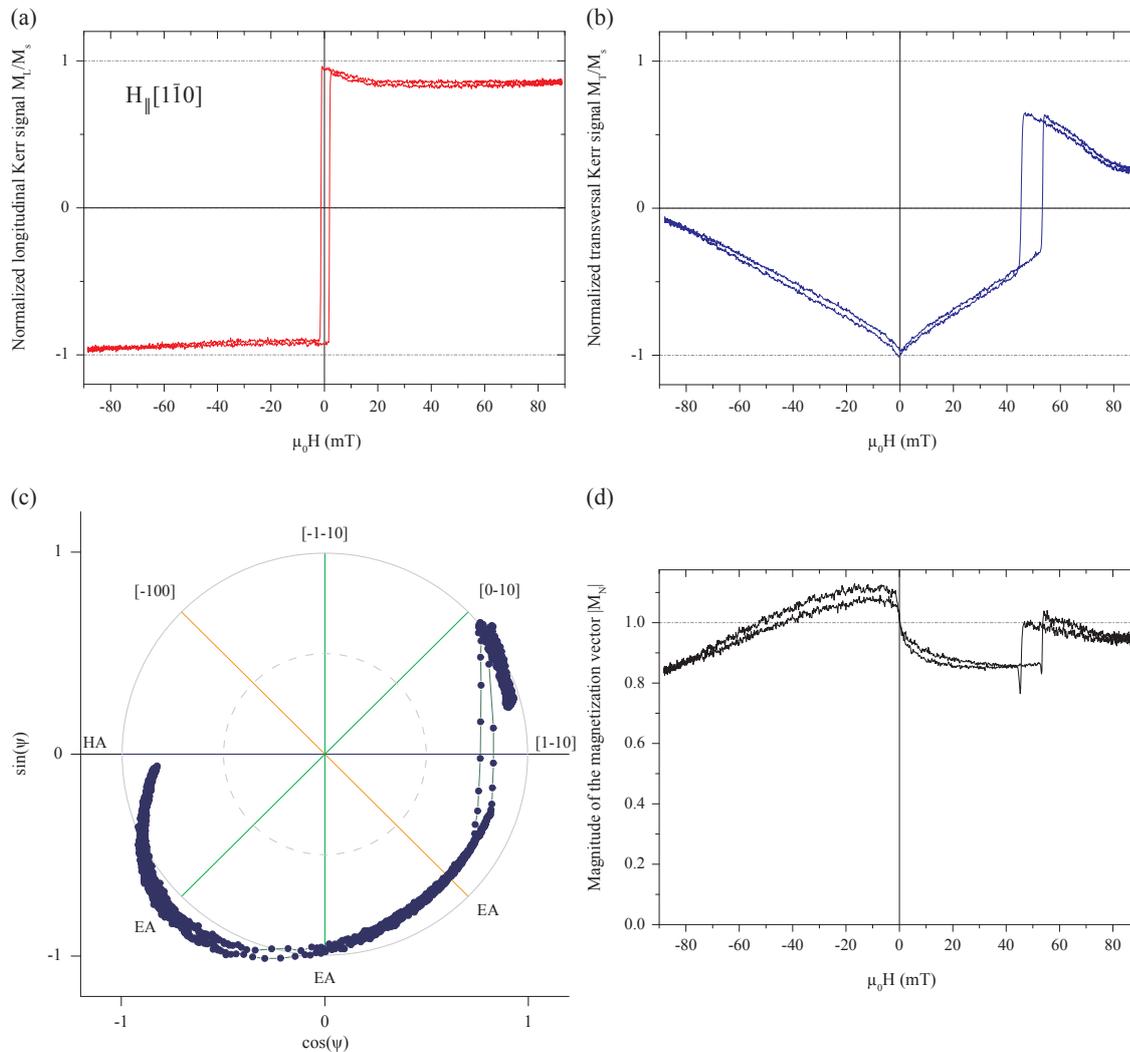
Figure A.2.: 8.2 nm-thick iron film: The graphs in (a) and (b) display the normalized longitudinal and transversal Kerr signals versus the external magnetic field applied in the $[1\bar{1}0]$ crystal direction. The plot in (c) shows the reversal process of the magnetization vector $\vec{M}_N(\psi)$ as a function of the in-plane rotation angle ψ. The graph in (d) presents the magnitude of the normalized magnetization vector $|\vec{M}_N(\psi)|$ versus the external magnetic field.

Figure A.3 presents the normalized (a) longitudinal and (b) transversal Kerr signals and (d) the magnitude of the magnetization vector as a function of the external magnetic field, respectively. Figure A.3(c) shows the polar plot of the magnetization vector. The

external magnetic field was applied in the $[\bar{1}00]$ crystal direction. The reversal process of the vector indicates a magnetic easy axis of the iron film. This easy axis is not as distinct as the easy axis in the $[\bar{1}\bar{1}0]$ crystal direction[123].
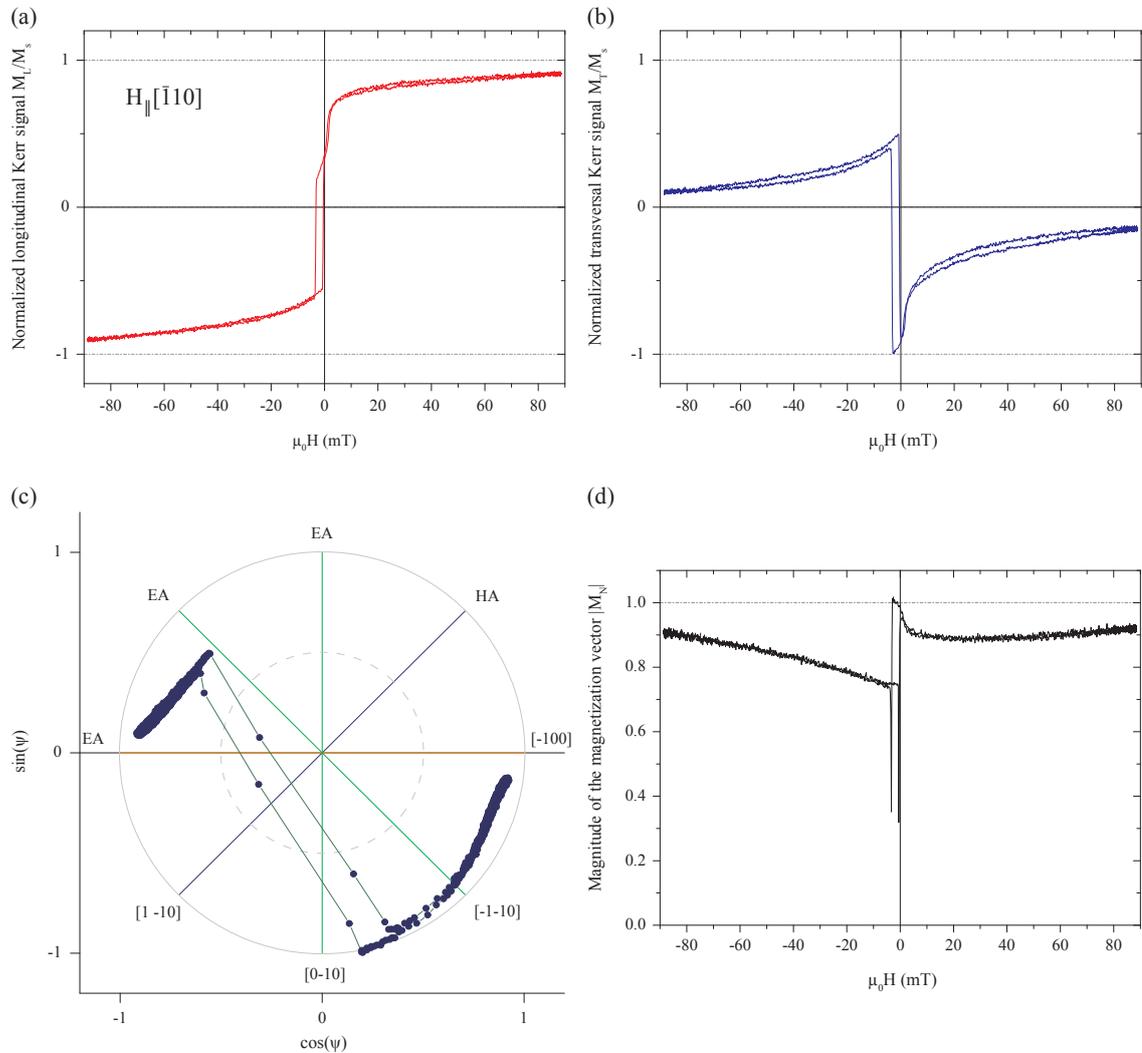
Figure A.3.: 8.2 nm-thick iron film: The graphs in (a) and (b) display the normalized longitudinal and transversal Kerr signals versus the external magnetic field applied in the $[\bar{1}00]$ crystal direction. The plot in (c) shows the reversal process of the magnetization vector $\vec{M}_N(\psi)$ as a function of the in-plane rotation angle ψ. The graph in (d) presents the magnitude of the normalized magnetization vector $|\vec{M}_N(\psi)|$ versus the external magnetic field.

A.3. Kerr ellipticity of iron on GaAs and iron on In$_{0.75}$Al$_{0.25}$As

The signal of the Kerr ellipticity is proportion to the amount of ferromagnetic material thus to the coverage of iron with a certain offset. The Kerr ellipticity signals of iron on GaAs and on In$_{0.75}$Al$_{0.25}$As in Figure A.4 saturate both around $x = 19.5\,\mathrm{mm}$. This wafer position complies with the four-probe measurements of a $20\,\mathrm{nm}$-thick iron film on SiO$_2$ which was shown in Figure 3.12(b) in section 3.3. This confirms that the tantalum mask had the same position during the iron deposition resulting in the same iron coverage along the iron gradient on the GaAs and on the In$_{0.75}$Al$_{0.25}$As substrate. If the position of the tantalum mask would have been shifted or rotated during fabrication of the two hybrid structures the saturation position of the Kerr signals would be shifted against each other.
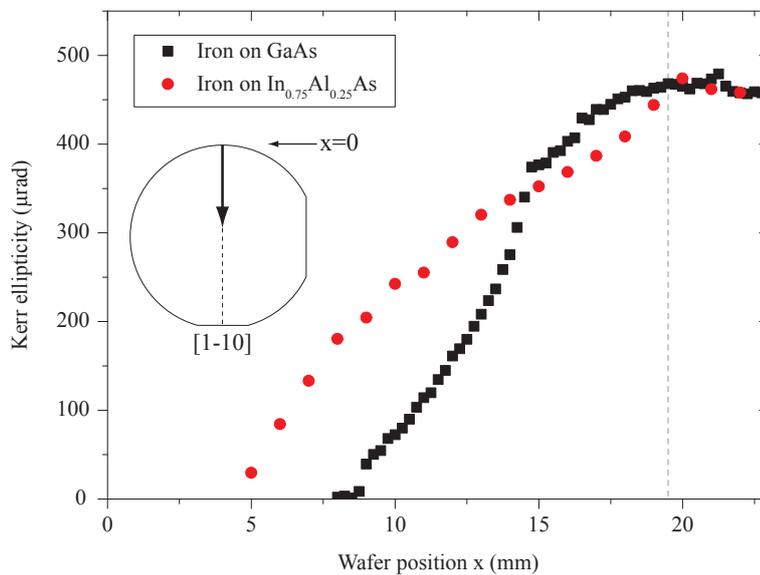
Figure A.4.: Kerr ellipticity of the iron film on GaAs and on In$_{0.75}$Al$_{0.25}$As.

B. Publications

B.1. Publication 1

Title:

Strain relaxation in metamorphic InAlAs buffers

Authors:

B. Landgraf, T. Slobodskyy, Ch. Heyn, and W. Hansen

published in

Materials Science and Engineering: B **177**,762-767 (2012)

included in section 4.3.1

B.2. Publication 2

Title:

Structural and magnetic properties of Ni$_2$MnIn Heusler thin films grown on modulation-doped InAs heterostructures with metamorphic buffer

Authors:

S. Bohse, A. Zolotaryov, A. Volland, B. Landgraf, O. Albrecht, M. Bastjan, T. Vossmeyer, D. Görlitz, Ch. Heyn, and W. Hansen

not included in this thesis

C. Conference contributions

- B. Landgraf, S. Bohse, Ch. Heyn, and W. Hansen.
  Molecular beam epitaxy of Heusler alloys on InAs heterostructures
  Workshop of the Graduiertenkolleg 1286 „Functional Metal-Semiconductor Hybrid Systems".
  Jever, Germany (2010)

- B. Landgraf, S. Bohse, Ch. Heyn, and W. Hansen.
  Molecular beam epitaxy of Heusler alloys on InAs heterostructures
  Frühjahrstagung der Deutschen Physikalischen Gesellschaft.
  Dresden, Germany (2011)

- B. Landgraf, Ch. Heyn, and W. Hansen.
  Indium content dependence of carrier mobility in modulation-doped InAs heterostructures
  Deutscher *MBE* workshop.
  Berlin, Germany (2011)

- B. Landgraf, Ch. Heyn, and W. Hansen.
  Indium content dependence of carrier mobility in modulation-doped InAs heterostructures
  Workshop of the Graduiertenkolleg 1286 „Functional Metal-Semiconductor Hybrid Systems".
  Lübeck, Germany (2011)

- B. Landgraf, T. Slobodskyy, Ch. Heyn, and W. Hansen.
  Strain relaxation in metamorphic InAlAs buffers
  Frühjahrstagung der Deutschen Physikalischen Gesellschaft.
  Berlin, Germany (2012)

- T. Nickel, B. Landgraf, T. Slobodskyy, and W. Hansen.
  Growth and Analysis of FeCo on GaAs
  Frühjahrstagung der Deutschen Physikalischen Gesellschaft.
  Berlin, Germany (2012)

- B. Landgraf, T. Slobodskyy, Ch. Heyn, and W. Hansen.
  Structural properties of iron on modulation-doped (001) *GaAs and modulation-doped InAs heterostructures*
  Workshop of the Graduiertenkolleg 1286 „Functional Metal-Semiconductor Hybrid Systems".
  Stade, Germany (2012)

- B. Landgraf, T. Slobodskyy, Ch. Heyn, and W. Hansen.
  Structural properties of iron on modulation-doped (001) *GaAs and modulation-doped InAs heterostructures*
  Frühjahrstagung der Deutschen Physikalischen Gesellschaft.
  Regensburg, Germany (2013)

- T. Slobodskyy, A. Slobodskyy, B. Landgraf, Ch. Heyn, and W. Hansen.
  3D reciprocal space imaging of individual Cu(In,Ga)Se$_2$ nanocrystallites inside a thin film solar cell
  Frühjahrstagung der Deutschen Physikalischen Gesellschaft.
  Regensburg, Germany (2013)

- T. Slobodskyy, B. Landgraf, G. Schneider, Ch. Heyn, and W. Hansen.
  Iron films grown on virtual substrates with metamorphic InAlAs buffers
  VI international seminar and school about modern methods of diffraction data analysis and x-ray optics.
  St. Petersburg, Russia (2013)

List of Figures

Bibliography

[1] I. Žutić, J. Fabian, and S.D. Sarma. Spintronics: Fundamentals and applications. *Reviews of modern physics*, 76(2):323, 2004.

[2] S.D. Bader and S.S.P. Parkin. Spintronics. *Annu. Rev. Condens. Matter Phys.*, 1:71–88, 2010.

[3] G.X. Miao, M. Münzenberg, and J.S. Moodera. Spin dynamics in semiconductors. *Reports on Progress in Physics*, 74:036501, 2011.

[4] M.W. Wu, J.H. Jiang, and M.Q. Weng. Spin dynamics in semiconductors. *Physics Reports*, 493:61–236, 2010.

[5] T. Benter, H. Lehmann, T. Matsuyama, W. Hansen, C. Heyn, U. Merkt, and J. Jacob. Quantized conductance and evidence for zitterbewegung in InAs spin filters. *Applied Physics Letters*, 102:212405–212405, 2013.

[6] A. Kawaharazuka, M. Ramsteiner, J. Herfort, H.-P. Schonherr, H. Kostial, and K.H. Ploog. Spin injection from Fe$_3$Si into GaAs. *Applied Physics Letters*, 85(16):3492–3494, 2004.

[7] S. Jahangir, F. Doğan, H. Kum, A. Manchon, and P. Bhattacharya. Spin diffusion in bulk GaN measured with MnAs spin injector. *Physical Review B*, 86(3):035315, 2012.

[8] K.-R. Jeon, B.-C. Min, I.-J. Shin, C.-Y. Park, H.-S. Lee, Y.-H. Jo, and S.-C. Shin. Electrical spin accumulation with improved bias voltage dependence in a crystalline CoFe/MgO/Si system. *Applied Physics Letters*, 98(26):262102–262102, 2011.

[9] C.H. Li, G. Kioseoglou, O.M.J. van't Erve, P.E. Thompson, and B.T. Jonker. Electrical spin injection into Si (001) through a SiO$_2$ tunnel barrier. *Applied Physics Letters*, 95(17):172102–172102, 2009.

[10] M. Ramsteiner, O. Brandt, T. Flissikowski, H.T. Grahn, M. Hashimoto, J. Herfort, and H. Kostial. Co$_2$FeSi/GaAs/(Al, Ga) As spin light-emitting diodes: Com-

petition between spin injection and ultrafast spin alignment. *Physical Review B*, 78(12):121303, 2008.

[11] P. Bruski, Y. Manzke, R. Farshchi, O. Brandt, J. Herfort, and M. Ramsteiner. All-electrical spin injection and detection in the Co_2FeSi/GaAs hybrid system in the local and non-local configuration. *Applied Physics Letters*, 103(5).

[12] T. Matsuyama, C.-M. Hu, D. Grundler, G. Meier, and U. Merkt. Ballistic spin transport and spin interference in ferromagnet/InAs (2DES)/ferromagnet devices. *Physical Review B*, 65(15):155322, 2002.

[13] G. Wastlbauer and J.A.C. Bland*. Structural and magnetic properties of ultrathin epitaxial Fe films on GaAs (001) and related semiconductor substrates. *Advances in physics*, 54(2):137–219, 2005.

[14] Y.B. Xu, E.T.M. Kernohan, M. Tselepi, J.A.C. Bland, and S. Holmes. Single crystal Fe films grown on InAs (100) by molecular beam epitaxy. *Applied physics letters*, 73(3):399–401, 1998.

[15] W.M. Haynes, D.R. Lide, and T.J. Bruno. *CRC Handbook of Chemistry and Physics 2012-2013*. CRC press, 2012.

[16] C.M. Teodorescu, F. Chevrier, R. Brochier, C. Richter, O. Heckmann, V. Ilakovac, P. De Padova, and K. Hricovini. X-ray magnetic circular dichroism, photoemission and rheed studies of Fe/InAs (100) interfaces. *Surface science*, 482:1004–1009, 2001.

[17] A. Filipe, A. Schuhl, and P. Galtier. Structure and magnetism of the Fe/GaAs interface. *Applied physics letters*, 70(1):129–131, 1997.

[18] X. Lou, Ch. Adelmann, S.A. Crooker, E.S. Garlid, J. Zhang, K.S.M. Reddy, S.D. Flexner, C.J. Palmstrøm, and P.A. Crowell. Electrical detection of spin transport in lateral ferromagnet–semiconductor devices. *Nature Physics*, 3(3):197–202, 2007.

[19] X. Lou. Electrical detection of spin transport in ferromagnet-semiconductor heterostructures. *arXiv preprint cond-mat/0701021*, 2007.

[20] R.I. Dzhioev, K.V. Kavokin, V.L. Korenev, M.V. Lazarev, B.Y. Meltser, M.N. Stepanova, B.P. Zakharchenya, D. Gammon, and D.S. Katzer. Low-temperature spin relaxation in n-type GaAs. *Physical Review B*, 66(24):245204, 2002.

[21] S. Datta and B. Das. Electronic analog of the electro-optic modulator. *Applied Physics Letters*, 56:665, 1990.

[22] A.W. Cummings, R. Akis, D.K. Ferry, J. Jacob, T. Matsuyama, U. Merkt, and G. Meier. Cascade of Y-shaped spin filters in InGaAs/InAs/InGaAs quantum wells. *Journal of Applied Physics*, 104(6):066106–066106, 2008.

[23] S. Löhr, Ch. Heyn, and W. Hansen. Nonplanar two-dimensional electron gases in InAs heterostructures on GaAs. *Applied physics letters*, 84(4):550–552, 2004.

[24] J. Nitta, T. Akazaki, H. Takayanagi, and T. Enoki. Gate control of spin–orbit interaction in an InAs-inserted $In_{0.53}Ga_{0.47}As/In_{0.52}Al_{0.48}As$ heterostructure. *Physica E: Low-dimensional Systems and Nanostructures*, 2(1):527–531, 1998.

[25] H. Wenzel, P. Crump, A. Pietrzak, X. Wang, G. Erbert, and G. Tränkle. Theoretical and experimental investigations of the limits to the maximum output power of laser diodes. *New Journal of Physics*, 12(8):085007, 2010.

[26] I. Dhifallah, M. Daoudi, A. Bardaoui, N. Sedrine, S. Aloulou, A. Ouerghli, and R. Chtourou. Photoluminescence studies of 2DEG confinement in InAs ultrathin layer introduced in GaAs/AlGaAs structure. *Physica E: Low-dimensional Systems and Nanostructures*, 42(8):2134–2138, 2010.

[27] I. Dhifallah, M. Daoudi, A. Bardaoui, B. Eljani, A. Ouerghi, and R. Chtourou. Photoreflectance study of InAs ultrathin layer embedded in Si-delta-doped GaAs/AlGaAs quantum wells. *Journal of Luminescence*, 131(5):1007–1012, 2011.

[28] I. Dhifallah, M. Daoudi, A. Ouerghli, M. Oueslati, and R. Chtourou. Silicon doping effects on optical properties of InAs ultrathin layer embedded in GaAs/AlGaAs: δSi high electron mobility transistors structures. *Superlattices and Microstructures*, 49(5):519–526, 2011.

[29] K. Wang, Y.-G. Zhang, Y. Gu, Ch. Li, H.S.B.Y. Li, Y.-Y. Li, et al. Iimproving the performance of extended wavelength InGaAs photodetectors by using digital graded heterointerfacessuperlattice. *Journal of Infrared and Millimeter Waves*, 6:002, 2009.

[30] S. Löhr, S. Mendach, T. Vonau, Ch. Heyn, and W. Hansen. Highly anisotropic electron transport in shallow InGaAs heterostructures. *Physical Review B*, 67(4):045309, 2003.

[31] T. Sasaki, H. Suzuki, A. Sai, J.-H. Lee, M. Takahasi, S. Fujikawa, K. Arafune, I. Kamiya, Y. Ohshita, and M. Yamaguchi. In situ real-time x-ray reciprocal space mapping during InGaAs/GaAs growth for understanding strain relaxation mechanisms. *Applied physics express*, 2(8):5501, 2009.

[32] H. Suzuki, T. Sasaki, A. Sai, Y. Ohshita, I. Kamiya, M. Yamaguchi, M. Takahasi, and S. Fujikawa. Real-time observation of anisotropic strain relaxation by three-dimensional reciprocal space mapping during InGaAs/GaAs (001) growth. *Applied Physics Letters*, 97(4):041906–041906, 2010.

[33] Y. Cordier, D. Ferre, J.M. Chauveau, and J. Dipersio. Surface morphology and strain relaxation of InAlAs buffer layers grown lattice mismatched on GaAs with inverse steps. *Applied surface science*, 166(1):442–445, 2000.

[34] Z. Jiang, W. Wang, H. Gao, L. Liu, H. Chen, and J. Zhou. Strain relaxation and surface morphology of high indium content InAlAs metamorphic buffers with reverse step. *Applied Surface Science*, 254(16):5241–5246, 2008.

[35] A. Sayari, N. Yahyaoui, A. Meftah, A. Sfaxi, and M. Oueslati. Residual strain and alloying effects on the vibrational properties of step-graded $In_xAl_{1-x}As$ layers grown on GaAs. *Journal of Luminescence*, 129(2):105–109, 2009.

[36] D. Lee, M.S. Park, Z. Tang, H. Luo, R. Beresford, and C.R. Wie. Characterization of metamorphic InAlAs/GaAs buffer layers using reciprocal space mapping. *Journal of applied physics*, 101:063523, 2007.

[37] S. Mendach, C.M. Hu, Ch. Heyn, S. Schnüll, H.P. Oepen, R. Anton, and w. Hansen. Strain relaxation in high-mobility InAs inserted-channel heterostructures with metamorphic buffer. *Physica E: Low-dimensional Systems and Nanostructures*, 13(2):1204–1207, 2002.

[38] Ch. Heyn, S. Mendach, S. Löhr, S. Beyer, S. Schnüll, and W. Hansen. Growth of shallow InAs hemts with metamorphic buffer. *Journal of crystal growth*, 251(1):832–836, 2003.

[39] H.C. Koo, H. Yi, J.-B. Ko, J. Chang, S.-H. Han, D. Jung, S.-G. Huh, and J. Eom. Electrical spin injection and detection in an InAs quantum well. *Applied physics letters*, 90(2):022101–022101, 2007.

[40] H.C. Koo, J.H. Kwon, J. Eom, J. Chang, S.H. Han, and M. Johnson. Control of spin precession in a spin-injected field effect transistor. *Science*, 325(5947):1515–1518, 2009.

[41] S. Bohse, A. Zolotaryov, W. Kreuzpaintner, D. Lott, A. Kornowski, A. Stemmann, Ch. Heyn, and W. Hansen. Suppression of interfacial intermixing between MBE-grown heusler alloy Ni_2MnIn and (001) InAs or InAs-HEMT structures. *Journal of Crystal Growth*, 323(1):368–371, 2011.

[42] S. Bohse, A. Zolotaryov, A. Volland, B. Landgraf, O. Albrecht, M. Bastjan, T. Voss-meyer, D. Görlitz, Ch. Heyn, and W. Hansen. Structural and magnetic properties of Ni_2MnIn heusler thin films grown on modulation-doped InAs heterostructures with metamorphic buffer. *Journal of Crystal Growth*, 338(1):91–95, 2012.

[43] G. Schmidt, D. Ferrand, L.W. Molenkamp, A.T. Filip, and B.J. Van Wees. Funda-mental obstacle for electrical spin injection from a ferromagnetic metal into a diffusive semiconductor. *Physical Review B*, 62(8):R4790–R4793, 2000.

[44] E.I. Rashba. Theory of electrical spin injection: Tunnel contacts as a solution of the conductivity mismatch problem. *Physical Review B*, 62(24):R16267–R16270, 2000.

[45] H. Kurebayashi, S.J. Steinmuller, J.B. Laloe, T. Trypiniotis, S. Easton, A. Ionescu, J.R. Yates, and J.A.C. Bland. Initial/final state selection of the spin polarization in electron tunneling across an epitaxial Fe/GaAs(001) interface. *Applied Physics Letters*, 91(10):102114–102114, 2007.

[46] B.T. Jonker, E.M. Kneedler, P. Thibado, O.J. Glembocki, L.J. Whitman, and B.R. Bennett. Schottky barrier formation for Fe on GaAs (001) and the role of interfacial structure. *Journal of Applied Physics*, 81(8):4362–4362, 1997.

[47] C. Adelmann, J.Q. Xie, C.J. Palmstrøm, J. Strand, X. Lou, J. Wang, and P.A. Crowell. Effects of doping profile and post-growth annealing on spin injection from Fe into (Al, Ga) As heterostructures. *Journal of Vacuum Science & Technology B: Microelectronics and Nanometer Structures*, 23(4):1747–1751, 2005.

[48] K. Kajiyama, Y. Mizushima, and S. Sakata. Schottky barrier height of n-InGaAs diodes. *Applied Physics Letters*, 23:458, 1973.

[49] C. Marinelli, L. Sorba, M. Lazzarino, D. Kumar, E. Pelucchi, B.H. Muller, D. Orani, S. Rubini, A. Franciosi, S. De Franceschi, et al. Tunable schottky barrier contacts to $In_xGa_{1-x}As$. *Journal of Vacuum Science & Technology B: Microelectronics and Nanometer Structures*, 18(4):2119–2127, 2000.

[50] C. Martınez Boubeta, E. Navarro, A. Cebollada, F. Briones, F. Peiró, and A. Cor-net. Epitaxial Fe/MgO heterostructures on GaAs (001). *Journal of crystal growth*, 226(2):223–230, 2001.

[51] K. Yoh, H. Ohno, K. Sueoka, and M.E. Ramsteiner. Reduced interface reaction during the epitaxial Fe growth on InAs for high efficiency spin injection. *Journal of Vacuum Science & Technology B: Microelectronics and Nanometer Structures*, 22(3):1432–1435, 2004.

[52] D.O. Demchenko and A.Y. Liu. Influence of interface structure on electronic properties and schottky barriers in Fe/GaAs magnetic junctions. *Physical Review B*, 73(11):115332, 2006.

[53] J.M. Teixeira, J. Ventura, J.P. Araujo, J.B. Sousa, P. Wisniowski, and P.P. Freitas. Tunneling processes in thin MgO magnetic junctions. *Applied Physics Letters*, 96(26):262506–262506, 2010.

[54] B.J. Jonsson-Akerman, R. Escudero, C. Leighton, S. Kim, I.K. Schuller, and D.A. Rabson. Reliability of normal-state current–voltage characteristics as an indicator of tunnel-junction barrier quality. *Applied Physics Letters*, 77(12):1870–1872, 2000.

[55] J. Thingna and J.-S. Wang. Geometrical effects on spin injection: 3D spin drift diffusion model. *Journal of Applied Physics*, 109(12):124303–124303, 2011.

[56] G.X. Miao, Y.J. Park, J.S. Moodera, M. Seibt, G. Eilers, and M. Münzenberg. Disturbance of tunneling coherence by oxygen vacancy in epitaxial Fe/MgO/Fe magnetic tunnel junctions. *Physical review letters*, 100(24):246803, 2008.

[57] E. Tsymbal, Y. Evgeny, and I. Žutić. *Handbook of spin transport and magnetism.* CRC Press, 2012.

[58] R.M. Stroud, A.T. Hanbicki, Y.D. Park, G. Kioseoglou, A.G. Petukhov, B.T. Jonker, G. Itskos, and A. Petrou. Reduction of spin injection efficiency by interface defect spin scattering in ZnMnSe/AlGaAs-GaAs spin-polarized light-emitting diodes. *Physical review letters*, 89(16):166602, 2002.

[59] S.M. Sze and K.K. Ng. *Physics of semiconductor devices.* Wiley. com, 2006.

[60] H. Ibach and H. Lüth. *Festkörperphysik: eine Einführung in die Grundlagen*, volume 4. Springer, 1990.

[61] H.A. Bethe. *Theory of the Boundary Layer of Crystal Rectifiers*, volume 43 of *Report (Massachusetts Institute of Technology. Radiation Laboratory).* Radiation Laboratory, Massachusetts Institute of Technology, 1942.

[62] M. Cardona. Electron effective masses of InAs and GaAs as a function of temperature and doping. *Physical Review*, 121(3):752, 1961.

[63] W.G. Spitzer and J.M. Whelan. Infrared absorption and electron effective mass in n-type gallium arsenide. *Physical Review*, 114(1):59, 1959.

[64] A. Raymond, J.L. Robert, and C. Bernard. The electron effective mass in heavily doped gaas. *Journal of Physics C: Solid State Physics*, 12(12):2289, 1979.

[65] I. Strzalkowski, S. Joshi, and C.R. Crowell. Dielectric constant and its temperature dependence for GaAs, CdTe, and ZnSe. *Applied Physics Letters*, 28(6):350–352, 1976.

[66] E. Burstein and S. Lundqvist. *Tunneling phenomena in solids.* Plenum Press New York, 1969.

[67] A.T. Hanbicki, O.M.J. van't Erve, R. Magno, G. Kioseoglou, C.H. Li, B.T. Jonker, G. Itskos, R. Mallory, M. Yasar, and A. Petrou. Analysis of the transport process providing spin injection through an Fe/AlGaAs schottky barrier. *Applied Physics Letters*, 82(23):4092–4094, 2003.

[68] J.G. Simmons. Generalized formula for the electric tunnel effect between similar electrodes separated by a thin insulating film. *Journal of Applied Physics*, 34:1793, 1963.

[69] W.F. Brinkman, R.C. Dynes, and J.M. Rowell. Tunneling conductance of asymmetrical barriers. *Journal of applied physics*, 41(5):1915–1921, 1970.

[70] J.J. Åkerman, R. Escudero, C. Leighton, S. Kim, D.A. Rabson, R.W. Dave, J.M. Slaughter, and I.K. Schuller. Criteria for ferromagnetic–insulator–ferromagnetic tunneling. *Journal of magnetism and magnetic materials*, 240(1):86–91, 2002.

[71] F. Xu, H. Pan, W. Zhang, G. Wang, Z. Li, and P. Xu. Electronic structure of the interface of GaAs(100) with MgO overlayer grown by thermal evaporation of Mg in O_2 under UHV. *Journal of Electron Spectroscopy and Related Phenomena*, 144–147(0):385–388, 2005.

[72] M.A. Herman, W. Richter, and H. Sitter. *Epitaxy: physical principles and technical implementation*, volume 62. Springer, 2004.

[73] M.A. Herman and H. Sitter. *Molecular beam epitaxy: fundamentals and current status.* Springer Berlin, 1996.

[74] A.J. SpringThorpe, S.J. Ingrey, B. Emmerstorfer, P. Mandeville, and W.T. Moore. Measurement of GaAs surface oxide desorption temperatures. *Applied physics letters*, 50(2):77–79, 1987.

[75] Ch. Heyn. Critical coverage for strain-induced formation of InAs quantum dots. *Physical Review B*, 64(16):165306, 2001.

[76] A. Volland. Herstellung und charakterisierung epitaktischer Ni_2MnIn heusler/halbleiter-hybridsysteme. 2010.

[77] R. Waser. *Nanoelectronics and information technology*. Wiley-Vch, 2012.

[78] P.K.J. Wong, Y. Fu, W. Zhang, Y. Zhai, Y.B. Xu, Z.C. Huang, Y.X. Xu, and H.R. Zhai. Influence of capping layers on magnetic anisotropy in Fe/MgO/GaAs (100) ultrathin films. *Magnetics, IEEE Transactions on*, 44(11):2907–2910, 2008.

[79] S.S.P. Parkin, Ch. Kaiser, A. Panchula, P.M. Rice, B. Hughes, M. Samant, and S.-H. Yang. Giant tunnelling magnetoresistance at room temperature with MgO (100) tunnel barriers. *Nature materials*, 3(12):862–867, 2004.

[80] I. Hernandez-Calderon and H. Höchst. New method for the analysis of reflection high-energy electron diffraction: α-Sn (001) and InSb (001) surfaces. *Physical Review B*, 27(8):4961, 1983.

[81] J. Klein. Epitaktische heterostrukturen aus dotierten manganaten. 2001.

[82] K. Kopitzki and P. Herzog. *Einführung in die Festkörperphysik*. Springer, 2007.

[83] W. Braun. *Applied RHEED: reflection high-energy electron diffraction during crystal growth*. Number 154. Springer, 1999.

[84] R.F.C. Farrow. *Molecular beam epitaxy: applications to key materials*. Access Online via Elsevier, 1995.

[85] R.D.G. Prasad, G. Mohan Rao, and S. Mohan. Electrical resistivity and thermoelectric power of iron films. *Journal of Materials Science Letters*, 9(6):650–651, 1990.

[86] T. Zychowicz, J. Krupka, and J. Mazierska. Measurements of conductivity of thin gold films at microwave frequencies employing resonant techniques. pages 572–574, 2006.

[87] M.F.C. Ladd and R.A. Palmer. *Structure determination by X-ray crystallography*. Springer, 2003.

[88] P. Kidd. *XRD of gallium nitride and related compounds: strain, composition and layer thickness*. PANalytical.

[89] L. Vegard. Die konstitution der mischkristalle und die raumfüllung der atome. *Zeitschrift für Physik A Hadrons and Nuclei*, 5(1):17–26, 1921.

[90] A.R. Denton and N.W. Ashcroft. Vegard's law. *Physical Review A*, 43(6):3161, 1991.

[91] W.E. Hoke, T.D. Kennedy, and A. Torabi. Simultaneous determination of poisson ratio, bulk lattice constant, and composition of ternary compounds: $In_{0.3}Ga_{0.7}As$, $In_{0.3}Al_{0.7}As$, $In_{0.7}Ga_{0.3}P$ and $In_{0.7}Al_{0.3}As$. *Applied Physics Letters*, 79(25):4160–4162, 2001.

[92] B. Aschenbach. X-ray telescopes. *Reports on Progress in Physics*, 48(5):579, 1985.

[93] M. Birkholz. *Thin film analysis by X-ray scattering*. Wiley. com, 2006.

[94] J. Daillant and A. Gibaud. *X-ray and neutron reflectivity: principles and applications*, volume 770. Springer, 2009.

[95] E. Chason and T.M. Mayer. Thin film and surface characterization by specular x-ray reflectivity. *Critical Reviews in Solid State and Material Sciences*, 22(1):1–67, 1997.

[96] H. Kiessig. Interferenz von röntgenstrahlen an dünnen schichten. *Annalen der Physik*, 402(7):769–788, 1931.

[97] T.C. Huang, R. Gilles, and G. Will. Thin-film thickness and density determination from x-ray reflectivity data using a conventional power diffractometer. *Thin Solid Films*, 230:99–101, 1993.

[98] K. Sakurai and A. Lida. Fourier analysis of interference structure in x-ray specular reflection from thin films. *Japanese Journal of Applied Physics*, 31:L113, 1992.

[99] G. Maurer, H. Neff, B. Scholtes, and E. Macherauch. Texture and lattice deformation pole figures of machined surfaces. *Texture, Stress, and Microstructure*, 8:639–678, 1988.

[100] M.T. Johnson, P.J.H. Bloemen, F.J.A. Den Broeder, and J.J. De Vries. Magnetic anisotropy in metallic multilayers. *Reports on Progress in Physics*, 59(11):1409, 1996.

[101] Z.Q. Qiu and S.D. Bader. Surface magneto-optic kerr effect. *Review of Scientific Instruments*, 71(3):1243–1255, 2000.

[102] L.D. Landau, E.M. Lifšic, J.B. Sykes, J.S. Bell, M.J. Kearsley, and L.P. Pitaevskii. *Electrodynamics of continuous media*, volume 364. Pergamon press Oxford, 1960.

[103] T. Nickel. Structural, electrical and magnetic properties of iron layers grown on (001)GaAs. Master's thesis.

[104] T. Kuschel, H. Bardenhagen, H. Wilkens, R. Schubert, J. Hamrle, J. Pištora, and J. Wollschläger. Vectorial magnetometry using magnetooptic Kerr effect including

first-and second-order contributions for thin ferromagnetic films. *Journal of Physics D: Applied Physics*, 44(26):265003, 2011.

[105] N. Tournerie, P. Schieffer, B. Lépine, C. Lallaizon, P. Turban, and G. Jézéquel. In-plane magnetic anisotropies in epitaxial Fe (001) thin films. *Physical Review B*, 78(13):134401, 2008.

[106] E.C. Stoner and E.P. Wohlfarth. A mechanism of magnetic hysteresis in heterogeneous alloys. *Philosophical Transactions of the Royal Society of London. Series A. Mathematical and Physical Sciences*, pages 599–642, 1948.

[107] R.P. Cowburn, S.J. Gray, J. Ferré, J.A.C. Bland, and J. Miltat. Magnetic switching and in-plane uniaxial anisotropy in ultrathin Ag/Fe/Ag (100) epitaxial films. *Journal of applied physics*, 78(12):7210–7219, 1995.

[108] J.M. Florczak and E.D. Dahlberg. Magnetization reversal in (100) Fe thin films. *Physical Review B*, 44(17):9338, 1991.

[109] T. Kuschel, J. Hamrle, J. Pištora, K. Saito, S. Bosu, Y. Sakuraba, K. Takanashi, and J. Wollschläger. Magnetic characterization of thin $Co_{50}Fe_{50}$ films by magnetooptic kerr effect. *Journal of Physics D: Applied Physics*, 45(49):495002, 2012.

[110] R. Moosbuhler, F. Bensch, M. Dumm, and G. Bayreuther. Epitaxial Fe films on GaAs (001): Does the substrate surface reconstruction affect the uniaxial magnetic anisotropy? *Journal of applied physics*, 91(10):8757–8759, 2002.

[111] E. Sjöstedt, L. Nordström, F. Gustavsson, and O. Eriksson. Uniaxial magnetocrystalline anisotropy of metal/semiconductor interfaces: Fe/ZnSe (001). *Physical review letters*, 89(26):267203, 2002.

[112] G. Bayreuther, M. Dumm, B. Uhl, R. Meier, and W. Kipferl. Magnetocrystalline volume and interface anisotropies in epitaxial films: universal relation and neel's model. *Journal of applied physics*, 93(10):8230–8235, 2003.

[113] M. Dumm, M. Zolfl, R. Moosbuhler, M. Brockmann, T. Schmidt, and G. Bayreuther. Magnetism of ultrathin FeCo (001) films on GaAs (001). *Journal of Applied Physics*, 87(9):5457–5459, 2000.

[114] S. McPhail, C.M. Gürtler, F. Montaigne, Y.B. Xu, M. Tselepi, and J.A.C. Bland. Interface bonding versus strain-induced magnetic anisotropy in epitaxial Fe/semiconductor structures. *Physical Review B*, 67(2):024409, 2003.

[115] M. Brockmann, M. Zölfl, S. Miethaner, and G. Bayreuther. In-plane volume and interface magnetic anisotropies in epitaxial Fe films on GaAs (001). *Journal of magnetism and magnetic materials*, 198:384–386, 1999.

[116] E. Schuster. *Struktur, Magnetismus und Grenzflächeneigenschaften epitaktischer dünner Fe-und FePt-Filme auf GaAs (001)-Substraten.* PhD thesis, Universität Duisburg-Essen, Fakultät für Physik, Angewandte Physik, 2008.

[117] S. Députier, R. Guérin, B. Lépine, A. Guivarc'h, and G. Jézéquel. The ternary compound $Fe_3Ga_{2-x}As_x$: a promising candidate for epitaxial and thermodynamically stable contacts on GaAs. *Journal of alloys and compounds*, 262:416–422, 1997.

[118] A. Ohtake. Surface reconstructions on GaAs (001). *Surface Science Reports*, 63(7):295–327, 2008.

[119] J.J. Krebs, B.T. Jonker, and G.A. Prinz. Properties of Fe single-crystal films grown on (100) GaAs by molecular-beam epitaxy. *Journal of applied physics*, 61(7):2596–2599, 1987.

[120] M. Gester, C. Daboo, R.J. Hicken, S.J. Gray, A. Ercole, and J.A. Bland. Continuous evolution of the in-plane magnetic anisotropies with thickness in epitaxial Fe films. *Journal of applied physics*, 80(1):347–355, 1996.

[121] L. Jianqiang, M. Fanbin, L. Guodong, C. Xueguang, H. Luo, L. Enke, and W. Guangheng. Electronic structure and magnetism of binary Fe-based half-heusler alloys Fe_2Z (Z= In, Sn, Sb and As). *Journal of Magnetism and Magnetic Materials*, 33:82–87, 2012.

[122] H.M. Ledbetter and R.P. Reed. Elastic properties of metals and alloys, I. iron, nickel, and iron-nickel alloys. *Journal of Physical and Chemical Reference Data*, 2:531, 1973.

[123] C. Daboo, R.J. Hicken, E. Gu, M. Gester, S.J. Gray, D.E.P. Eley, E. Ahmad, J.A.C. Bland, R. Ploessl, and J.N. Chapman. Anisotropy and orientational dependence of magnetization reversal processes in epitaxial ferromagnetic thin films. *Physical Review B*, 51(22):15964, 1995.

[124] Y.B. Xu, E.T.M. Kernohan, D.J. Freeland, A. Ercole, M. Tselepi, and J.A.C. Bland. Evolution of the ferromagnetic phase of ultrathin fe films grown on GaAs (100)-4× 6. *Physical Review B*, 58(2):890, 1998.

[125] I. Vincze and A.T. Aldred. Mössbauer measurements in iron-base alloys with non-transition elements. *Physical Review B*, 9(9):3845, 1974.

[126] J. Camarero, J.J. De Miguel, R. Miranda, and A. Hernando. Thickness-dependent coercivity of ultrathin Co films grown on Cu (111). *Journal of Physics: Condensed Matter*, 12(35):7713, 2000.

[127] M. Niño, J. Camarero, L. Gómez, J. Ferrón, J.J. de Miguel, and R. Miranda. Surfactant-assisted epitaxial growth and magnetism of Fe films on Cu (111). *Journal of Physics: Condensed Matter*, 20(26):265008, 2008.

[128] C.H. Li, G. Kioseoglou, O.M.J. van't Erve, A.T. Hanbicki, B.T. Jonker, R. Mallory, M. Yasar, and A. Petrou. Spin injection across (110) interfaces: Fe/GaAs (110) spin-light-emitting diodes. *Applied physics letters*, 85:1544, 2004.

[129] C. Adelmann, X. Lou, J. Strand, C.J. Palmstrøm, and P.A. Crowell. Spin injection and relaxation in ferromagnet-semiconductor heterostructures. *Physical Review B*, 71(12):121301, 2005.

[130] L.R. Fleet, K. Yoshida, H. Kobayashi, Y. Ohno, H. Kurebayashi, J.-Y. Kim, C.H.W. Barnes, and A. Hirohata. Schottky barrier height in Fe/GaAs films. *Magnetics, IEEE Transactions on*, 46(6):1737–1740, 2010.

[131] Y.J. Park, M.C. Hickey, M.J. Van Veenhuizen, J. Chang, D. Heiman, and J.S. Moodera. Analysis of current-voltage characteristics of Fe/MgO/GaAs junctions using self-consistent field modeling. *Physical Review B*, 80(24):245315, 2009.

[132] O. Madelung, U. Rössler, and M. Shultz. II–VI and I–VII compounds; semimagnetic compounds, 1999.

[133] G. Chen, J.X. Li, J. Zhu, J.H. Liang, and Y.Z. Wu. In-plane magnetic anisotropy in Fe/MgO/GaAs (001) system. *Journal of Applied Physics*, 109:07C108, 2011.

[134] E.J. Tarsa, M. De Graef, D.R. Clarke, A.C. Gossard, and J.S. Speck. Growth and characterization of (111) and (001) oriented MgO films on (001) GaAs. *Journal of applied physics*, 73(7):3276–3283, 1993.

[135] K.-H. Kim, H.-J. Kim, G.-H. Kim, J. Chang, and S.-H. Han. Strain-induced microstructural evolution in epitaxial Fe/MgO layers grown on $In_x Ga_{1-x} As$(001) substrates. *Applied Physics Letters*, 95(16):164103–164103, 2009.

[136] K.-H. Kim, H.-J. Kim, J.-P. Ahn, S.-C. Lee, S. Ok Won, J. Woo Choi, and J. Chang. Epitaxial growth of Fe and MgO layers on GaAs (001): Microstructure and magnetic property. *Journal of Applied Physics*, 110(11):114910–114910, 2011.

[137] G. Wedler, C.M. Schneider, A. Trampert, and R. Koch. Strain relief of heteroepitaxial bcc-Fe (001) films. *Physical review letters*, 93(23):236101, 2004.

[138] R. Koch, M. Weber, K. Thürmer, and K.H. Rieder. Magnetoelastic coupling of Fe at high stress investigated by means of epitaxial Fe (001) films. *Journal of magnetism and magnetic materials*, 159(1):L11–L16, 1996.

[139] S. Sakshath, S.V. Bhat, P.S. Anil Kumar, D. Sander, and J. Kirschner. Enhancement of uniaxial magnetic anisotropy in Fe thin films grown on GaAs (001) with an MgO underlayer. *Journal of Applied Physics*, 109(7):07C114–07C114, 2011.

[140] H. Saito, Y. Mineno, S. Yuasa, and K. Ando. Reducing schottky barrier height for Fe/n-GaAs junction by inserting thin GaO_x layer. *Journal of Applied Physics*, 109(7):07C701–07C701, 2011.

[141] Y. Lu, J.C. Le Breton, P. Turban, B. Lépine, P. Schieffer, and G. Jézéquel. Band structure of the epitaxial Fe/MgO/GaAs (001) tunnel junction studied by X-ray and ultraviolet photoelectron spectroscopies. *Applied physics letters*, 89:152106, 2006.

[142] Y.J. Park, M.C. Hickey, M.J. Van Veenhuizen, J. Chang, D. Heiman, C.H. Perry, and J.S. Moodera. Efficient spin transfer phenomena in Fe/MgO/GaAs structure. *Journal of Physics: Condensed Matter*, 23(11):116002, 2011.

[143] B. Landgraf, T. Slobodskyy, Ch. Heyn, and W. Hansen. Strain relaxation in metamorphic InAlAs buffers. *Materials Science and Engineering: B*, 2012.

[144] A. Trampert, K.H. Ploog, and E. Tournié. Anisotropic misfit dislocation nucleation in two-dimensional grown InAs/GaAs (001) heterostructures. *Applied physics letters*, 73(8):1074–1076, 1998.

[145] A.E. Romanov, W. Pompe, S. Mathis, G.E. Beltz, and J.S. Speck. Threading dislocation reduction in strained layers. *Journal of applied physics*, 85(1):182–192, 1999.

[146] J.M. Moison, C. Guille, F. Houzay, F. Barthe, and M. Van Rompay. Surface segregation of third-column atoms in group III-V arsenide compounds: Ternary alloys and heterostructures. *Physical Review B*, 40(9):6149, 1989.

[147] H.R. Wenk and P. Van Houtte. Texture and anisotropy. *Reports on Progress in Physics*, 67(8):1367, 2004.

[148] F. Capotondi, G. Biasiol, D. Ercolani, and L. Sorba. Scattering mechanisms in undoped $In_{0.75}Ga_{0.25}As/In_{0.75}Al_{0.25}As$ two-dimensional electron gases. *Journal of crystal growth*, 278(1-4):538–543, 2005.

[149] L. Liefeith. In-Gehalt Abhängigkeit der Beweglichkeit in metamorphen InAs-HEMTs. 2011.

[150] T.O. Wiegard. *Anleitung zum Versuch: Quantum-Hall-Effekt*, volume 2. 1995.

[151] P.V. Panat and V.V. Paranjape. Screening effects in two-dimensional electron gas. *Solid state communications*, 62(12):829–832, 1987.

[152] D. Ercolani, G. Biasiol, E. Cancellieri, M. Rosini, C. Jacoboni, F. Carillo, S. Heun, L. Sorba, and F. Nolting. Transport anisotropy in $In_{0.75}Ga_{0.25}As$ two-dimensional electron gases induced by indium concentration modulation. *Physical Review B*, 77(23):235307, 2008.

[153] D. Jena, A.C. Gossard, and U.K. Mishra. Dislocation scattering in a two-dimensional electron gas. *Applied Physics Letters*, 76(13):1707–1709, 2000.

[154] Y. Lin, J.A. Carlin, A.R. Arehart, A.M. Carlin, and S.A. Ringel. High-mobility two-dimensional electron gas in InAlAs/InAs heterostructures grown on virtual InAs substrates by molecular-beam epitaxy. *Applied physics letters*, 90:012115, 2007.

[155] R.S. Goldman, K.L. Kavanagh, H.H. Wieder, V.M. Robbins, S.N. Ehrlich, and R.M. Feenstra. Correlation of buffer strain relaxation modes with transport properties of two-dimensional electron gases. *Journal of applied physics*, 80(12):6849–6854, 1996.

[156] A. Gold. Scattering time and single-particle relaxation time in a disordered two-dimensional electron gas. *Physical Review B*, 38(15):10798, 1988.

[157] W. Walukiewicz, H.E. Ruda, J. Lagowski, and H.C. Gatos. Electron mobility in modulation-doped heterostructures. *Physical Review B*, 30(8):4571, 1984.

[158] S. Löhr. *Modulierte zweidimensionale Elektronengase und Spin-Bahn Wechselwirkung in InAs und GaAs Heterostrukturen*. Cuvillier Verlag, 2004.

[159] N. Tournerie, P. Schieffer, B. Lepine, C. Lallaizon, and G. Jezequel. Structural and magnetic anisotropy properties in epitaxial Fe films on $Al_{0.48}In_{0.52}As$ (001). *Magnetics, IEEE Transactions on*, 41(10):3322–3324, 2005.

[160] C. Marinelli, L. Sorba, M. Lazzarino, D. Kumar, E. Pelucchi, B.H. Muller, D. Orani, S. Rubini, A. Franciosi, S. De Franceschi, and F. Beltram. Tunable schottky barrier contacts to $In_xGa_{1-x}As$. *Journal of Vacuum Science Technology B: Microelectronics and Nanometer Structures*, 18(4):2119–2127, 2000.

[161] T. Akazaki, J. Nitta, H. Takayanagi, T. Enoki, and K. Arai. Improving the mobility of an $In_{0.52}Al_{0.48}As/In_{0.53}Ga_{0.47}As$ inverted modulation-doped structure by inserting a strained InAs quantum well. *Applied physics letters*, 65(10):1263–1265, 1994.

[162] I. Vurgaftman, J.R. Meyer, and L.R. Ram-Mohan. Band parameters for III–V compound semiconductors and their alloys. *Journal of applied physics*, 89(11):5815–5875, 2001.

[163] K. Tivakornsasithorn, A.M. Alsmadi, X. Liu, J.C. Leiner, Y. Choi, D.J. Keavney, K.F. Eid, M. Dobrowolska, and J.K. Furdyna. Exchange bias and asymmetric magnetization reversal in ultrathin Fe films grown on GaAs (001) substrates. *Journal of Applied Physics*, 113(13):133908–133908, 2013.

[164] T. Akiho, T. Uemura, M. Harada, K. Matsuda, and M. Yamamoto. Effect of MgO barrier insertion on spin-dependent transport properties of CoFe/n-GaAs heterojunctions. *Japanese Journal of Applied Physics*, 51(2), 2012.

[165] C.H. Möller. *Novel magnetoresistance effects in microstructured metal-semiconductor hybrid structures fabricated by cleaved-edge overgrowth.* Cuvillier Verlag, 2003.

[166] J. Herfort, H.-P. Schonherr, and K.-H. Ploog. Epitaxial growth of $Fe_3Si/GaAs(001)$ hybrid structures. *Applied physics letters*, 83(19):3912–3914, 2003.

[167] M. Hashimoto, J. Herfort, A. Trampert, and K.H. Ploog. Growth, interface structure and magnetic properties of heusler alloy $Co_2FeSi/GaAs$ (001) hybrid structures. *Journal of Crystal Growth*, 301:592–596, 2007.

[168] A. Ionescu, C.A.F. Vaz, T. Trypiniotis, C.M. Gürtler, H. García-Miquel, J.A.C. Bland, M.E. Vickers, R.M. Dalgliesh, S. Langridge, Y. Bugoslavsky, et al. Structural, magnetic, electronic, and spin transport properties of epitaxial $Fe_3Si/$ GaAs (001). *Physical Review B*, 71(9):094401, 2005.

[169] J. Herfort, H.-P. Schonherr, and B. Jenichen. Magnetic and structural properties of ultrathin epitaxial Fe_3Si films on GaAs (001). *Journal of Applied Physics*, 103(7):07B506–07B506, 2008.

[170] S. Wurmehl, G.-H. Fecher, H.-C. Kandpal, V. Ksenofontov, C. Felser, and H.-J. Lin. Investigation of CoFeSi: The heusler compound with highest curie temperature and magnetic moment. *Applied physics letters*, 88:032503, 2006.

[171] M. Hashimoto, J. Herfort, H.-P. Schönherr, and K.H. Ploog. Epitaxial heusler alloy $Co_2FeSi/GaAs$ (001) hybrid structures. *Applied Physics Letters*, 87:102506, 2005.

Acknowledgements

Finally, I would like to thank Nicole Yee. She is wonderful beyond words, and I am blessed to have her with me at my side in life. She has always supported and encouraged me, and she has believed in me at times when I felt uncertain. Her love and kindness have always been a great inspiration to me!